Summer 2016

Nanostructured materials prepared by atomic layer deposition for catalysis and lithium-ion battery applications

Rajankumar Patel

Department: Chemical and Biochemical Engineering

Recommended Citation

Patel, Rajankumar, "Nanostructured materials prepared by atomic layer deposition for catalysis and lithium-ion battery applications" (2016). *Doctoral Dissertations*. 2652.
https://scholarsmine.mst.edu/doctoral_dissertations/2652

NANOSTRUCTURED MATERIALS PREPARED BY ATOMIC LAYER DEPOSITION FOR CATALYSIS AND LITHIUM-ION BATTERY APPLICATIONS

by

RAJANKUMAR PATEL

A DISSERTATION

Presented to the Faculty of the Graduate School of the

MISSOURI UNIVERSITY OF SCIENCE AND TECHNOLOGY

In Partial Fulfillment of the Requirements for the Degree

DOCTOR OF PHILOSOPHY

in

CHEMICAL ENGINEERING

2016

Approved by:

Xinhua Liang, Advisor
Muthanna Al-Dahhan
Joontaek Park
Fateme Rezaei
Amitava Choudhury

PUBLICATION DISSERTATION OPTION

This thesis consists of the following five articles that have been published or pending submission for publication:

Paper I, Pages 23-42, “Highly porous titania films coated on sub-micron particles with tunable thickness by molecular layer deposition in a fluidized bed reactor” has been published in *Ceramics International* 41(2): 2240-2246, 2015.

Paper II, Pages 43-52, “Encapsulation of supported metal nanoparticles with an ultra-thin porous shell for size-selective reactions” has been published in *Chemical Communications* 49(86): 10067-10069, 2013.

Paper III, Pages 53-86, “Significant capacity and cycle-life improvement of lithium-ion batteries through ultrathin conductive film stabilized cathode particles” has been published in *Advanced Materials Interfaces* 2(8): 1500046, 2015.

Paper IV, Pages 87-111, “Ionic and electronic conductivities of thin atomic layer deposited film coated lithium ion battery cathode particles” has been *submitted to RSC Advances*.

Paper V, Pages 112-153, “Employing synergetic effect of doping and thin film coating to boost the performance of lithium-ion battery cathode particles” revision has been submitted to *Scientific Reports*.

ABSTRACT

Atomic/molecular layer deposition (ALD/MLD) has emerged as an important technique for depositing thin films in both scientific research and industrial applications. In this dissertation, ALD/MLD was used to create novel nanostructures for two different applications, catalysis and lithium-ion batteries.

MLD was used to prepare ultra-thin dense hybrid organic/inorganic polymer films. Oxidizing the hybrid films removed the organic components and produced the desired nanoporous films. Both porous alumina and titania films can be prepared by such a way. A novel nanostructured catalyst (Pt/SiO_2) with an ultra-thin porous alumina shell obtained from the thermal decomposition of an aluminium alkoxide film deposited by MLD for size-selective reactions was developed. The molecular sieving capability of the porous metal oxide films was verified by examining the liquid-phase hydrogenation of n-hexene versus cis-cyclooctene.

For lithium-ion battery cathodes, two different approaches are presented. Firstly, ultrathin and highly-conformal conductive CeO_2 films were coated on $LiMn_2O_4$ particles using ALD process. The initial capacity of the 3 nm CeO_2-coated sample showed 24% increment compared to the capacity of the uncoated one, and 96% and 95% of the initial capacity was retained after 1,000 cycles with 1C rate at room temperature (RT) and 55 °C, respectively. The study of ionic and electronic conductivities of the coated and uncoated materials helped explain the improved performance of CeO_2 coated materials. Secondly, iron oxide films were deposited using ALD on $LiMn_{1.5}Ni_{0.5}O_4$ particles for the synergetic effect of performance enhancing by iron doping and conformal iron oxide film coating. With an optimal film thickness of ~0.6 nm, the initial capacity improved by 25% at RT and by ~26% at 55 °C at 1C cycling rate. The synergy of doping of $LiMn_{1.5}Ni_{0.5}O_4$ with Fe near surface combined with the conductive and protective nature of the optimal iron oxide film led to high capacity retention (~93% at RT and ~91% at 55 °C) even after 1,000 cycles at 1C cycling rate.

ACKNOWLEDGMENTS

I am very grateful to my advisor, Dr. Xinhua Liang. Without his support, encouragement and patience, this study would not have been completed. His excellent guidance, numerous valuable suggestions and discussions not only made this dissertation possible, but also taught me a proper, meticulous academic approach towards research, for which I would like to express my deepest gratitude to him.

I also would like to extend my sincere appreciation to Dr. Amitava Choudhury, who always offered his support and guidance. I also sincerely appreciate my other committee members, Dr. Fateme Rezaei, Dr. Muthanna Al-Dahhan, and Dr. Joontaek Park for their constructive suggestions. In addition, I would like to give my thanks to technicians in the Materials Research Center (MRC), Dr. Eric Bohannan for XRD analysis, Mr. Brian Porter for XPS analysis, and Dr. Jessica Terbush and Dr. Clarissa Weisner for TEM analysis.

Many thanks also go to the technician, Mr. Dean Lenz, and staff in Chemical and Biochemical Engineering department. I thank them all for the great assistance they provided during my studies in Rolla. All of my colleagues in Dr. Liang's group and my friends deserve many thanks as well. I greatly appreciate their help, useful discussions and friendship during my Ph.D. studies.

Last but not least, I would like to thank my family members who made this possible: my parents, and my wife for their continual encouragement, support, and love that keeps me moving forward in my studies and my life as well.

TABLE OF CONTENTS

Page

SECTION

PAPER

SECTION

LIST OF FIGURES

PAPER I

PAPER II

PAPER III

PAPER IV

PAPER V

LIST OF TABLES

Table Page

PAPER III

PAPER IV

PAPER V

1. INTRODUCTION

1.1. ATOMIC LAYER DEPOSITION TECHNIQUE

Atomic Layer Deposition (ALD) as an outgrowth of molecular beam epitaxy was, earlier, called atomic layer evaporation or epitaxy. Finnish researchers led by Suntola in the 1970s,[1] and Russian researchers led by Aleskovskii in the 1960s are the earliest known ALD developers.[2, 3] Distinguished from other deposition techniques, such as chemical vapor deposition (CVD), physical vapor deposition (PVD), and other solution-based methods, ALD as a chemical vapor method operates with a unique mechanism relying on two gas-solid half-reactions to produce an ultimate material.[4] The reactions of ALD feature the characteristics of surface-controlled and self-terminating nature. In return, ALD performs the deposition of films in a layer-by-layer mode and it is especially superior in controlling films at the atomic level. As a result, ALD provides the deposited films with excellent uniformity and unrivalled conformality. In essence, ALD works with a temperature lower than the decomposition of the used precursors, typically lower than 400 ºC, even down to room temperature. In addition, ALD requires no catalysts and has no needs on solvents. All the aforementioned characteristics contribute ALD to be a unique but precise deposition technique. Ascribed to the above-mentioned advantages, ALD is particularly suitable for production of high-quality thin films. Its initial applications were limited to the growth of II-VI materials and dielectric thin films for electroluminescent display devices,[4] but it was later widened for the growth of III-V compounds.[5] Besides its successes in the areas of semiconductors, ALD has been gaining more applications since the beginning of the 21st century, owing to an increasing recognition on its versatile capabilities. The new widened applications of ALD are closely related with nanotechnology, which offers new opportunities for many areas with novel components.[6] Recent reviews conducted by Knez et al.,[7] Kim et al.,[8] and George[9] jointly provided a comprehensive view on the latest progress of ALD, especially on the fabrication of nanostructured materials. The new tendencies of ALD in nanotechnology are offering ALD many more opportunities in new areas, such as sensors, solar cells, fuel cells, and lithium-ion batteries.

The film growth in ALD is governed by self-limiting gas-solid surface half reactions, unlike the traditional methods, such as CVD and PVD, which are dependent on the primary reactant sources. To demonstrate the underlying mechanism of ALD process, a typical ALD process for the Al_2O_3 is schematically illustrated in Figure 1.1.

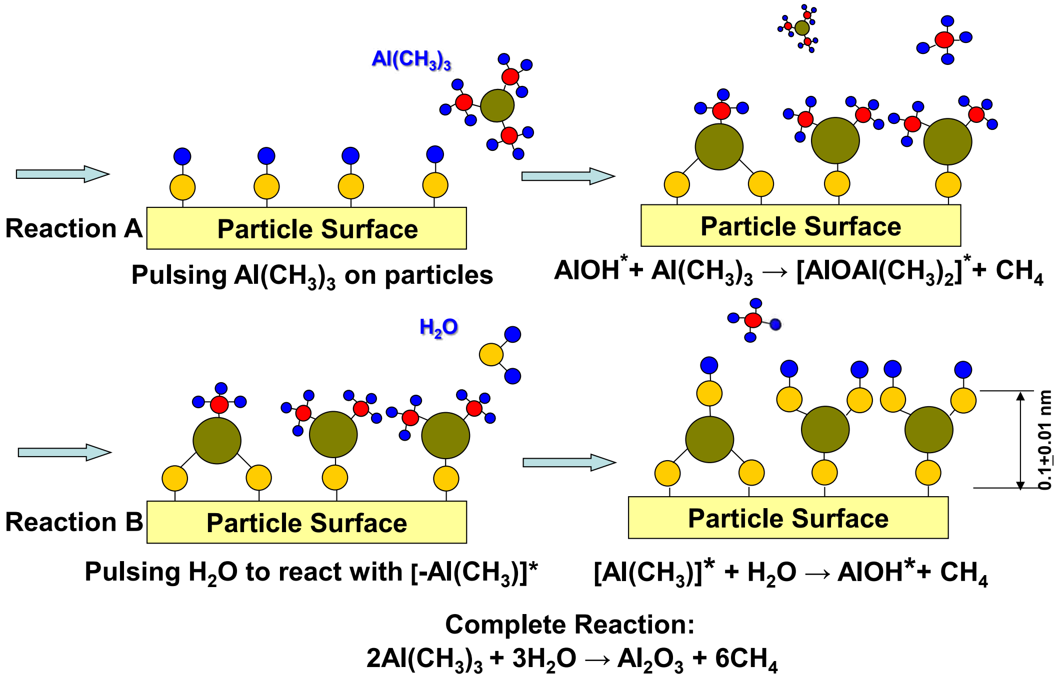

Figure 1.1. Atomic layer deposition reaction steps.

A typical ALD reaction requires two precursors. The most effective ALD process of Al_2O_3 (ALD-Al_2O_3) uses trimethylaluminum (TMA) and water as precursors, as shown in Figure 1 as an example. In a CVD process, the reaction is described by an overall reaction:[10]

$$2Al(CH_3)_3 + 3H_2O \rightarrow Al_2O_3 + 6CH_{4\,(g)} \qquad (1)$$

In comparison, the ALD-Al_2O_3 proceeds with two half-reactions. A typical alumina ALD cycle consists six steps. The metal precursor TMA is first introduced in the reaction chamber which reacts with the native surface functional groups, such as hydroxide groups. The half-reaction of that step is suggested as follows:[10]

$$AlOH^* + Al(CH_3)_{3\,(g)} \rightarrow Al\text{-}O\text{-}Al(CH_3)_2^* + CH_{4\,(g)} \qquad (2)$$

where, the (*) designates the species carried by or chemically attached on substrates, and (g) designates the gaseous byproducts. Once the surface is saturated with AlOH* and forms a layer of $Al\text{-}O\text{-}Al(CH_3)_2^*$, then the reaction chamber is flushed with inert gas to remove any unreacted TMA and any byproducts. The chamber is then purged using vacuum pump to ensure that no TMA is left behind. Only after that, the second precursor, oxidizer, de-ionized water is introduced. The water reacts with the $Al\text{-}O\text{-}Al(CH_3)_2$ layer to form Al_2O_3 monolayer and regenerate -AlOH groups. The half-reaction of this step is suggested as follows:

$$AlCH_3^* + H_2O_{(g)} \rightarrow AlOH^* + CH_{4\,(g)} \qquad (3)$$

The subsequent steps are inert gas flush and vacuum purge. With this one cycle of alumina ALD, ~0.1 nm conformal layer of alumina is achieved. In order to get thicker coating, the cycle is repeated as needed. ALD is cyclic in operation and proceeds in a layer-by-layer fashion.

cycle is repeated as needed. ALD is cyclic in operation and proceeds in a layer-by-layer fashion.

Molecular layer deposition (MLD) is like ALD, and it is also a layer-by-layer, self-terminating process.[11-13] However, during the MLD process, an organic or hybrid organic/inorganic molecular part is attached as a part of the coating process. One Japanese group pioneered the deposition process of organic polymer MLD films using stepwise consolidation.[13, 14] Various reactants has been researched for the organic MLD, such as polyurethane[15], polyurea[16], polyamide,[13, 17] polyimide,[12, 18] and hybrid polyimide–polyamide[19].

At the end of the each coating cycle all the unreacted reactants and byproducts are discarded by purging an inert gas, and an identical surface is produced as the initial native surface with the same functional groups. A control of the amount of material being deposited is achieved by controlling the ALD/MLD coating cycles. Due to the nature of self-terminating reactions, it is possible to achieve ultrathin films with high conformity irrespective of the type of substrate surface, porosity, or surface area.[20] As a result, ALD/MLD has been widely applied in a variety of applications, such as electronics,[7, 20] catalysis,[21-23] photovoltaics,[24] batteries,[25] and fuel cells.[23, 26]

1.2. SIZE-SELECTIVE CATALYSTS

An important and basic concept of catalysis is to selectively transform a particular reactant from a mixture of reactants into products using metallic catalysts, which is also called size or shape-selective catalysis.[27] Many important reactions like combustion reactions, hydrogenation, and dehydrogenation are catalyzed using metallic particles.

However, the conventional metallic catalysts cannot selectively drive the conversion of a certain reactant from a mixture of reactants. Although many attempts have been made to surmount this inadequacy of selective discrimination by fabricating chemically adjusted catalyst surface,[28] optimizing operational conditions,[29] or using manipulative enzyme mimics,[30] significant improvements are not yet to be found. Size-sensitive catalysts with a core-shell structure is an important topic of research, attracting a lot of attention.[31, 32]

The properties of porous shell on the size-selective catalysts are very important. Here, a porous material/media means a material containing pores or voids. Some naturally occurring materials are also porous, for example, rocks, soil, zeolites, biological tissues, and some artificial materials, such as ceramics and cements are also porous. The concept of porous material has been vastly used in many research areas, such as filtration, liquid adsorption and catalysis. They have been applied either as catalyst themselves or as an inert support for the active phase. Some of porous materials have the ability to, at the same time, act as support and also take part in the catalytic process.[33] A useful way to classify a nano-porous material is by the size of their pores, because most of properties interesting for applications of adsorption and diffusion are dependent on this parameter. Based on their pore sizes, the three main categories of porous materials are micropores (pore size < 2 nm), mesopores (pore size 2-50 nm), and macropores (pore size >50 nm). The size distribution, shapes and volume of the porous materials determine their potential to be applied for a particular function. Most common size-selective catalysts are metal nanoparticles encapsulated by mesoporous materials like metal organic frameworks (MOFs),[34] titania[35], silica,[36-38] and zeolites,[39-41] to form a core-shell structure.

The zeolites has been popular for size-selective catalysis over 50 years in the chemical industry.[41-43] However, there is a limitation in the types of molecules that can be part of size or shape-selective reactions over zeolites.[44] One theory is to cover the catalyst in a discriminating film so that the transport of the reactant to the active sites can be controlled.[37] However, it has been proved to be difficult to fabricate a uniform ultrathin films and so many efforts has been focused on creating multi-layered crystallites.[45-47] Weisz et al. were the first to synthesize Pt particles covered in a LTA-type zeolite structure to create size selective metal-containing compounds for the hydrogenation reaction of n-butene in a mixture of n-butene and isobutene.[48, 49] Their process was highly complex with several steps to prepare such sort-of captured metallic catalysts. Another method that has been used to prepare such catalysts consists of a composite material with a polycrystalline zeolite ZSM-5 layer covering Pt nanoparticles supported on titania.[37] The prepared catalysts showed selective discrimination towards the hydrogenation of linear alkenes, rather than the branched alkenes. In a recent report, Pt metal particles were encapsulated in porous zeolite which allowed only small oxide alcohols and acted as a barrier for the large poison molecules.[50]

The preparation of porous films directly deposited onto the surface of catalyst particles is attracting increasing attention.[40, 51, 52] This type of composite materials displayed unusual activity and selectivity patterns in a number of reactions of academic and industrial interest including amine[52] and maleic anhydride[51] syntheses, selective hydrogenation reactions,[40] and Fischer−Tropsch synthesis.[53] In most cases, zeolite-based films deposited on macroscopic beads or supports were prepared by in situ synthesis of the zeolite. However, post-synthesis deposition techniques have also been developed.[36, 54] For example, Foley et al.[52] demonstrated that it was possible to obtain shape selectivity effect by creating a layer of amorphous carbon-based molecular sieve on top of silica−alumina particles.

It was reported that the possibility to prepare a thin monocrystalline zeolite layer encapsulating Pt nanoparticles supported over SiO_2 catalysts for the selective oxidation of CO in the mixture of CO and butane.[51, 55] They used a polyelectrolyte cationic polymer to achieve the shorter connection between the zeolite seeds and the catalyst. The cationic polymer caused the same repulsion effect between the oppositely charged oxide surfaces.[39] A range of hydrocarbons were produced by selective Fischer-Tropsch reactions using Co/SiO_2 encapsulated by H-ZSM-5 films.[53, 56] Using a polycrystalline coating of silicalite-1 on Pt/TiO_2, Nishiyama et al. demonstrated the size discriminating hydrogenation reaction to produce a range of hydrocarbons.[57, 58] In all previous studies, a macroscopic layer was coated on metal/SiO_2 grains, and the activity was given by the metal particles underneath the membrane. However, the thickness of the zeolite shell was usually from 200 nm up to several microns,[55, 57] which eventually limited the overall reaction rates due to diffusion transport limitations.[57]

For porous films used in size-selective catalysts, the films should be defect free and have a very uniform porous structure, in order to have a good effect of molecular discrimination so that high selectivity can be achieved; the films should also be ultra-thin, so that there will be not much mass diffusion and the films can be deposited into some porous substrates, which are typically used as catalyst supports. MLD process has been used for preparing the porous thin films with precise thickness. This process allows a film to be conformally constructed on surfaces with arbitrary shapes and surface areas. It has recently been demonstrated that ultra-thin porous aluminum oxide films can be prepared from organic-inorganic hybrid MLD polymer films by removing the organic components.[59, 60] The level of porosity is dependent on the organic contents of the deposited hybrid MLD films. In this work, ultra-thin porous alumina shell was achieved after decomposition of aluminium alkoxide films deposited using MLD process to fabricate an innovative nanostructured catalyst for size selective reactions.

1.3. LITHIUM-ION BATTERY CATHODE MATERIALS

Rechargeable lithium-ion batteries (LIBs) have drawn extensive attention due to their excellent properties, such as high energy density and light weight. A single-cell lithium battery consists of a positive and negative electrode, called the cathode and anode, respectively. Normally, the anode consists of some form of carbon (e.g., graphite) and the cathode consists of a lithiated transition metal compound (e.g., $LiMn_2O_4$). The anode and cathode are kept apart by electrically insulating separator. In order to enable Li-ion transport between the two electrodes, the separator is soaked in a liquid electrolyte, consisting of a dissolved lithium salt (e.g., $LiPF_6$) in a mixture of organic alkyl carbonate solvents, such as ethylene, dimethyl, diethyl and ethyl methyl carbonate (EC, DMC, DEC, and EMC, respectively). Another important requirement of the liquid electrolyte is that it also must be electrically insulating, to avoid short-circuiting of the cell. Once these electrodes are connected externally, chemical reactions can proceed simultaneously at both electrodes, converting chemical energy to useful electrical energy, see Figure 1.2.

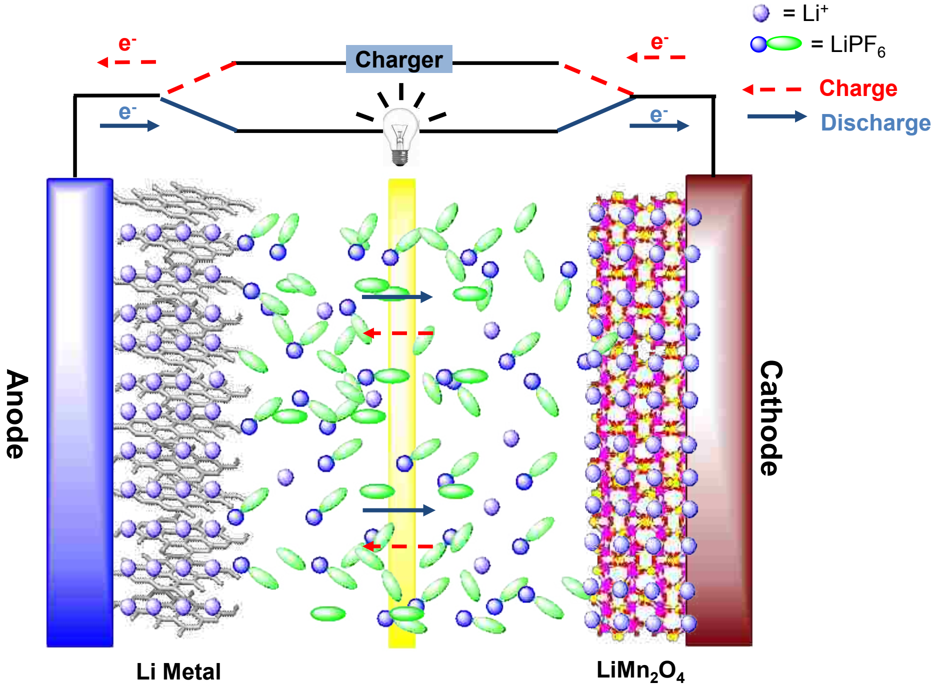

Figure 1.2. A simple overview of a common lithium ion battery, illustrating the processes occurring during discharge and charge.

During discharge, electrons leave the anode (it is oxidized) and travel to the cathode through the external circuit (doing useful work), while the lithium ions are extracted (deintercalated) from the anode and travel to the cathode through the electrolyte. At the cathode, metal atoms in the host structure are reduced as they receive the electrons, and the lithium-ions traveling through the electrolyte are inserted into the cathode (intercalated). During charging the opposite reactions occur.

Typical cathode materials, such as $LiCoO_2$, $LiNiO_2$, $LiMn_2O_4$ and $LiFePO_4$, have been widely investigated for LIBs with high energy and power density, or good cycling stability. Among them, $LiCoO_2$ has been used in commercial rechargeable LIBs thanks to its easy production, high cell voltage (3.6 V) and high specific capacity (140 mAh/g). However, cobalt resource on earth is quite limited and causes a much high production cost of resultant LIBs. Besides, cobalt is a very toxic element, which may pollute natural environment, if $LiCoO_2$-based LIBs are not correctly disposed. $LiNiO_2$ is less toxic material for LIBs, and nickel reserve on earth is much larger than cobalt. Its working potential is 3.6 V (vs. Li/Li^+), with a large specific capacity of 180 mAh/g. However, $LiNiO_2$ with precise stoichiometric ratios is much more difficult to be synthesized, and its crystal structure is not much stable during Li-ion intercalation process, resulting in poor stability of $LiNiO_2$-based LIBs.

Recently, $LiMn_2O_4$ and $LiFePO_4$ become popular cathode materials for high-energy-density LIBs used in electric vehicles. $LiFePO_4$ is cheap, easily-synthesized and environmentally friendly and $LiFePO_4$-based LIBs also have excellent long-term stability. However, its working potential (3.4 V vs. Li/Li+) is low, and its energy density (110 mAh/g) is too small. The biggest drawback of $LiFePO_4$ is very poor electronic conductivity, yielding such low specific energy capacity. For $LiMn_2O_4$, it is a promising material that may be used in future commercial LIBs, due to its unique advantages. It has higher specific capacity (120 mAh/g) and output voltages (3.5 ~ 4.3 V vs. Li/Li^+), higher safety and no memory effect.[61, 62] In addition, $LiMn_2O_4$ has abundant resource and is cheap, non-toxic, and environmentally friendly. However, a critical problem of $LiMn_2O_4$ is its poor stability with electrolyte and its capacity degradation during cycling, which limits its practical applications.[62, 63] In general, the fast capacity fading of $LiMn_2O_4$ can be ascribed to three factors:[64, 65] (1) dissolution of Mn^{2+} ions into solutions. Mn^{2+} ions are formed by a disproportional reaction:

$$2Mn^{3+}{}_{(solid)} \rightarrow Mn^{4+}{}_{(solid)} + Mn^{2+}{}_{(solution)} \tag{4}$$

(2) Jahn-Teller (J-T) distortion effect of Mn^{3+} ions due to the crystallographic transformation of $Li_xMn_2O_4$ (1<x<2) from cubic spinel structure to tetragonal phase that is well-known for its poor capacity retention, and (3) continuous decomposition of electrolytes on the electrode partially due to formation of Mn^{4+} that has high oxidation ability. Thus, a variety of methods have been proposed to solve these problems. For instance, a small amount of cations, such as Al, Ga, Co, Ni , Cr and Ti, are doped into spinel $LiMn_2O_4$ in order to improve its structural stability.[66] A recent Li nuclear magnetic resonance (NMR) study on $Li(M_xMn_{2-x})O_4$ (M = Mn, Cr, Co, Al) has shown that the improved cathodic performance of the doped spinels is due to structural stabilization, whereas Mn dissolution and concomitant Li-for-Mn ion exchange at the end of discharge is the dominant contribution to the capacity fading in $LiMn_2O_4$.[67] The fact that the unsubstituted $LiMn_2O_4$ shows structural change and capacity fade on cycling at ambient temperature[68-70] as well as in the M-substituted spinels at 50 °C,[71] which is in accordance with the proposed structural stability of the material with doping.[68, 72, 73] Another common approach is surface modification of $LiMn_2O_4$ by coating with oxides,[74-76] metals,[77] fluorides,[78] phosphates,[79] polymers,[80] carbon[81] and some electrode materials.[82, 83] The oxide coating on $LiMn_2O_4$ scavenges hydrogen fluoride (HF) formed from side reactions in LIBs, and thus slows down dissolution of manganese ions and degradation of electrolytes at cathode, yielding improved electrochemical performance of $LiMn_2O_4$.

$LiMn_2O_4$ cycles at 4.0 V vs. Li/Li^+. This corresponds to the $Mn^{3+}/^{4+}$ redox couple, which lies in a metal 3d band at a substantial energy above the O:2p band. The characteristic voltage of the cathode can be increased by lowering the energy of the metal 3d band, concomitantly increasing the voltage difference between the cathode redox couple and the anode (and Li/Li$^+$) couple. Increased cell voltage results in a higher energy density at the cost of increased side reactions, which occur between the cathode and the electrolyte. These side reactions deplete the electrolyte and the lithium salt, leading to decreased coulombic efficiency and significant energy density fade over time. The development of new, high-voltage capable electrolytes is a major research area, and progress is being made in ionic liquids and fluorinated organic electrolytes.

One way to increase the cell voltage is to substitute another transition metal for Mn, such as Fe, Co, or Ni. Ni-substituted spinel has been the most successful in terms of performance due to the Ni^{2+}/ Ni^{3+}/ Ni^{4+} redox couples.[84] Up to 0.5 Ni per formula unit can be substituted for Mn, yielding the chemical formula $LiMn_{1.54}Ni_{0.52}O_4$. Further Ni substitution is not possible, and results in a nickel-rich $Li_xNi_{1-x}O$ disordered rocksalt secondary phase during synthesis.[85] By substituting Ni for Mn, the Mn:eg band is depleted in order to donate electrons to the lower energy Ni:eg band, lowering the Fermi energy and increasing the cell voltage. The charge/discharge voltage of $LiMn_{1.5}Ni_{0.5}O_4$ is 4.7 V, approximately 700 mV higher than that of $LiMn_2O_4$. For this reason, $LiMn_{1.5}Ni_{0.5}O_4$ is also called "high-voltage spinel" or "5 V spinel" (even though the actual voltage is just shy of 5V vs. Li/Li$^+$). The 700 mV advantage over $LiMn_2O_4$ gives high-voltage spinel excellent energy density - comparable to layered oxides, but with less Ni and Li precursor materials, so the cost per kWh is lower. This makes it an attractive material for high power battery industry.

1.4. DISSERTATION SUMMARY

In Paper I, fabrication of highly porous titania films with tunable thickness using MLD technique on sub-micron silica particles was introduced. The organic constituents in the films were removed by either calcination in air at elevated temperatures or decomposition in the presence of water at room temperature, which could be very important for coating temperature-sensitive substrates. The resulting porous structures had both micropores and mesopores. This type of porous coating can be used for fine tuning some porous materials, such as zeolite for gas separation, and catalysts with enhanced performance (e.g., increased thermal stability and reaction selectivity).

In Paper II, the same technique as in Chapter 2 was employed to use the ultrathin porous film to cover the metal nanoparticles supported on mesoporous substrate for size-selective reactions. Ultra-thin porous alumina shell was achieved after decomposition of aluminum alkoxide films deposited using MLD process to fabricate an innovative nanostructured catalyst for size selective reactions. The molecular sieving capability of the porous metal oxide films was verified by examining the liquid-phase hydrogenation of *n*-hexene *versus cis*-cyclooctene.

In Paper III, a breakthrough was achieved to overcome a bargain between the cycle life and the capacity using conductive CeO_2 ALD films conformally coated on the $LiMn_2O_4$ particles. The electrochemical tests showed significant improvement in both life cycle and the capacity of the coated samples. The impedance results showed much lower resistance in the case of $LiMn_2O_4$ particles coated with CeO_2 films of an optimal thickness.

In Paper IV, study of ionic and electronic conductivities for the ceria ALD-coated and uncoated LMO and LMNO samples was carried out. Also, the results were compared to the insulating materials such as Al_2O_3 and ZrO_2 ALD-coated LMO samples. The ionic conductivities of the coated samples were at least one magnitude higher than those of the uncoated samples. The experimental results proved that the ionic conductivity of the ceria films was responsible for the improved performance and longer life cycle of the CeO_2 coated $LiMn_2O_4$ samples.

In Paper V, a novel synergetic effect of doping and thin film coating was employed to improve performance and cycle life of cathode particles. The Fe doping occurred mostly during the initial ALD cycles and further ALD cycles coated a conformal iron oxide layer on the $LiMn_{1.5}Ni_{0.5}O_4$ particles. The electrochemical performance showed significant improvement in the capacity, compared to the uncoated samples.

In Section 2, the findings of the dissertation is summarized and some suggestions has been made for the future research work.

REFERENCES

1. Suntola, T.; Antson, J., Method for Producing Compound Thin Films. In Google Patents: **1977**.

2. Aleskovskii, V.; Kol'tsov, S. In *Some Characteristics of Molecular Layering Reactions*, Abstract of Scientific and Technical Conference, Goskhimizdat, Leningrad, 1965; **1965**.

3. A. M. Shevjakov, G. N. K., and V. B. Aleskovskii In *Chemistry of High-Temperature Materials*, Proceedings of the Second USSR Conference on High-temperature Chemistry of Oxides, Nauka, Leningrad, USSR, 11/26/1965, 1965; Nauka, Leningrad, USSR, **1965**; pp 149-155.

4. Suntola, T., Atomic Layer Epitaxy. *Thin Solid Films* **1992,** 216, (1), 84-89.

5. Usui, A., Atomic Layer Epitaxy of III-V Compounds: Chemistry and Applications. *Proceedings of the IEEE* **1992,** 80, (10), 1641-1653.

6. Ritala, M.; Leskelä, M., Atomic Layer Epitaxy - A Valuable Tool for Nanotechnology? *Nanotechnology* **1999,** 10, (1), 19.

7. Knez, M., Nielsch, K., Niinistö, L., Synthesis and Surface Engineering of Complex Nanostructures by Atomic Layer Deposition. *Advanced Materials* **2007,** 19, (21), 1521-4096.

8. Kim, H.; Maeng, W.-J., Applications of Atomic Layer Deposition to Nanofabrication and Emerging Nanodevices. *Thin Solid Films* **2009,** 517, (8), 2563-2580.

9. George, S. M., Atomic Layer Deposition: An Overview. *Chemical Reviews* **2009,** 110, (1), 111-131.

10. Hakim, L. F.; McCormick, J. A.; Zhan, G.-D.; Weimer, A. W.; Li, P.; George, S. M., Surface Modification of Titania Nanoparticles Using Ultrathin Ceramic Films. *Journal of the American Ceramic Society* **2006,** 89, (10), 3070-3075.

11. Nishizawa, J. i.; Abe, H.; Kurabayashi, T., Molecular Layer Epitaxy. *Journal of The Electrochemical Society* **1985,** 132, (5), 1197-1200.

12. Du, Y.; George, S. M., Molecular Layer Deposition of Nylon 66 Films Examined Using in Situ FTIR Spectroscopy. *The Journal of Physical Chemistry C* **2007,** 111, (24), 8509-8517.

13. Yoshimura, T.; Tatsuura, S.; Sotoyama, W., Polymer Films Formed with Monolayer Growth Steps by Molecular Layer Deposition. *Applied Physics Letters* **1991,** 59, (4), 482-484.

14. Yoshimura, T.; Tatsuura, S.; Sotoyama, W.; Matsuura, A.; Hayano, T., Quantum Wire and Dot Formation by Chemical Vapor Deposition and Molecular Layer Deposition of One-Dimensional Conjugated Polymer. *Applied Physics Letters* **1992,** 60, (3), 268-270.

15. Lee, J. S.; Lee, Y.-J.; Tae, E. L.; Park, Y. S.; Yoon, K. B., Synthesis of Zeolite As Ordered Multicrystal Arrays. *Science* **2003,** 301, (5634), 818-821.

16. Kim, A.; Filler, M. A.; Kim, S.; Bent, S. F., Layer-by-Layer Growth on Ge(100) via Spontaneous Urea Coupling Reactions. *J Am Chem Soc* **2005,** 127, (16), 6123-32.

17. Nagai, A.; Shao, H.; Umemoto, S.; Kikutani, T.; Okui, N., Quadruple Aliphatic Polyamide Systems Prepared by a Layer-by-Layer Alternating Vapour Deposition Method. *High Performance Polymers* **2001,** 13, (2), S169-S179.

18. Bitzer, T.; Richardson, N. V., Demonstration of an Imide Coupling Reaction on a Si(100)-2×1 Surface by Molecular Layer Deposition. *Applied Physics Letters* **1997,** 71, (5), 662-664.

19. Takayuki, M.; Kiyomi, T.; Osamu, M.; Sadaaki, Y.; Hisakazu, N., Preparation of Polyimide-Polyamide Random Copolymer Thin Film by Sequential Vapor Deposition Polymerization. *Japanese Journal of Applied Physics* **2002,** 41, (2R), 746.

20. Pagán-Torres, Y. J.; Gallo, J. M. R.; Wang, D.; Pham, H. N.; Libera, J. A.; Marshall, C. L.; Elam, J. W.; Datye, A. K.; Dumesic, J. A., Synthesis of Highly Ordered Hydrothermally Stable Mesoporous Niobia Catalysts by Atomic Layer Deposition. *ACS Catalysis* **2011,** 1, (10), 1234-1245.

21. Liang, X.; Li, J.; Yu, M.; McMurray, C. N.; Falconer, J. L.; Weimer, A. W., Stabilization of Supported Metal Nanoparticles Using an Ultrathin Porous Shell. *ACS Catalysis* **2011,** 1, (10), 1162-1165.

22. Feng, H.; Libera, J. A.; Stair, P. C.; Miller, J. T.; Elam, J. W., Subnanometer Palladium Particles Synthesized by Atomic Layer Deposition. *Acs Catalysis* **2011,** 1, (6), 665-673.

23. King, J. S.; Wittstock, A.; Biener, J.; Kucheyev, S. O.; Wang, Y. M.; Baumann, T. F.; Giri, S. K.; Hamza, A. V.; Baeumer, M.; Bent, S. F., Ultralow Loading Pt Nanocatalysts Prepared by Atomic Layer Deposition on Carbon Aerogels. *Nano Letters* **2008,** 8, (8), 2405-2409.

24. Chen, Y. W.; Prange, J. D.; Dühnen, S.; Park, Y.; Gunji, M.; Chidsey, C. E. D.; McIntyre, P. C., Atomic Layer-Deposited Tunnel Oxide Stabilizes Silicon Photoanodes for Water Oxidation. *Nat Mater* **2011,** 10, (7), 539-544.

25. Scott, I. D.; Jung, Y. S.; Cavanagh, A. S.; Yan, Y.; Dillon, A. C.; George, S. M.; Lee, S.-H., Ultrathin Coatings on Nano-$LiCoO_2$ for Li-Ion Vehicular Applications. *Nano Letters* **2011,** 11, (2), 414-418.

26. Chao, C.-C.; Hsu, C.-M.; Cui, Y.; Prinz, F. B., Improved Solid Oxide Fuel Cell Performance with Nanostructured Electrolytes. *ACS Nano* **2011,** 5, (7), 5692-5696.

27. Smit, B.; Maesen, T. L. M., Towards a Molecular Understanding of Shape Selectivity. *Nature* **2008,** 451, (7179), 671-678.

28. Grisel, R. J. H.; Weststrate, C. J.; Goossens, A.; Crajé, M. W. J.; van der Kraan, A. M.; Nieuwenhuys, B. E., Oxidation of CO over $Au/MO_x/Al_2O_3$ Multi-component Catalysts in a Hydrogen-rich Environment. *Catalysis Today* **2002,** 72, (1–2), 123-132.

29. Sedmak, G.; Hočevar, S.; Levec, J., Kinetics of Selective CO Oxidation in Excess of H_2 over the Nanostructured $Cu_{0.1}Ce_{0.9}O_{2-y}$ Catalyst. *Journal of Catalysis* **2003,** 213, (2), 135-150.

30. De Vos, D.; Sels, B.; Jacobs, P., Heterogeneous Enzyme Mimics Based on Zeolites and Layered Hydroxides. *CATTECH* **2002,** 6, (1), 14-29.

31. Lewis, L. N., Chemical Catalysis by Colloids and Clusters. *Chemical Reviews* **1993,** 93, (8), 2693-2730.

32. Schmid, G., Large Clusters and Colloids. Metals in the Embryonic State. *Chemical Reviews* **1992,** 92, (8), 1709-1727.

33. M. Beller, A. R., R. A. van Santen, Eds., *Catalysis - From Principals to Applications*. Wiley-VCH Verlag GmbH & Co. KGaA: **2012**.

34. Lu, G.; Li, S.; Guo, Z.; Farha, O. K.; Hauser, B. G.; Qi, X.; Wang, Y.; Wang, X.; Han, S.; Liu, X., Imparting Functionality to a Metal–Organic Framework Material by Controlled Nanoparticle Encapsulation. *Nature chemistry* **2012,** 4, (4), 310-316.

35. Zhang, Z.; Zhou, Y.; Zhang, Y.; Sheng, X.; Zhou, S.; Xiang, S., Anisotropic Growth of SiO_2 and TiO_2 Mixed Oxides onto Au Nanostructures: Highly Thermal Stability and Enhanced Reaction Activity. *RSC Advances* **2014,** 4, (75), 40078-40084.

36. Berenguer-Murcia, Á.; Morallón, E.; Cazorla-Amorós, D.; Linares-Solano, Á., Preparation of Silicalite-1 Layers on Pt-coated Carbon Materials: A Possible Electrochemical Aapproach Towards Membrane Reactors. *Microporous and Mesoporous Materials* **2005,** 78, (2–3), 159-167.

37. van der puil, N.; Creyghton, E. J.; Rodenburg, E. C.; Sie, T. S.; van Bekkum, H.; Jansen, J. C., Catalytic Testing of TiO_2/Platinum/Silicalite-1 Composites. *Journal of the Chemical Society, Faraday Transactions* **1996,** 92, (22), 4609-4615.

38. Park, J. N.; Forman, A. J.; Tang, W.; Cheng, J.; Hu, Y. S.; Lin, H.; McFarland, E. W., Highly Active and Sinter-Resistant Pd-Nanoparticle Catalysts Encapsulated in Silica. *Small* **2008,** 4, (10), 1694-1697.

39. Goodman, K. E.; Hayes, J. W.; Malde, C. N.; Petch, M. I., Method of Coating Materials with a Zeolite-type Substance. *European Patent EP 0* **1998,** 878, 233.

40. Zhong, Y.; Chen, L.; Luo, M.; Xie, Y.; Zhu, W., Fabrication of Zeolite-4A Membranes on a Catalyst Particle Level. *Chemical Communications* **2006**, (27), 2911-2912.

41. Degnan Jr, T. F., The Implications of the Fundamentals of Shape Selectivity for the Development of Catalysts for the Petroleum and Petrochemical Industries. *Journal of Catalysis* **2003,** 216, (1–2), 32-46.

42. Ji, Y.-J.; Zhang, B.; Xu, L.; Wu, H.; Peng, H.; Chen, L.; Liu, Y.; Wu, P., Core/Shell-Structured Al-MWW@B-MWW Zeolites for Shape-Selective Toluene Disproportionation to Para-Xylene. *Journal of Catalysis* **2011,** 283, (2), 168-177.

43. Corma, A., Inorganic Solid Acids and Their Use in Acid-Catalyzed Hydrocarbon Reactions. *Chemical Reviews* **1995,** 95, (3), 559-614.

44. Okuhara, T., Microporous Heteropoly Compounds and Their Shape Selective Catalysis. *Applied Catalysis A: General* **2003,** 256, (1–2), 213-224.

45. van der Puil, N.; Dautzenberg, F. M.; van Bekkum, H.; Jansen, J. C., Preparation and Catalytic Testing of Zeolite Coatings on Preshaped Alumina Supports. *Microporous and Mesoporous Materials* **1999,** 27, (1), 95-106.

46. Jansen, J. C.; Koegler, J. H.; van Bekkum, H.; Calis, H. P. A.; van den Bleek, C. M.; Kapteijn, F.; Moulijn, J. A.; Geus, E. R.; van der Puil, N., Zeolitic Coatings and Their Potential Use in Catalysis. *Microporous and Mesoporous Materials* **1998,** 21, (4–6), 213-226.

47. Hedlund, J.; Sterte, J.; Anthonis, M.; Bons, A.-J.; Carstensen, B.; Corcoran, N.; Cox, D.; Deckman, H.; De Gijnst, W.; de Moor, P.-P.; Lai, F.; McHenry, J.; Mortier, W.; Reinoso, J.; Peters, J., High-flux MFI Membranes. *Microporous and Mesoporous Materials* **2002,** 52, (3), 179-189.

48. Weisz, P. B.; Frilette, V. J.; Maatman, R. W.; Mower, E. B., Catalysis by Crystalline Aluminosilicates II. Molecular-Shape Selective Reactions. *Journal of Catalysis* **1962,** 1, (4), 307-312.

49. Weisz, P. B.; Frilette, V. J., Intracrystalline and Molecular-Shape-Selective Catalysis by Zeolite Salts. *The Journal of Physical Chemistry* **1960,** 64, (3), 382-382.

50. Ren, N.; Yang, Y.-H.; Shen, J.; Zhang, Y.-H.; Xu, H.-L.; Gao, Z.; Tang, Y., Novel, Efficient Hollow Zeolitically Microcapsulized Noble Metal Catalysts. *Journal of Catalysis* **2007,** 251, (1), 182-188.

51. Collier, P.; Golunski, S.; Malde, C.; Breen, J.; Burch, R., Active-Site Coating for Molecular Discrimination in Heterogeneous Catalysis. *Journal of the American Chemical Society* **2003,** 125, (41), 12414-12415.

52. Bell, A. T.; Foley, H. C.; Lafyatis, D. S.; Mariwala, R. K.; Sonnichsen, G. D.; Brake, L. D., Chemical Reaction Engineering: Science & Technology Shape selective methylamines synthesis: Reaction and diffusion in a CMs-SiO_2-Al_2O_3 composite catalyst. *Chemical Engineering Science* **1994,** 49, (24), 4771-4786.

53. He, J.; Yoneyama, Y.; Xu, B.; Nishiyama, N.; Tsubaki, N., Designing a Capsule Catalyst and its Application for Direct Synthesis of Middle Isoparaffins. *Langmuir* **2005,** 21, (5), 1699-1702.

54. Ke, C.; Yang, W. L.; Ni, Z.; Wang, Y. J.; Tang, Y.; Gu, Y.; Gao, Z., Electrophoretic Assembly of Nanozeolites: Zeolite Coated Fibers and Hollow Zeolite Fibers. *Chemical Communications* **2001**, (8), 783-784.

55. Devi, R. N.; Meunier, F. C.; Le Goaziou, T.; Hardacre, C.; Collier, P. J.; Golunski, S. E.; Gladden, L. F.; Mantle, M. D., Modulating the Selectivity for CO and Butane Oxidation Over Heterogeneous Catalysis through Amorphous Catalyst Coatings. *The Journal of Physical Chemistry C* **2008,** 112, (29), 10968-10975.

56. Sartipi, S.; van Dijk, J. E.; Gascon, J.; Kapteijn, F., Toward Bifunctional Catalysts for the Direct Conversion of Syngas to Gasoline Range Hydrocarbons: H-ZSM-5 Coated Co Versus H-ZSM-5 Supported Co. *Applied Catalysis A: General* **2013,** 456, 11-22.

57. Miyamoto, M.; Kamei, T.; Nishiyama, N.; Egashira, Y.; Ueyama, K., Single Crystals of ZSM-5/Silicalite Composites. *Advanced Materials* **2005,** 17, (16), 1985-1988.

58. Nishiyama, N.; Ichioka, K.; Park, D.-H.; Egashira, Y.; Ueyama, K.; Gora, L.; Zhu, W.; Kapteijn, F.; Moulijn, J. A., Reactant-Selective Hydrogenation Over Composite Silicalite-1-Coated Pt/TiO_2 Particles. *Industrial & Engineering Chemistry Research* **2004,** 43, (5), 1211-1215.

59. Liang, X.; Yu, M.; Li, J.; Jiang, Y.-B.; Weimer, A. W., Ultra-thin Microporous–mesoporous Metal Oxide Films Prepared by Molecular Layer Deposition (MLD). *Chemical Communications* **2009**, (46), 7140-7142.

60. Liang, X.; Evanko, B. W.; Izar, A.; King, D. M.; Jiang, Y.-B.; Weimer, A. W., Ultrathin Highly Porous Alumina Films Prepared by Alucone ABC Molecular Layer Deposition (MLD). *Microporous and Mesoporous Materials* **2013,** 168, 178-182.

61. Iguchi, E.; Tokuda, Y.; Nakatsugawa, H.; Munakata, F., Electrical Transport Properties in $LiMn_2O_4$, $Li_{0.95}Mn_2O_4$, and $LiMn_{1.95}B_{0.05}O_4$ (B=Al or Ga) Around Room Temperature. *Journal of Applied Physics* **2002,** 91, (4), 2149-2154.

62. Lei, J.; Li, L.; Kostecki, R.; Muller, R.; McLarnon, F., Characterization of SEI Layers on $LiMn_2O_4$ Cathodes with In Situ Spectroscopic Ellipsometry. *Journal of The Electrochemical Society* **2005,** 152, (4), A774-A777.

63. Cho, J.; Kim, T.-J.; Kim, Y. J.; Park, B., Complete Blocking of Mn^{3+} Ion Dissolution from a $LiMn_2O_4$ Spinel Intercalation Compound by Co_3O_4 Coating. *Chemical Communications* **2001**, (12), 1074-1075.

64. Zhuang, Q.-C.; Wei, T.; Du, L.-L.; Cui, Y.-L.; Fang, L.; Sun, S.-G., An Electrochemical Impedance Spectroscopic Study of the Electronic and Ionic Transport Properties of Spinel $LiMn_2O_4$. *The Journal of Physical Chemistry C* **2010,** 114, (18), 8614-8621.

65. Li, X.; Liu, J.; Meng, X.; Tang, Y.; Banis, M. N.; Yang, J.; Hu, Y.; Li, R.; Cai, M.; Sun, X., Significant Impact on Cathode Performance of Lithium-Ion Batteries by Precisely Controlled Metal Oxide Nanocoatings via Atomic Layer Deposition. *Journal of Power Sources* **2014,** 247, 57-69.

66. Liu, Q.; Wang, S.; Tan, H.; Yang, Z.; Zeng, J., Preparation and Doping Mode of Doped $LiMn_2O_4$ for Li-Ion Batteries. *Energies* **2013,** 6, (3), 1718-1730.

67. Tucker, M. C.; Reimer, J. A.; Cairns, E. J., A 7Li NMR Study of Capacity Fade in Metal-Substituted Lithium Manganese Oxide Spinels. *Journal of The Electrochemical Society* **2002,** 149, (5), A574-A585.

68. Lee, Y.-S.; Yoshio, M., Unique Aluminum Effect of $LiAl_xMn_{2-x}O_4$ Material in the 3 V Region. *Electrochemical and Solid-State Letters* **2001,** 4, (7), A85-A88.

69. Aurbach, D.; Levi, M. D.; Gamulski, K.; Markovsky, B.; Salitra, G.; Levi, E.; Heider, U.; Heider, L.; Oesten, R., Capacity Fading of $Li_xMn_2O_4$ Spinel Electrodes Studied by XRD and Electroanalytical Techniques. *Journal of Power Sources* **1999,** 81–82, 472-479.

70. Thackeray, M. M., Manganese Oxides for Lithium Batteries. *Progress in Solid State Chemistry* **1997,** 25, (1–2), 1-71.

71. Sun, Y. K.; Yoon, C. S.; Kim, C. K.; Youn, S. G.; Lee, Y. S.; Yoshio, M.; Oh, I. H., Degradation Mechanism of Spinel $LiAl_{0.2}Mn_{1.8}O_4$ Cathode Materials on High Temperature Cycling. *Journal of Materials Chemistry* **2001,** 11, (10), 2519-2522.

72. Amatucci, G.; Du Pasquier, A.; Blyr, A.; Zheng, T.; Tarascon, J. M., The Elevated Temperature Performance of the $LiMn_2O_4$/C System: Failure and Solutions. *Electrochimica Acta* **1999,** 45, (1–2), 255-271.

73. Thackeray, M. M.; Johnson, C. S.; Kahaian, A. J.; Kepler, K. D.; Vaughey, J. T.; Shao-Horn, Y.; Hackney, S. A., Stabilization of Insertion Electrodes for Lithium Batteries. *Journal of Power Sources* **1999,** 81–82, 60-66.

74. Cho, J.; Kim, G., Enhancement of Thermal Stability of $LiCoO_2$ by $LiMn_2O_4$ Coating. *Electrochemical and Solid-State Letters* **1999,** 2, (6), 253-255.

75. Ha, H.-W.; Yun, N. J.; Kim, K., Improvement of Electrochemical Stability of $LiMn_2O_4$ by CeO_2 Coating for Lithium-Ion Batteries. *Electrochimica Acta* **2007,** 52, (9), 3236-3241.

76. Guan, D.; Jeevarajan, J. A.; Wang, Y., Enhanced Cycleability of $LiMn_2O_4$ Cathodes by Atomic Layer Deposition of Nanosized-thin Al_2O_3 Coatings. *Nanoscale* **2011,** 3, (4), 1465-1469.

77. Park, S.-C.; Kim, Y.-M.; Han, S.-C.; Ahn, S.; Ku, C.-H.; Lee, J.-Y., The Elevated Temperature Performance of $LiMn_2O_4$ Coated with $LiNi_{1-X}Co_XO_2$ (X = 0.2 and 1). *Journal of Power Sources* **2002,** 107, (1), 42-47.

78. Li, J.-g.; He, X.-m.; Zhao, R.-s., Electrochemical Performance of SrF_2-Coated $LiMn_2O_4$ Cathode Material for Li-Ion Batteries. *Transactions of Nonferrous Metals Society of China* **2007,** 17, (6), 1324-1327.

79. Jung, Y. S.; Cavanagh, A. S.; Dillon, A. C.; Groner, M. D.; George, S. M.; Lee, S.-H., Enhanced Stability of $LiCoO_2$ Cathodes in Lithium-Ion Batteries Using Surface Modification by Atomic Layer Deposition. *Journal of The Electrochemical Society* **2010,** 157, (1), A75.

80. Xu, K.; von Cresce, A., Interfacing Electrolytes with Electrodes in Li Ion Batteries. *Journal of Materials Chemistry* **2011,** 21, (27), 9849.

81. Aurbach, D.; Ein-Eli, Y.; Chusid, O.; Carmeli, Y.; Babai, M.; Yamin, H., The Correlation Between the Surface Chemistry and the Performance of Li-Carbon Intercalation Anodes for Rechargeable 'Rocking-Chair' Type Batteries. *Journal of The Electrochemical Society* **1994,** 141, (3), 603-611.

82. Levi, M. D.; Gamolsky, K.; Aurbach, D.; Heider, U.; Oesten, R., On Electrochemical Impedance Measurements of $Li_xCo_{0.2}Ni_{0.8}O_2$ and Li_xNiO_2 Intercalation Electrodes. *Electrochimica Acta* **2000,** 45, (11), 1781-1789.

83. Wang, H.-Y.; Wang, F.-M., Electrochemical Investigation of an Artificial Solid Electrolyte Interface for Improving the Cycle-Ability of Lithium Ion Batteries Using an Atomic Layer Deposition on a Graphite Electrode. *Journal of Power Sources* **2013,** 233, 1-5.

84. Amine, K.; Tukamoto, H.; Yasuda, H.; Fujita, Y., A New Three-Volt Spinel $Li_{1+x}Mn_{1.5}Ni_{0.5}O_4$ for Secondary Lithium Batteries. *Journal of The Electrochemical Society* **1996,** 143, (5), 1607-1613.

85. Pasero, D.; Reeves, N.; Pralong, V.; West, A., Oxygen Nonstoichiometry and Phase Transitions in $LiMn_{1.5}Ni_{0.5}O_{4-\delta}$. *Journal of The Electrochemical Society* **2008,** 155, (4), A282-A291.

PAPER

I. Highly porous titania films coated on sub-micron particles with tunable thickness by molecular layer deposition in a fluidized bed reactor

Rajankumar L. Patel [a], Ying-Bing Jiang [b], and Xinhua Liang [a,*]

[a] Department of Chemical and Biochemical Engineering, Missouri University of Science and Technology, Rolla, Missouri 65409, USA

[b] TEM Laboratory, University of New Mexico, Albuquerque, New Mexico 87131, USA
* To whom correspondence should be addressed. E-mail: liangxin@mst.edu

Abstract

Titanium alkoxide (titanicone) thin films were coated on large quantities of sub-micron sized silica particles at 100 ºC using molecular layer deposition (MLD) in a fluidized bed reactor. Titanium tetrachloride and ethylene glycol were used as precursors. The content of titanium on the particles increased linearly as the number of MLD coating cycles increased. The conformity of the films, with a thickness of ~12 nm, was verified by TEM for silica particles coated with 50 cycles of titanicone. The composition of the titanicone films was confirmed by EDS. Porous titanium oxide films were formed for the particles coated with 50 cycles of titanicone MLD by oxidation in air at 400 °C or by decomposition of the organic components of the titanicone films in the presence of water. The thicknesses of the films were reduced from ~12 nm to ~8 nm after oxidation in air at 400 °C for 1 hr. The effect of aging on the titanicone films was studied at different lengths of aging time in the presence of water. A greatly increased surface area of 48.8 m^2g^{-1} was obtained for the particles exposed to water for 24 hr, compared to the as-deposited 50 cycles of titanicone coated sample with a surface area of 7.7 m^2g^{-1}. The decomposition of titanicone films, after exposure to water vapor for various lengths of time, was studied by FTIR.

Keywords: Ultra-thin; Porous film; Molecular layer deposition (MLD); Titanium alkoxide (titanicone); Titanium oxide (titania); Fluidized bed reactor

1. Introduction

Titania possesses properties like chemical inertia [1] and high surface affinity towards ligands [2, 3]. Its optical and electronic activities make it an extremely attractive material for a great variety of applications, including pigments [4, 5], photocatalysts [6, 7], and energy conversion [8, 9]. Many applications (e.g., solar cells, sensors, etc.) require processing of thin films with high surface areas, high porosity, and high purity to obtain improved device efficiency [8-12]. Fabrication control of porous titania films is significant since it can impart a profound effect on surface reactions and fine tuning of material properties [6, 13, 14]. Currently, most of the preparation methods used involve organic templates. Organic-inorganic films are prepared first, and the organic templates must be removed gently by calcination at high temperature in order to create porous structures. Sol-gel [15], self-assembly [16, 17], layer-by-layer assembly [18], and Langmuir-Blodgett [19] were each developed for fabricating polymeric thin films. Although these techniques can fabricate organic-inorganic films, often they lack a porous framework with structural integrity, precise composition, and thickness control.

Similar to atomic layer deposition (ALD), the vapor-phase molecular layer deposition (MLD) approach is ideal for the deposition of organic or organic-inorganic hybrid materials [20-24]. This MLD approach utilizes alternating self-limiting heterogeneous surface reactions to build up a solid-state thin film through a sequence of molecular adsorption/reaction steps. This process allows a film to be conformally constructed on surfaces with arbitrary shapes and surface areas. MLD can provide precise control over film thickness, composition, and conformity at the molecular level. It has recently been demonstrated that ultra-thin porous aluminum oxide films can be prepared from MLD prepared organic-inorganic hybrid polymer films by removing the organic components [25, 26]. The porosity of the resulting inorganic films will depend on the volume occupied by the organic constituting part. It is expected that ultra-thin porous titania films can also be prepared by a similar process. The MLD chemistry of hybrid organic-inorganic titanium alkoxide (titanicone) films has been reported using alternating reactions of titanium tetrachloride ($TiCl_4$) and ethylene glycol (EG) [27, 28]. The photocatalytic activity of the thermally annealed titanicone film was about a 5-fold increase when compared to that of the TiO_2 film prepared by ALD under optimal processing conditions [28]. Thus far, no study has been conducted for titanicone MLD on a large quantity of particles and their porous film formation.

In this study, ultra-thin titanicone films were coated on primary sub-micron SiO_2 particles. The reason for using particles with such a low surface area is because it was easier to verify the particle surface area increment due to the formation of porous structures from MLD films. This type of porous coating can be used for fine tuning some porous materials, such as zeolite for gas separation [29], and catalysts with enhanced performance (i.e., as increased thermal stability [30], and reaction selectivity [31]). The organic constituents in the films were removed either by calcination in air at elevated temperatures or decomposition in the presence of water at room temperature, which could be very important for coating temperature-sensitive substrates. The resulting porous structures had both micropores and mesopores.

2. Experimental Details

2.1. *MLD of titanicone films*

Titanicone MLD was performed in a fluidized bed reactor, as shown in Fig. 1. This reactor system consisted of a reactor column, a vibration generation system, a gas flow control system, and a data acquisition and control system with LabView®, which has been described in detail previously [24]. Silica powder (500 nm, 99.9%, from Alfa Aesar) was used as the substrate. Titanium tetrachloride (99.9%, from Sigma Aldrich) and ethylene glycol (anhydrous, 99.8%, from Sigma Aldrich) were used as precursors. All of the chemicals were used as received without any treatment. For a typical run, 10 g of particles were loaded into the reactor. The reaction temperature was 100 °C. The minimum fluidization superficial gas velocity was determined by measuring the pressure drop across the particles bed versus the superficial gas velocity of purge gas. The base pressure was ~3.5 Torr at the minimum fluidization velocity. During the MLD reaction, $TiCl_4$ was fed through the distributor of the reactor, based on the driving force of its room-temperature vapor pressure. A needle valve was used to adjust the $TiCl_4$ flow rate and ensure that the $TiCl_4$ pressure was high enough to promote particle fluidization. The reactor was also subjected to vibration via vibrators to improve the quality of particle fluidization during the MLD process. The vapor of EG was delivered into the reactor using a bubbler, which was heated at 65 °C. The feed lines were kept at ~100 °C to avoid excessive adsorption of EG in the internal walls of the system that could promote side-reactions of chemical vapor deposition (CVD).

The entire coating-sequence process was controlled and monitored using a LabView® program. Each MLD coating cycle consisted of six steps: $TiCl_4$ dose (90 s), N_2 flush (600 s), vacuum (30 s); EG dose (720 s), N_2 flush (600 s), and vacuum (30 s). These steps helped ensure that direct contact between the two precursors was avoided and CVD side-reactions were prevented. N_2 gas flow rate was controlled by an MKS mass flow controller during the process. Before the reaction, the particles were outgassed at 100 °C with a continuous N_2 flow for at least 5 hr. The MLD reaction was carried out for 10, 20, 30, 40, and 50 cycles.

In order to form porous MLD films, two post-treatment procedures were applied: thermal annealing and water soaking. The 50 cycles of titanicone MLD coated silica particles were oxidized in air at 400 °C for 1 hr at a heating and cooling rate of 1 °C/min. A different set of the same particles was soaked in deionized water for different lengths of time and then dried under vacuum at room temperature.

2.2. *Characterization*

The coated particles were visualized with an FEI Tecnai F20 field emission gun high resolution TEM/STEM equipped with an energy dispersive X-ray spectrometer (EDS) system. TEM samples were prepared by placing the particles on holey-carbon films supported on Cu grids. To quantify the amount of Ti on the surface of the particles, inductively-coupled plasma atomic emission spectroscopy (ICP-AES) was used. A Perkin-Elmer Optima 7300DV instrument was used to perform ICP-AES. A Quantachrome Autosorb-1 was used to obtain nitrogen adsorption and desorption isotherms at -196 ºC, for the uncoated, and the MLD coated particles before and after the removal of the organic components. Before starting the adsorption measurements, the as-deposited samples were outgassed at 50 ºC under vacuum for 24 hr, and the samples that were water treated and oxidized were outgassed at 120 ºC under vacuum for 24 hr. The specific surface areas of the samples were calculated using the Brunauer–Emmett–Teller (BET) method in a relative pressure range of 0.05–0.25. The pore size distribution curves were derived from the adsorption and desorption isotherms using the Horvath-Kawazoe (HK) and the Barrett–Joyner–Halenda (BJH) methods. The infrared spectroscopy (IR) spectra of the samples were obtained from Nicolet Nexus 470 FT-IR Spectrometer (Thermo Nicolet) in the transmission mode, and continuously purged with purified dry air. Samples were measured with 100 scans at a 4 cm^{-1} resolution.

3. Results and Discussion

3.1. *Growth of titanicone MLD films on* SiO_2

Titanicone films of different thicknesses were coated on SiO_2 particles by controlling the number of MLD cycles. The Ti content on the silica particles of each sample was measured by ICP-AES. As shown in Fig. 2, titanium content followed a linear path with increase in the number of MLD cycles. The titanicone film thickness was much smaller than the sub-micron sized silica particles. This resulted in a linear proportionality between the titanium content and the number of coating cycles. The thicknesses of titanicone films were reflected by the content of Ti on the particles. The linearity of the plot also clearly indicated the layer-by-layer growth of the titanicone MLD films on the substrate particles. Therefore, the thickness of each film can be precisely controlled by the number of MLD coating cycles. No nucleation period was required to deposit MLD coating on the silica particles, because native hydroxyl groups were present on the surfaces of the silica particles. The uniformly deposited titanicone films were directly observed by TEM imaging. As shown in Fig. 3a, the thickness of the film was ~12 nm for particles coated with 50 cycles of MLD coating. This thickness indicated that the growth rate of the titanicone films was ~0.24 nm per $TiCl_4$/EG cycle. This observed growth rate was a bit slower than the reported growth rate of titanicone MLD, which was 0.44 nm/cycle at 100 °C [27]. The composition of the films was directly confirmed by EDS, as shown in Fig. 3b and 3c. The former spectrum is for the silica substrate and the latter one is for the titanicone MLD film.

Most of the primary particles were coated with titanicone films during the coating process, which was indirectly supported by the BET surface area analysis as shown in Fig. 4. The gradual decrease in the surface area of the particles was analogous to the proven results that MLD coating occurred on the primary particles despite of small-sized aggregates [24]. There was no dramatic decrement in surface area with an increase in the number of MLD coating cycles. The surface area of uncoated silica particles gradually decreased from 10.0 m^2g^{-1} to 7.4 m^2g^{-1} for the particles coated with 40 cycles of titanicone film. The surface area did not decrease further beyond 40 cycles of MLD coating. The reduction in surface area before 40 cycles could be explained by the larger particles, density changes, and the slight aggregation of particles after MLD coating. The increase in surface area after 40 cycles could be explained by the partial formation of porous films, which would contribute to higher surface areas of the particles. This similar behavior has also been documented for alucone and zincone films in previous studies [26, 32], where it was found that porous metal oxide films could form during the deposition process.

3.2. *Porous MLD films*

Silica particles coated with 50 cycles of titanicone films were oxidized in air at 400 °C for 1 hr to create porous structures within the films. The TEM image, in Fig. 5, of one such particle confirms the resultant conformal film after oxidation. The surface area of the oxidized particles was 22.0 m^2g^{-1} and this increment can be attributed to the formation of porous structures of TiO_2. During oxidation in air, the organic components should be degraded to create a porous structure of a conformal titania film. As clearly shown in Fig. 3a and 5, the film thickness decreased from ~12 nm to ~8 nm for the oxidized particles. At the oxidation temperature of 400 °C, amorphous titania could be crystallized to form anatase phase titania. Such phase transformation may affect the stability of the porous structure, and result in a lower surface area of porous titania. This set of experiments indicates the potential of the MLD method for the uniform coating of high geometric aspect ratio nanoscale structures. Since thermal annealing of titania results phase change from amorphous to anatase, the MLD technique can also be crucial for the thermal annealing compatibility process [28, 33]. However, the XRD results of the oxidized samples showed no confirmed sign that the anatase phase was present. It seems that the amount of crystalline titania was not substantial enough to be detected by XRD. This could be due to low crystallinity of titania present in the samples, since the samples were heated at 400 °C for only 1 hr and the presence of carbon could have suppressed the phase transition [28].

The particles from the same batch, 50 cycles of titanicone coated silica, were soaked in deionized water for different lengths of time, and then dried. The porous structures of titania particles were studied by nitrogen adsorption and desorption analysis. Fig. 6 shows nitrogen adsorption and desorption isotherms, surface area, pore volume, and pore size distributions of 50 cycles of titanicone MLD coated silica particles after being soaked in water for different lengths of time. The adsorption-desorption isotherm is a type II isotherm, according to the IUPAC recommendations. The pore diameter of the micropores was estimated to be ~0.6 nm by using the HK method. Mesopores, with an estimated diameter of ~1.1 nm by using the BJH method, were also observed. The high surface areas of the water soaked particles were due to the formation of these micropores and mesopores in the films. After being soaked in water for 24 hr, most of the organic components were removed, and the surface area of the porous titania films greatly increased to 48.8 m^2/g, as compared to the surface area of 7.7 m^2/g for the as-deposited silica particles. However, the surfaces of the particles decreased with soaking times longer than 24 hr, which was due to the collapse of micropores and mesopores that formed larger pores and promoted instability of the titania films. It is worthy to mention that the surface area of the titania film itself was much higher, since this was the surface area of 500 nm SiO_2 particles coated with one layer of porous titania film. The TEM image, as shown in Fig. 7, of the silica particle coated with 50 cycles of titanicone MLD film after being soaked in water for 24 hr, revealed that the continuous layer of film had collapsed due to drastic decomposition of the organic components by directly soaking the particles in water. The porous structure was damaged, and the porous film was not conformal.

In order to unfold the decomposition of the titanicone films in the presence of water, 50 cycles of titanicone coated silica particles were exposed to water vapor for different lengths of time and the composition changes of the films were analyzed by FTIR. As shown in Fig. 8, a broad absorption peak was seen at 3100–3800 cm^{-1}, which was assigned to the stretching modes of O–H bands and related to free water (capillary pore water and surface absorbed water) [34]. The peak at ~1620 cm^{-1} was due to the bending vibration of the H–O–H bond, which was assigned to the –OH present in the sample. In all samples, a band at 1000–1250 cm^{-1} was clearly visible, and was assigned to the asymmetric stretching vibrations of the Si–O–Si band [34]. The two absorption peaks between 760–950 cm^{-1} were ascribed to the symmetric vibrations of the stretching Si–O–Ti band. In the low-frequency region, the appearance of low intensity at 500 cm^{-1} indicated the Ti−O−Ti modes. The peaks related to the $–CH_3$ and $–CH_2$ groups were observed at 1367, 1532, and 2950 cm^{-1}. An indicative peak at ~1880 cm^{-1} showed a possible alkene (–CH=CH–) group stretching. Over a period of more than 24 hr, these components were decomposed in the presence of water, as evident from the FTIR. The series of FTIR spectra, for the samples exposed to water vapor for different lengths of time, elucidated the presence of organic components in the titanicone films and their decomposition after their exposure to water vapor. This finding also confirms that the titanicone films became titania films after removal of that organic components. It also explains the increase in the surface areas of the titania films after 24 hr water vapor exposure, which was the result of space left after decomposition of the organic components.

4. Conclusions

Sub-micron silica particles were coated with ultra-thin titanicone films by MLD at 100 ºC in a fluidized bed reactor. TEM and EDS studies confirmed the conformality and the composition of the titanicone MLD films, respectively. Porous titania films were created by oxidizing the MLD coated particles in air at 400 °C or by decomposition in the presence of water. The surface area was increased from 7.7 m^2g^{-1} for the as-deposited 50 cycles titanicone MLD coated silica particles to 22.0 m^2g^{-1} for the particles oxidized at 400 °C, and to 48.8 m^2g^{-1} for the sample after being soaked in water for 24 hr. The lower surface areas of the oxidized particles were due to the phase transformation of amorphous titania to anatase titania at the oxidation temperature of 400 °C. The decomposition of organic components was studied by FTIR for titanicone films exposed to water vapor for different lengths of time. This study demonstrated a process for preparing porous titania films with a tunable thickness, which could have many potential applications, such as catalysis, separation, sensing, and energy conversion and storage.

Acknowledgments

This work was supported in part by the National Science Foundation grant NSF CBET 1402122 and the Materials Research Center at the Missouri University of Science and Technology.

References

[1] D. Grosso, G. J. d. A. A. Soler-Illia, E. L. Crepaldi, F. Cagnol, C. Sinturel, A. Bourgeois, A. Brunet-Bruneau, H. Amenitsch, P. A. Albouy, C. Sanchez, Highly porous TiO_2 anatase optical thin films with cubic mesostructure stabilized at 700 °C, *Chemistry of Materials* 15 (2003) 4562-4570.

[2] A. Hagfeldt, M. Grätzel, Molecular photovoltaics, *Accounts of Chemical Research* 33 (2000) 269-277.

[3] F. Campus, P. Bonhôte, M. Grätzel, S. Heinen, L. Walder, Electrochromic devices based on surface-modified nanocrystalline TiO_2 thin-film electrodes, *Solar Energy Materials and Solar Cells* 56 (1999) 281-297.

[4] K. Akiyama, N. Toyama, K. Muraoka, M. Tsunashima, Configurational observation of titanium oxide pigment particles, *Journal of the American Ceramic Society* 81 (1998) 1071-1073.

[5] S.-J. Kim, D. E. McKean, Aqueous TiO_2 suspension preparation and novel application of ink-jet printing technique for ceramics patterning, *Journal of Materials Science Letters* 17 (1998) 141-144.

[6] M. A. Carreon, S. Y. Choi, M. Mamak, N. Chopra, G. A. Ozin, Pore architecture affects photocatalytic activity of periodic mesoporous nanocrystalline anatase thin films, *Journal of Materials Chemistry* 17 (2007) 82-89.

[7] Z. Ding, X. Hu, G. Q. Lu, P.-L. Yue, P. F. Greenfield, Novel silica gel supported TiO_2 photocatalyst synthesized by CVD method, *Langmuir* 16 (2000) 6216-6222.

[8] B. O'regan, M. Grfitzeli, A low-cost, high-efficiency solar cell based on dye-sensitized, *Nature* 353 (1991) 737-740.

[9] L. Kavan, J. Rathouský, M. Grätzel, V. Shklover, A. Zukal, Surfactant-templated TiO_2 (anatase): Characteristic features of lithium insertion electrochemistry in organized nanostructures, *Journal of Physical Chemistry B* 104 (2000) 12012-12020.

[10] K. M. Coakley, Y. Liu, M. D. McGehee, K. L. Frindell, G. D. Stucky, Infiltrating semiconducting polymers into self-assembled mesoporous titania films for photovoltaic applications, *Advanced Functional Materials* 13 (2003) 301-306.

[11] E. Stathatos, Y. Chen, D. D. Dionysiou, Quasi-solid-state dye-sensitized solar cells employing nanocrystalline TiO_2 films made at low temperature, *Solar Energy Materials and Solar Cells* 92 (2008) 1358-1365.

[12] D. Zhang, T. Yoshida, T. Oekermann, K. Furuta, H. Minoura, Room-temperature synthesis of porous nanoparticulate TiO_2 films for flexible dye-sensitized solar cells, *Advanced Functional Materials* 16 (2006) 1228-1234.

[13] X. H. Liang, R. L. Patel, Porous titania microspheres with uniform wall thickness and high photoactivity, *Ceramics International* 40 (2014) 3097-3103.

[14] E. J. Crossland, N. Noel, V. Sivaram, T. Leijtens, J. A. Alexander-Webber, H. J. Snaith, Mesoporous TiO_2 single crystals delivering enhanced mobility and optoelectronic device performance, *Nature* 495 (2013) 215-219.

[15] K.-N. P. Kumar, J. Kumar, K. Keizer, Effect of peptization on densification and phase-transformation behavior of sol–gel-derived nanostructured titania, *Journal of the American Ceramic Society* 77 (1994) 1396-1400.

[16] C. Sanchez, C. Boissière, D. Grosso, C. Laberty, L. Nicole, Design, synthesis, and properties of inorganic and hybrid thin films having periodically organized nanoporosity, *Chemistry of Materials* 20 (2008) 682-737.

[17] O. Sel, D. Kuang, M. Thommes, B. Smarsly, Principles of hierarchical meso-and macropore architectures by liquid crystalline and polymer colloid templating, *Langmuir* 22 (2006) 2311-2322.

[18] T. Sasaki, Y. Ebina, T. Tanaka, M. Harada, M. Watanabe, G. Decher, Layer-by-layer assembly of titania nanosheet/polycation composite films. *Chemistry of Materials* 13 (2001) 4661-4667.

[19] J. Sánchez-González, J. Ruiz-Garcıa, M. Gálvez-Ruiz, Langmuir–Blodgett films of biopolymers: a method to obtain protein multilayers, *Journal of Colloid and Interface Science* 267 (2003) 286-293.

[20] T. Yoshimura, S. Tatsuura, W. Sotoyama, Polymer-films formed with monolayer growth steps by molecular layer deposition, *Applied Physics Letters* 59 (1991) 482-484.

[21] T. Yoshimura, S. Tatsuura, W. Sotoyama, A. Matsuura, T. Hayano, Quantum wire and dot formation by chemical vapor-deposition and molecular layer deposition of one-dimensional conjugated polymer, *Applied Physics Letters* 60 (1992) 268-270.

[22] Y. Du, S. M. George, Molecular layer deposition of nylon 66 films examined using in situ FTIR spectroscopy, *Journal of Physical Chemistry C* 111 (2007) 8509-8517.

[23] Q. Peng, B. Gong, R. M. VanGundy, G. N. Parsons, "Zincone" zinc oxide-organic hybrid polymer thin films formed by molecular layer deposition, *Chemistry of Materials* 21 (2009) 820-830.

[24] X. H. Liang, D. M. King, P. Li, S. M. George, A. W. Weimer, Nanocoating hybrid polymer films on large quantities of cohesive nanoparticles by molecular layer deposition, *AIChE Journal* 55 (2009) 1030-1039.

[25] X. H. Liang, M. Yu, J. H. Li, Y. B. Jiang, A. W. Weimer, Ultra-thin microporous–mesoporous metal oxide films prepared by molecular layer deposition (MLD), *Chemical Communications* 46 (2009) 7140-7142.

[26] X. H. Liang, B. W. Evanko, A. Izar, D. M. King, Y. B. Jiang, A. W. Weimer, Ultrathin highly porous alumina films prepared by alucone ABC molecular layer deposition (MLD), *Microporous and Mesoporous Materials* 168 (2013) 178–182.

[27] A. I. Abdulagatov, R. A. Hall, J. L. Sutherland, B. H. Lee, A. S. Cavanagh, S. M. George, Molecular layer deposition of titanicone films using $TiCl_4$ and ethylene glycol or glycerol: growth and properties, *Chemistry of Materials* 24 (2012) 2854-2863.

[28] S. Ishchuk, D. H. Taffa, O. Hazut, N. Kaynan, R. Yerushalmi, Transformation of organic–inorganic hybrid films obtained by molecular layer deposition to photocatalytic layers with enhanced activity, *ACS Nano* 6 (2012) 7263-7269.

[29] M. Yu, H. H. Funke, R. D. Noble, J. L. Falconer, H_2 separation using defect-free, inorganic composite membranes, *Journal of the American Chemical Society* 133 (2011) 1748–1750.

[30] X. H. Liang, J. H. Li, M. Yu, C. N. McMurray, J. L. Falconer, A. W. Weimer, Stabilization of supported metal nanoparticles using an ultrathin porous shell, *ACS Catalysis* 1 (2011) 1162-1165.

[31] Z. Y. Shang, R. L. Patel, B. W. Evanko, X. H. Liang, Encapsulation of supported metal nanoparticles with an ultra-thin porous shell for size-selective reactions, *Chemical Communications* 49 (2013) 10067-10069.

[32] X. H. Liang, Y. B. Jiang, A. W. Weimer, Nanocoating zinc alkoxide (zincone) hybrid polymer films on particles using a fluidized bed reactor, *Journal of Vacuum Science & Technology A* 30 (2012) 01A108.

[33] Y. Yu, J. Wang, J. F. Parr, Preparation and properties of TiO_2/fumed silica composite photocatalytic materials, *Procedia Engineering* 27 (2012), 448-456.

[34] W. Gu, C. P. Tripp, Role of water in the atomic layer deposition of TiO_2 on SiO_2, *Langmuir* 21 (2005) 211-216.

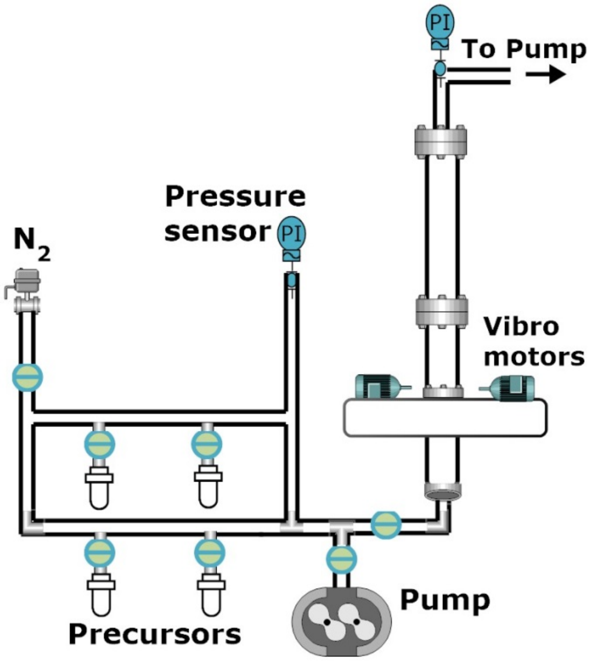

Fig. 1. Schematic of MLD fluidized bed reactor.

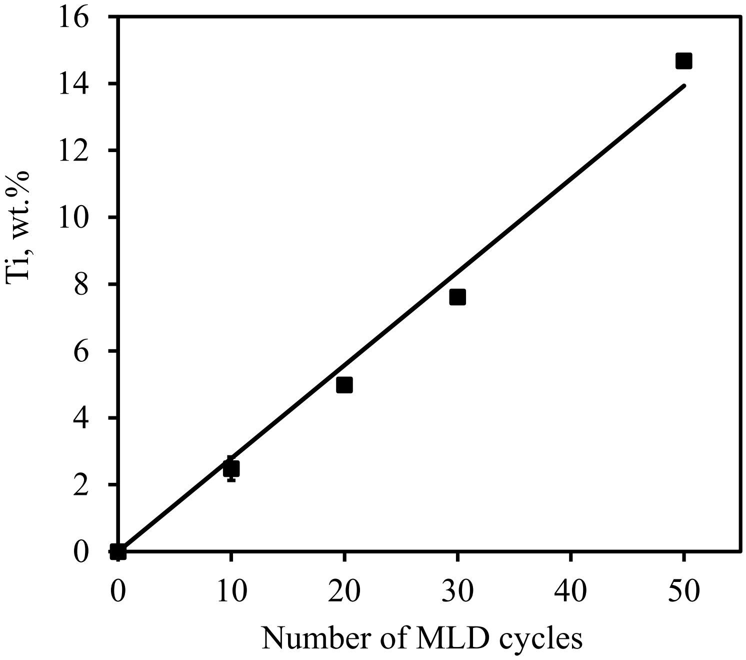

Fig. 2. Titanium content on 500 nm silica particles versus the number of MLD-coating cycles.

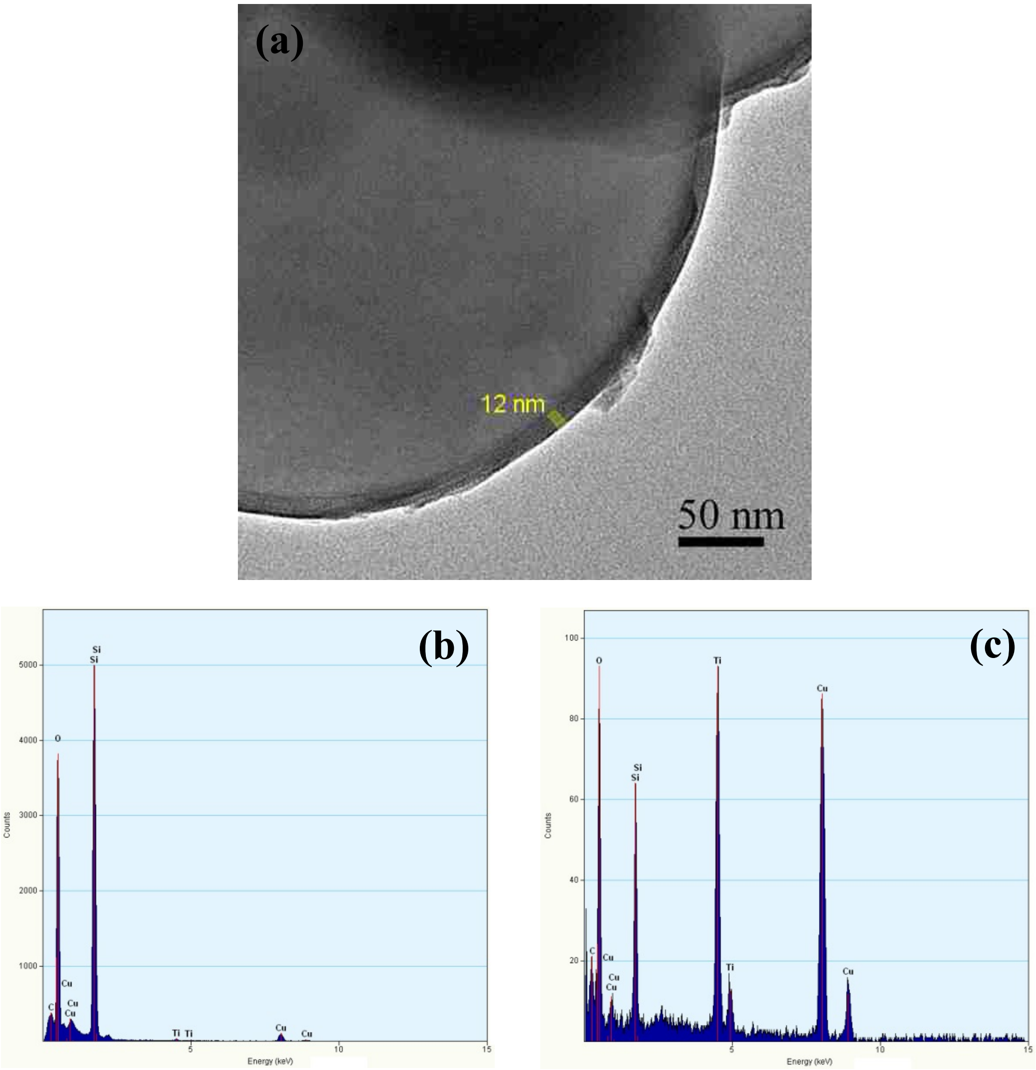

Fig. 3. (a) TEM image of one 500 nm silica particle coated with 50 cycles of titanicone MLD film and EDS spectra of (b) the silica substrate and (c) the titanicone MLD film.

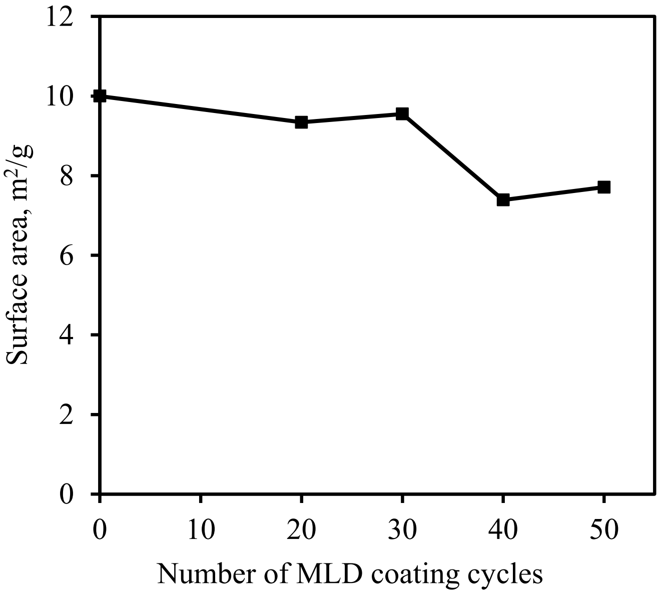

Fig. 4. Surface area of silica particles versus the number of MLD coating cycles.

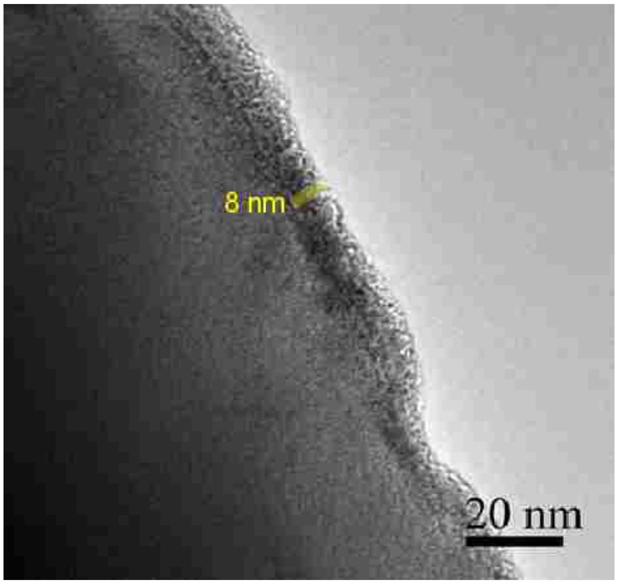

Fig. 5. TEM image of one 500 nm silica particle coated with 50 cycles of titanicone MLD film after oxidation in air at 400 ºC for 1 hr.

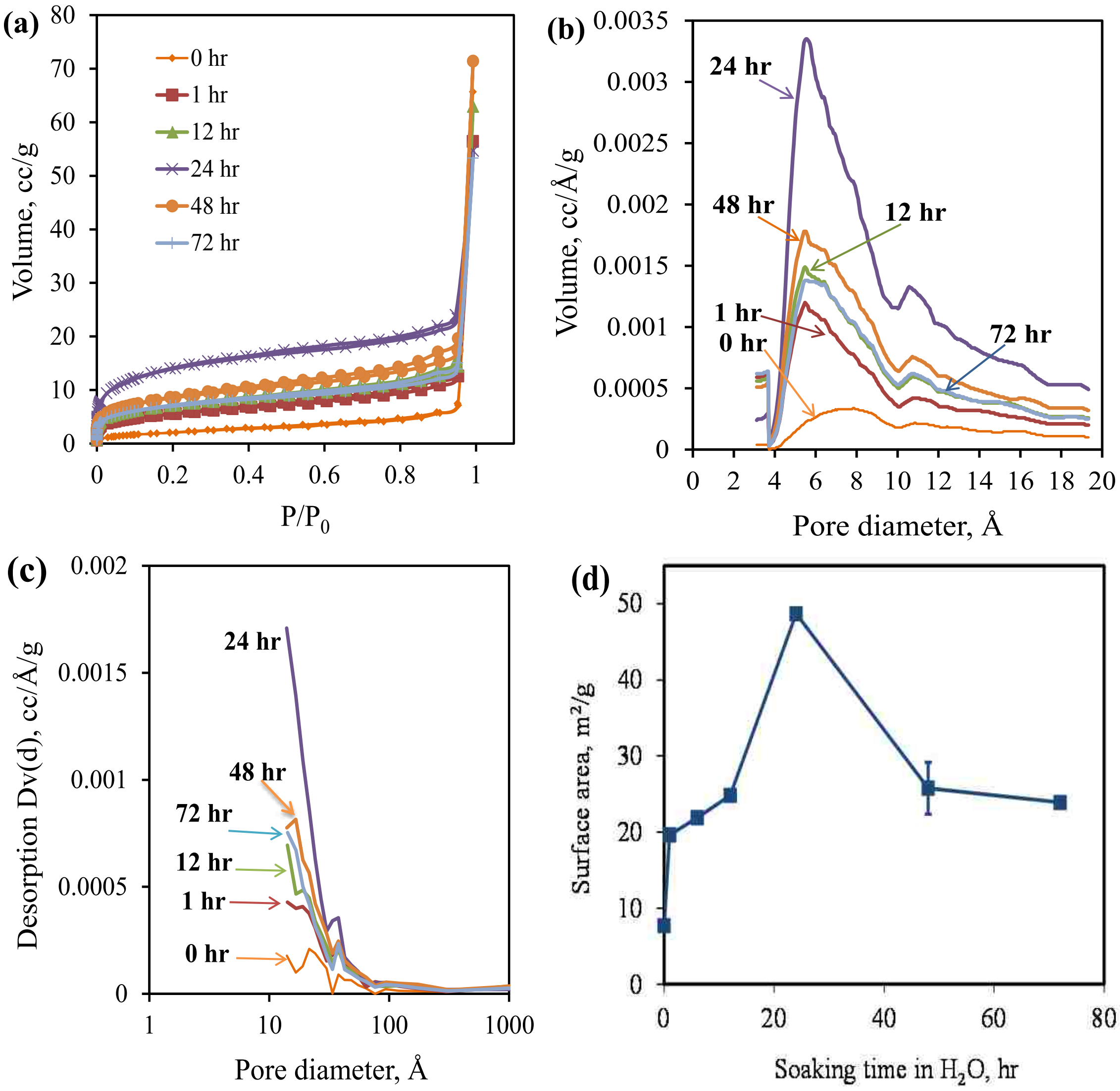

Fig. 6. (a) Nitrogen adsorption and desorption isotherms, pore size distributions of (b) micropores and (c) mesopores, and (d) surface area of silica particles coated with 50 cycles of titanicone MLD film after being soaked in water for different lengths of time.

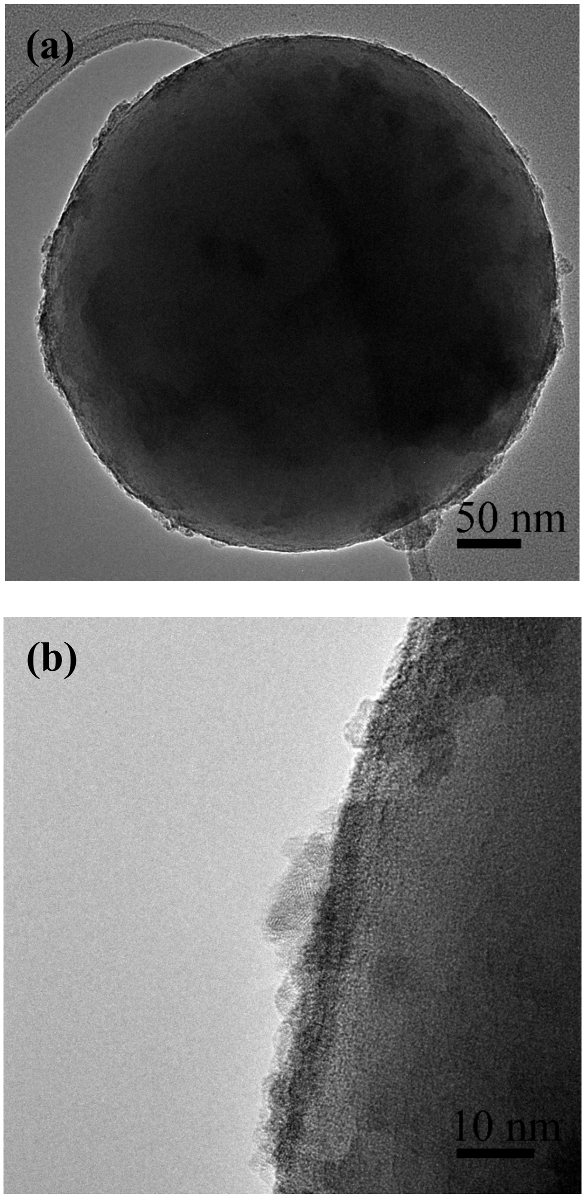

Fig. 7. (a, b) TEM images of one 500 nm silica particle coated with 50 cycles of titanicone MLD film after being soaked in water for 24 hr.

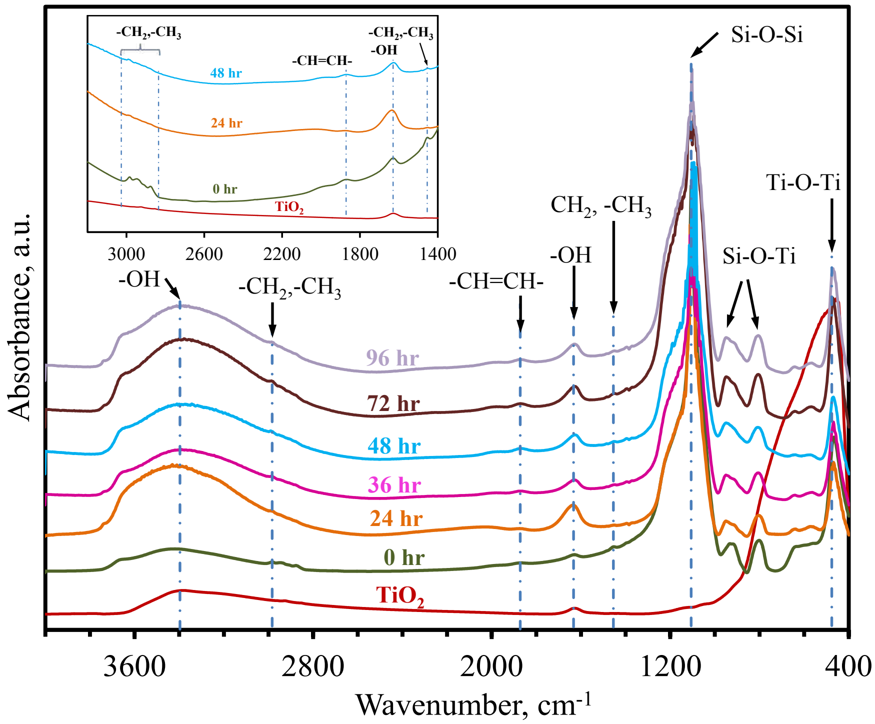

Fig. 8. FTIR spectra of silica particles coated with 50 cycles of titanicone MLD film after being exposed to water vapor for different lengths of time. The inset spectra clearly show the presence of $-CH_2$, $-CH_3$ groups on the as-deposited silica particles.

II. Encapsulation of supported metal nanoparticles with an ultra-thin porous shell for size-selective reactions

Zeyu Shang[1], Rajankumar L. Patel[1], Brian W. Evanko and Xinhua Liang

Department of Chemical and Biochemical Engineering, Missouri University of Science and Technology, Rolla, Missouri 65409, USA.

Tel: 1-573-341-7632; E-mail: liangxin@mst.edu

[1]Both authors contributed equally to this work.

Abstract

A novel nanostructured catalyst with an ultra-thin porous shell obtained from the thermal decomposition of an aluminium alkoxide film deposited by molecular layer deposition for size-selective reactions was developed. The molecular sieving capability of the porous metal oxide films was verified by examining the liquid-phase hydrogenation of n-hexene versus cis-cyclooctene.

Heterogeneous catalysts are widely used (e.g., producing fertilizers, making gasoline from petroleum, and controlling automotive exhaust pollution via the catalytic muffler). However, heterogeneous catalysts cannot selectively convert specific molecules in the reactants mixture to catalyze only desired reactions.[1] Size-selective catalysts with a metal core and porous oxide shell have a promising structure that can increase the reaction selectivity through reactant molecular discrimination.[1-2]

Current research activities in this area are mainly focused on encapsulating unsupported catalysts or nanoparticles supported on dense catalyst supports.[2-3] Nishiyama et al.[2a] applied an aqueous solution of fumed silica, ethanol, and tetrapropylammonium hydroxide (TPAOH) to synthesize silicalite-1 coatings on spherical Pt/TiO_2 particles with a diameter of 0.5 mm under hydrothermal conditions. The thickness of the silicalite-1 layer was about 40 μm. Yang et al.[2b] developed a size-selective catalyst with a core-shell structure, where a Pd-containing silica core was surrounded by a silica shell in the presence of a cationic surfactant. This catalyst showed good activity and selectivity in the benzyl alcohol aerobic oxidation. Lu et al.[3] encapsulated unsupported surfactant-capped Pt nanoparticles by a zeolitic imidazolate framework (ZIF-8) with an average pore size of about 1.2 nm and a film thickness of about 200 nm. The ZIF-8 porous coating greatly increased the selectivity towards hydrogenation of n-hexene over cis-cyclooctene. However, compared to the naked catalyst, there was a 60% conversion loss for n-hexene hydrogenation mainly due to the mass diffusion barrier from the relatively thick ZIF-8 coating.

Normally, heterogeneous catalysts consist of small metal particles dispersed on a high surface area porous oxide support. The support maximizes the number of metal atoms at a surface, since metal atoms in the bulk are not involved in catalytic reactions. Traditional methods like hydrothermal synthesis[4] and sol-gel processes[5] can prepare inorganic coatings with few defects, such as zeolite membranes and mesoporous films. However, it is difficult for these methods to deposit ultra-thin porous films inside the porous structure of the catalyst supports and control the thickness of the films with nanometer precision.

It is highly desirable to develop a new strategy to prepare an ultra-thin porous film with controllable pore size and a limited mass diffusion barrier. Lu et al.[6] showed that ultra-thin porous alumina films could be formed from dense atomic layer deposited (ALD) alumina films by thermal treatment at 700 ºC. The pore size was about 2 nm. The formation of the porous structure was a result of the heat treatment process and there was no control over pore size. Canlas et al.[7] prepared shape-selective sieving layers on an oxide catalyst surface by grafting the catalyst particles with bulky single-molecule sacrificial templates with submonolayer coverage, then partially overcoating the catalyst with alumina through ALD. The number of the nanocavities was controlled by the number of template molecules grafted on the catalyst surface. The size of the nanocavities was controlled by the size of the template molecule and the thickness of ALD films. Although they achieved good conversion and selectivity for photooxidation of certain alcohols, their technique requires rigid molecules with certain surface orientations as sacrificial templates and many steps are needed to prepare the shape-selective sieving layers.

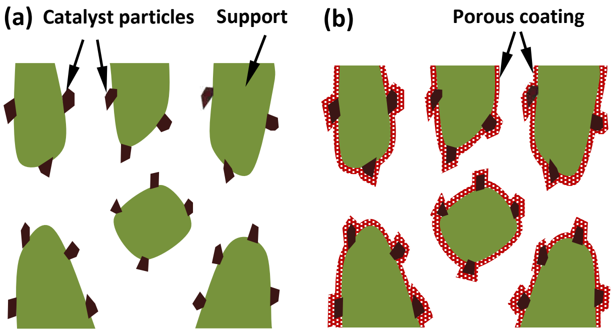

Fig. 1. Schematic representation of supported metal catalysts (a) before and (b) after a porous coating on all surfaces of the catalyst particles.

Recently, one novel method was developed by Liang et al. to prepare ultra-thin porous aluminium oxide films formed from the calcination of aluminium alkoxide (alucone) films, which were deposited by molecular layer deposition (MLD) using trimethylaluminium (TMA) and ethylene glycol (EG) as precursors.[8] The average pore size of porous alumina was about 0.6 nm (more than 95%).[8] MLD is a layer-by-layer gas phase thin film coating technique, which has been utilized to deposit pure polymer films or hybrid polymer films with nanometer-sized control of film thickness and well controlled film composition.[9] The self-limiting nature of MLD makes it ideal for coating porous substrates where line-of-sight gas phase deposition methods fail. Herein, we prepared Pt/SiO_2 catalysts encapsulated by an ultra-thin porous alumina film by MLD, as schematically shown in Fig. 1. Due to the conformal oxide coverage and sub-nanometer pores, the reaction rates of larger reactants should be slowed because they diffuse much more slowly than the smaller reactants through the oxide layer. Since the porous film is only several nanometers thick, the mass diffusion barrier for the smaller molecules is minimal. The combination of the catalytic properties of Pt nanoparticles and the molecular sieving capability of the porous oxide films was evaluated by examining the liquid-phase hydrogenation of n-hexene versus cis-cyclooctene.

The Pt nanoparticles were deposited on mesoporous silica particles by ALD using methylcyclopentadienyl-(trimethyl) platinum(IV) ($MeCpPt\text{-}Me_3$) and oxygen as precursors in a fluidized bed reactor, as described in detail elsewhere.[10] The silica particles are 30-75 μm in diameter with an average pore size of 15 nm and a Brunauer-Emmett-Teller (BET) surface area of 270 m^2/g. Three cycles of Pt ALD were carried out at 300 ºC to obtain a Pt loading of 2.2 wt.%, as measured by inductively coupled plasma-atomic emission spectroscopy (ICP-AES).

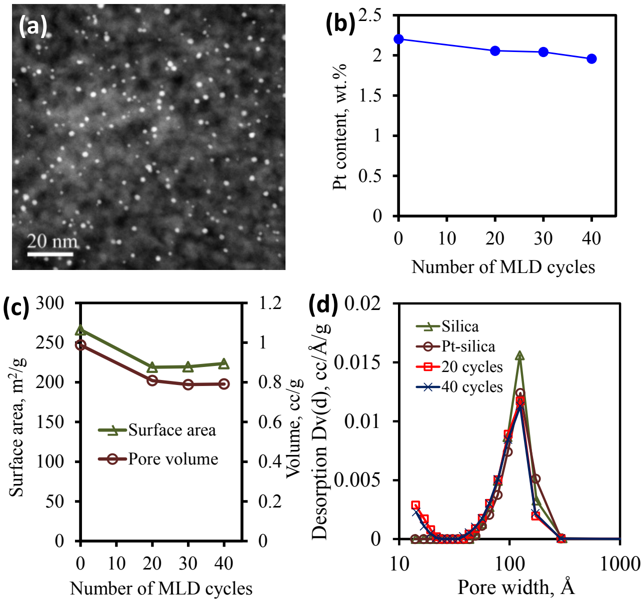

Fig. 2. (a) Cross-sectional STEM image of the Pt nanoparticles on silica gel particles, (b) Pt content, (c) surface area and pore volume, and (d) pore size distribution of the Pt/SiO_2 particles coated with different thicknesses of porous alumina films.

One cross-sectional scanning transmission electron microscopy (STEM) image of Pt/SiO_2 is displayed in Fig. 2a. The white points in the picture are Pt nanoparticles. The Pt nanoparticles are uniformly dispersed on the surface of silica gel particles and inside of the porous structures. The average Pt particle size is about 2 nm. The Pt/SiO_2 particles were coated with three thicknesses of alucone MLD films, deposited with 20, 30, and 40 cycles of alternating reactions of TMA and EG in a fluidized bed reactor at 160 ºC.[11] Three corresponding thicknesses (~2, 3, and 4 nm) of porous alumina films were then formed by oxidation at 400 ºC in air, as described elsewhere.[8] During the oxidation process, the samples were heated in air from room temperature to 400 °C at a rate of 1 °C/min, kept at 400 °C for one hour, and then cooled to room temperature at the same rate. The organic component was removed completely and highly porous alumina films were formed. The carbon chain length of the polymer component determines pore size, so MLD precursors with different carbon chain lengths could lead to porous metal oxide films with different pore sizes. The mass fraction of Pt in the catalyst decreased slightly as the number of MLD cycles increased, as shown in Fig. 2b, because the alumina film increased the catalyst weight.

A Quantachrome Autosorb-1 was used to obtain nitrogen adsorption and desorption isotherms of catalyst particles at -196 ºC. The specific surface areas of the samples were calculated using the BET method in the relative pressure range of 0.05–0.25. The total pore volumes were calculated from the adsorption quantity at a relative pressure of $P/P_0 = 0.99$. The pore size distribution curves were derived from the adsorption branches of the isotherms using the Barrett–Joyner–Halenda (BJH) method. As shown in Fig. 2c, the surface area of the Pt/SiO_2 particles decreased from 266 to 219 m^2/g with 20 cycles of MLD coating, and slightly increased with the further deposition of MLD films. This increase is due to the contribution of the higher surface area porous alumina films, which can have a surface area as high as 1000 m^2/g.[8] The pore volume of the Pt/SiO_2 particles decreased from 0.99 to 0.81 cm^3/g with 20 cycles of MLD coating, and slightly decreased again to 0.79 cm^3/g with the further deposition of MLD films. As shown in Fig. 2d, the average pore size of the silica gel particles was about 15 nm. The number of mesopores decreased with the deposition of Pt nanoparticles, but there was no further decrease with the deposition of porous alumina films. Clearly, a large number of micropores were formed after MLD coating, compared to silica gel or Pt/SiO_2 particles. The average pore size of the porous film was estimated to be 0.6 nm.[8]

The catalytic hydrogenation of olefins (n-hexene >99%, and cis-cyclooctene >95%) was carried out in an ethyl acetate solution under a static hydrogen atmosphere at 35 ºC.

The reactions were conducted in unstirred mini-batch reactors assembled from 3/8 inch stainless steel Swagelok® parts. Port connectors sealed with a cap on one end and one three-way valve on the other end gave a reactor volume of about 2 mL. In a typical run, n-hexene or cis-cyclooctene (0.08 g), ethyl acetate (0.78 g) and the Pt catalysts (~0.006 g) were added to the reactor. All catalysts had an identical Pt loading even though the total mass within the reactor increases as the number of MLD cycles increases. The mass ratio of Pt to olefin was 0.15%. The residual air in the reactor was expelled by flushing with hydrogen. The reactor was first pressurized with hydrogen to 20 psi and depressurized to atmosphere pressure. This process was repeated 50 times. After this flushing process, more than 99.999% of air was replaced by hydrogen gas. The control experiments indicated that the mass loss of the reactants and the solvent during this flushing process was less than 0.5 wt.%. The reaction was carried out at 1 atm of hydrogen and 35 ºC for 24 hours. The amount of hydrogen in the closed system was more than enough for the hydrogenation reaction. After the reaction, the catalyst powder was filtered off and the filtrate was analysed using a gas chromatograph (Agilent, 6890N) equipped with a 30 m DB-5 column and FID detector to determine the conversion and selectivity.

The control experiments indicated that there was no catalytic activity of olefin hydrogenation for both silica gel particles and alumina ALD films. The catalytic activity resulted solely from Pt. The results are listed in Fig. 3. For the uncoated Pt/SiO_2 catalyst, the conversion of n-hexene and cis-cyclooctene was 9.1% and 6.9%, respectively. The conversion of n-hexene decreased with ~2 nm of porous alumina film (20 cycles of MLD), and decreased slightly more with further increases in film thickness. The conversion of n-hexene fell to 4.5% after the catalyst was coated with ~4 nm of alumina film.

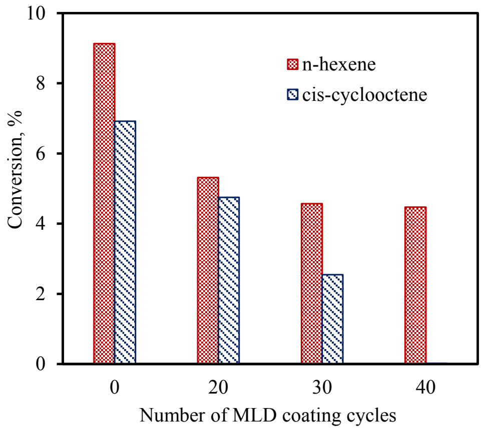

Fig. 3. Size-selective hydrogenation of n-hexene and cis-cyclooctene catalyzed by Pt/SiO_2 particles coated with different thicknesses of porous alumina films.

In contrast, the conversion of cis-cyclooctene decreased almost linearly as the thickness of the porous alumina films increased, and no obvious cis-cyclooctene conversion (<0.02 %) was observed with ~4 nm of alumina films. Clearly, the naked Pt nanoparticles displayed indiscriminate catalysis of olefin hydrogenation. In contrast, the Pt nanoparticles encapsulated with a porous alumina shell showed selectivity for catalytic hydrogenation of n-hexene versus cis-cyclooctene due to the size discrimination of the ultra-thin porous layer.

Previous studies of H_2 chemisorption indicated that the Pt dispersion decreased when the Pt nanoparticles were encapsulated with porous alumina films due to the contact points between Pt particles and the porous metal oxide films.[12] About 42% of the Pt surface area was lost with the deposition of 40 cycles of MLD films.[12] In this study, the reduction of the conversion of n-hexene was 51% with the deposition of 40 cycles of MLD films on Pt/SiO_2, compared to the naked Pt/SiO_2. It is believed that the decline in the conversion of n-hexene was mainly caused by the loss of Pt metal surface, rather than the mass diffusion limitation resulting from the thin porous oxide films. The porous structure allows smaller reactants to access the encapsulated active sites, and inhibits or prevents the reactants with larger molecular size from accessing the Pt sites. Since the film is ultra-thin, the reactants and products of small molecules can pass freely through the porous films. The molecular size of H_2 is so small, that the size effects for H_2 molecules can be neglected. The size-selectivity effect results mainly from the difference in the molecular size of olefins.

In summary, a novel strategy to prepare a supported size-selective metal nanoparticle catalyst with an ultra-thin porous shell was developed. The thickness of the porous oxide films could be well controlled at subnanometer scale by applying the MLD technique. The pore size of the film was about 0.6 nm. The size selective effect of the porous alumina films was verified by the liquid-phase hydrogenation of n-hexene versus cis-cyclooctene. This catalyst showed great selectivity in the hydrogenation of olefins. Importantly, the mass diffusion limitation was not significant due to the ultra-thin films. The success of making these materials by MLD opens up a new method for preparing size-selective catalysts.

Acknowledgements

This work was partly supported by the University of Missouri Research Board. The authors thank Dr. Xinsheng Zhang at Environmental Research Centre at Missouri University of Science and Technology for the assistance with the GC analysis.

Notes and References

1. P. Collier, S. Golunski, C. Malde, J. Breen and R. Burch, *Journal of the American Chemical Society,* 2003, **125**, 12414.

2. (a) N. Nishiyama, K. Ichioka, D. H. Park, Y. Egashira, K. Ueyama, L. Gora, W. D. Zhu, F. Kapteijn and J. A. Moulijn, *Industrial & Engineering Chemistry Research,* 2004, **43**, 1211; (b) H. Q. Yang, Y. Z. Chong, X. K. Li, H. Ge, W. B. Fan and J. G. Wang, *Journal of Materials Chemistry,* 2012, **22**, 9069.

3. G. Lu, S. Z. Li, Z. Guo, O. K. Farha, B. G. Hauser, X. Y. Qi, Y. Wang, X. Wang, S. Y. Han, X. G. Liu, J. S. DuChene, H. Zhang, Q. C. Zhang, X. D. Chen, J. Ma, S. C. J. Loo, W. D. Wei, Y. H. Yang, J. T. Hupp and F. W. Huo, *Nature Chemistry,* 2012, **4**, 310.

4. Z. P. Lai, G. Bonilla, I. Diaz, J. G. Nery, K. Sujaoti, M. A. Amat, E. Kokkoli, O. Terasaki, R. W. Thompson and M. Tsapatsis, *Science,* 2003, **300**, 456.

5. D. Zhao, P. Yang, N. Melosh, J. Feng, B. F. Chmelka and G. D. Stucky, *Advanced Materials,* 1998, **10**, 1380.

6. J. L. Lu, B. S. Fu, M. C. Kung, G. M. Xiao, J. W. Elam, H. H. Kung and P. C. Stair, *Science,* 2012, **335**, 1205.

7. C. P. Canlas, J. L. Lu, N. A. Ray, N. A. Grosso-Giordano, S. Lee, J. W. Elam, R. E. Winans, R. P. Van Duyne, P. C. Stair and J. M. Notestein, *Nature Chemistry,* 2012, **4**, 1030.

8. X. H. Liang, M. Yu, J. H. Li, Y. B. Jiang and A. W. Weimer, *Chemical Communications,* 2009, **46**, 7140.

9. (a) T. Yoshimura, S. Tatsuura and W. Sotoyama, *Applied physics letters,* 1991, **59**, 482; (b) A. A. Dameron, D. Seghete, B. B. Burton, S. D. Davidson, A. S. Cavanagh, J. A. Bertrand and S. M. George, *Chemistry of Materials,* 2008, **20**, 3315.

10. X. H. Liang, Y. Zhou, J. H. Li and A. W. Weimer, *Journal of Nanoparticle Research,* 2011, **13**, 3781.

11. X. H. Liang, D. M. King, P. Li, S. M. George and A. W. Weimer, *AIChE Journal,* 2009, **55**, 1030.

12. X. H. Liang, J. H. Li, M. Yu, C. N. McMurray, J. L. Falconer and A. W. Weimer, *ACS Catalysis,* 2011, **1**, 1162.

III. Significant Capacity and Cycle-Life Improvement of Lithium-Ion Batteries through Ultrathin Conductive Film Stabilized Cathode Particles

Rajankumar L. Patel, Hui Xie, Jonghyun Park, Hooman Yaghoobnejad Asl, Amitava Choudhury, and Xinhua Liang*

R.L. Patel, Prof. X.H. Liang
Department of Chemical and Biochemical Engineering, Missouri University of Science and Technology, Rolla, MO 65409, United States
Email: liangxin@mst.edu

H. Xie
Texas Materials Institute, The University of Texas at Austin, Austin, Texas 78712, United States

Prof. J. Park
Department of Mechanical and Aerospace Engineering, Missouri University of Science and Technology, Rolla, MO 65409, United States

H. Yaghoobnejad Asl, Prof. A. Choudhury
Department of Chemistry, Missouri University of Science and Technology, Rolla, MO 65409, United States

Abstract

Atomic layer deposition (ALD), as a thin film deposition technique, has been explored as a viable path to improve the performance of lithium-ion batteries. However, a trade-off between the species transport (capacity) and protection (lifetime), resulting from the insulating properties of ALD films, is the key challenge in ALD technology. Here we report a breakthrough to overcome this trade-off by coating an ultra-thin conformal cerium dioxide (CeO_2) film on the surfaces of $LiMn_2O_4$ particles. The optimized CeO_2 film (~3 nm) coated particles exhibit a significant improvement in capacity and cycling performance compared to uncoated, Al_2O_3 coated, and ZrO_2 coated samples at room temperature and

55 °C for long cycling numbers. The initial capacity of the 3 nm CeO_2 coated sample shows 24% increment compared to the capacity of the uncoated one, and 96% and 95% of the initial capacity is retained after 1,000 cycles with 1 C rate at room temperature and 55 °C, respectively. The detailed electrochemical data reveal that the suppression of the impedance rise and the facile transport of the species are the main contributors to the success.

Keywords: Atomic layer deposition (ALD), cerium dioxide (CeO_2), lithium-ion battery, cathode, conductive

1. Introduction

Thin film coatings on lithium-ion battery (LIB) electrode powders have proven to be an effective way to improve the capacity retention, rate capability, and thermal stability of electrode materials. Different coating materials have been studied, including carbon,[1] metal oxides (e.g., Al_2O_3, ZrO_2, ZnO, and SiO_2)[2-4] and metal phosphates (e.g., $AlPO_4$).[5] The majority of the coating strategies were based on the sol–gel methods,[2-4] which require a heat treatment after the coating process. These coating technologies can cause an unstable interface and poor longevity of the performance due to possible incomplete coating or an overly thick coating.[6] In contrast, an ultra-thin film coating with a thickness at sub-nanometer levels has the potential to alleviate the requirements of the electron and Li^+ conductivity for coating materials. Atomic layer deposition (ALD) has been demonstrated to be an important technique for high performance materials for batteries.[7] ALD is best known for its ability to deposit high-quality ultra-thin films of materials based on alternating pulses of chemical vapors that react with surfaces.[8, 9] Atmospheric pressure ALD process for particle coating has also been reported.[10] Unlike physical coating methods, strong chemical bonds are created to maintain the physical integrity between the substrate and the coating layer. To date, studies mainly focus on insulating ceramic ALD thin film coatings, such as Al_2O_3,[7, 11, 12] TiO_2,[13] ZnO,[7, 14] and ZrO_2.[14]

However, for instance, Al_2O_3 is not the most ideal material for LIB applications because of its poor electronic and ionic conductivity. Ideally, the film must be thick enough to protect the active materials long enough from the superfluous electrochemical side reactions.[11] The increased thickness, however, hinders the species transport including electrons and ions. There is a trade-off between the species transport (increasing capacity) and protection of the particles (expecting long cycle life). Jung et al.[7] demonstrated that $LiCoO_2$ powders, coated with thicknesses of only 0.3 to 0.4 nm using two Al_2O_3 ALD cycles, exhibited a capacity retention of 89% after 120 charge-discharge cycles in the 3.3–4.5 V (vs. Li/Li^+) range, while the bare $LiCoO_2$ powders displayed only a 45% capacity retention. However, the results from this study were limited to low cycle numbers (120 cycles). They also demonstrated a thicker ALD film showed a significantly decreased capacity (~ 20 $mAhg^{-1}$), and attributed it to the reduction in electron conductivity and possible reduction in Li-ion conductivity. High kinetic and diffusion polarizations might result in the capacity decrease. They also observed large overpotentials with the thick films. Similar results have been reported,[15-17] but they only demonstrated a partial improvement within limited cycle numbers; they could not retain the improved capacity after long cycles or under the severe loading conditions such as high C rates and high temperatures. These unsatisfactory outcomes call for a reliable coating methodology which can achieve both high capacity and excellent cycling capability simultaneously. It is highly desirable to develop a robust coating with a superior ionic conductivity facilitating facile (de)intercalation of the lithium ions in the active materials. The main challenge is how to resolve that confrontation between the facile transport with a thin layer and long protection with a thick layer.

Herein, we demonstrated that coating with an ultra-thin electronic and ionic conductive film can solve this trade-off problem. $LiMn_2O_4$ was studied as a proof of the concept, since it is one of the important cathode materials in LIBs due to its high working voltage, low toxicity, and low cost. However, it suffers from two major shortcomings: (1) fast capacity fading, induced by poor electrochemical stability, especially under high charge voltage and high temperature; and (2) poor electrical conductivity (10^{-6} s/cm vs. 10^{-2} s/cm for $LiCoO_2$[18]) as well as slow Li^+ diffusion within the cathode materials (10^{-11}~10^{-13} cm^2/s for a pure $LiMn_2O_4$ cathode and 10^{-8} ~10^{-9} cm^2/s for a blended cathode with carbon black and a binder).[19]

We utilized cerium oxides (CeO_2) as the thin film coating materials. CeO_2 offers varied interesting properties including oxygen storage capacity, high thermal stability, electrical conductivity, and diffusivity. CeO_2 is already being used as promoter in many catalyst formulations and enhance the electrical contact between oxides facilitating electron transfer between CeO_2 and the supported metal oxide. CeO_2 films have been used in LIB research via nanocomposite and particle coating[20] (based on sol-gel method), but the performance improvement was limited to relatively short cycling number (<100 cycles). Previous studies[21-23] of nano-CeO_2 coated $LiMn_2O_4$ using pechini method or precipitation method indicated that no significant enhancement of cycling stability of $LiMn_2O_4$ was achieved using CeO_2 coating. The main reason could be the fact that the CeO_2 films prepared by these methods were composed of CeO_2 nanoparticles. These films were not conformal and pin-hole free as well as being too thick.

In this study, large quantities of $LiMn_2O_4$ particles were coated with ultra-thin CeO_2 films by ALD in a fluidized bed reactor. For comparison, five cycles of Al_2O_3 and five cycles of ZrO_2 ALD films, which are among the optimal ALD film thicknesses based on previous reports,[7, 14] were also deposited on the surfaces of $LiMn_2O_4$ particles. The high stability and high initial capacity of the CeO_2 coated samples were demonstrated by the long cycle life performance of the prepared cells for more than 1,000 charge-discharge cycles at room temperature and high temperature.

2. Results and Discussion

2.1. CeO_2 Films Coated on $LiMn_2O_4$ Particles

CeO_2 films were conformally coated on the surfaces of $LiMn_2O_4$ particles (~8 µm, L-140 from LICO Technology Corporation). The TEM image of an uncoated $LiMn_2O_4$ particle (shown in **Figure 1**a) displays a clean edge of a pristine particle. In contrast, Figure 1b displays a distinctive conformal coating of ~3 nm layer on a $LiMn_2O_4$ particle after 50 cycles of CeO_2 ALD. The thickness of CeO_2 film was ~5 nm after 100 cycles of CeO_2 ALD (Figures 1c and 1d). The conformality of the CeO_2 films on parimary $LiMn_2O_4$ particles can be verified from **Figure S1.** For the film thickness comparison, the TEM images of $LiMn_2O_4$ particles coated with 5 cycles ZrO_2 ALD and 5 cycles Al_2O_3 ALD are also provided in Figure S1.

2.2. Electrochemical Testing

Galvanostatic charge-discharge measurements were carried out in a voltage range between 3.4 V and 4.5 V. **Figures 2**a and 2b show the discharge capacities of uncoated (UC), 5 cycles of ZrO_2 (5Zr), 5 cycles of Al_2O_3 (5Al), and 10 (10Ce), 30 (30Ce), 50 (50Ce), 100 (100Ce), and 150 (150Ce) cycles of CeO_2-coated $LiMn_2O_4$ samples that were discharged with different C rates at room temperature and 55 ºC, respectively. For each cell, the discharge capacities were measured for five cycles at discharge rates of 0.2C, 0.5C, 1C, and 2C. Compared to the UC, 5Al, and 5Zr, the CeO_2 coated samples showed higher initial discharge capacity at various C rates, except for the samples coated with 100Ce and 150Ce.

The voltage drop in a LIB is mainly resulted from the kinetic overpotential, diffusional overpotential, resistance due to the Solid Electrolyte Interphase (SEI) layer, and ohmic resistance. The ALD CeO_2 film can affect all of the voltage drops except for the diffusional overpotential if the lithium concentration ratio between the surface and inside bulk is not changed significantly due to the CeO_2 coating. For the SEI layer, compared to the SEI layer formed on anode particles, the thickness of the surface film (sometimes it is called solid permeable interface, SPI layer[24]) formed on the cathode particles is thin and it increases with time and temperature. This process consumes the active lithium ions and solvents. It also causes gas evolution which builds up pressure inside the cell causing significant capacity fade. Generally, the SPI layer on cathode particles cannot effectively passivate the surface, so the SPI layer thickness keeps increasing. However, the ALD CeO_2 layer can serve as an artificial SEI layer, so it can suppress further formation of the SEI layer. The thickness of 3 nm CeO_2 is quite thick compared to the initial thin SPI layer, so it can prevent the layer from growing further.

As the most of literature on ALD coating strategies on the particles in battery electrode materials have demonstrated, putting a fence around particles delays the transport of lithium ions. This may increase the charge transfer resistance. However, a CeO_2 film, which has a relatively high ionic conductivity, allows the ions to move easily.[25, 26] Additionally, since the particles are totally covered with CeO_2 film, the film plays a role as the electronic path. Consequently, the CeO_2 coating interface stabilized the chemical reaction and species transport inside the cell, which, otherwise, would have led to a large polarization and then caused capacity fading, as was evident for uncoated $LiMn_2O_4$. **Figure 3** apparently demonstrates the difference between the UC particles (a) and the 50Ce particles (b) in terms of voltage drop. As the cycle number increases the voltage drop increases significantly (first 250 cycles are most severe), while no significant voltage drop change is observed for the CeO_2 coated particles during long cycling.

Figures 4a shows the results of discharge cycling at a 1C rate between 3.4 V and 4.5 V for the UC, 5Zr, 5Al, and 30Ce, 50Ce, and 100Ce cells at room temperature up to 1,000 cycles. The discharge capacity of the UC was initially 61 mAh/g, but then after 1,000 cycles it declined to 24 mAh/g. For the 5Al and 5Zr samples, the initial discharge capacity was 54 mAh/g and 61 mAh/g, respectively. With five cycles of Al_2O_3 ALD coating, an obvious initial discharge capacity reduction was observed, which was consistent with the previously reported data.[7, 11] In contrast, the 30Ce and 50Ce samples exhibited much higher initial discharge capacities than the UC. Notably, the 50Ce showed a remarkable initial discharge capacity of 80 mAh/g, which is a 24 % increment compared to the UC.

The stable discharge capacity at 81 mAh/g was maintained even after 900 cycles and only dropped slightly to 78 mAh/g after 1,000 cycles. This was still 17 mAh/g higher than the initial discharge capacity of the UC cell. In addition, as seen in Figure 4b, surface modification via ALD significantly improved the cycling performance of $LiMn_2O_4$, even at an elevated temperature. The 50Ce cell exhibited an initial discharge capacity of 81 mAh/g and was stable even after 800 cycles, remarkably with no apparent loss of capacity. CeO_2 coating using Pechini method was reported for the stabilization of $LiMn_2O_4$ spinel.[21] Their reported capacity dropped to 82 % within 150 cycles between 3.0 V and 4.4 V at room temperature for $LiMn_2O_4$ coated with 2 wt.% CeO_2; at elevated temperature their capacity dropped even faster to 82% after 40 cycles. Clearly, the CeO_2 ALD coated samples have much better performance than the reported samples coated with non-ALD techniques. In this study, the 50Ce cell had a much higher capacity than the 5Zr, 5Al and UC cells, which meant that CeO_2 was much more chemically and thermally stable with good conductivity.

As confirmed from the previous work, the downside of coating on particles is to delay the transport of the species. Also, as the C rate increases, the temperature inside cell increase, and the stress level is also increased due to developed concentration gradient inside particles and possible phase transition at the surface of the particle resulting from overlithiation. **Figure 5** shows the results of the test at 2C rate. The 50Ce still had far better discharge capacity than the 5Zr, 5Al, and UC cells, even after 1,000 cycles at 2C rate. The 50Ce showed more than 62% capacity retention after 1,000 cycles, while the UC and 5Zr did not show steady capacity retention and their capacities kept dropping very quickly untill they reached zero. The excellent cycling behavior of the CeO_2-coated $LiMn_2O_4$ electrodes, compared to the uncoated particles or coated particles with other materials, clearly indicated that the CeO_2 coating has enough conductivity, so it can achieve significantly improved electrochemical performances even at high C rates.

In order to characterize the electrochemical property changes due to the interface change caused by the ALD film coating, an Electrochemical Impedance Spectroscopy (EIS) analysis was conducted. As shown in **Figure 6**, one major semicircle was observed for both uncoated and CeO_2 coated samples. This is due to an overlap between the SEI layer contribution at high frequency and the charge transfer resistance at mid-high frequency. The inclined lines at low frequencies represent the bulk diffusion of lithium ions. In Figure 6a and 6b, it is clear that the 10Ce, 30Ce, and 50Ce samples show distinctively smaller diameter of the semicircles compared to the UC. A slight expansion of semicircle was observed with the increase in the thickness of the deposited CeO_2 films. This represents the increase of charge transfer resistance due to the delay of the lithium transfer through a longer distance as the film thickness increases. As a result, the 100Ce sample shows the largest resistance even compared to the UC spinel.

EIS spectra were fitted using a corresponding equivalent circuit given in Figure 6c. To clarify, the curves represent only the marker connector lines and do not represent the fit line. In the equivalent circuit, R_{ohm} refers to the uncompensated ohmic resistance between the working electrode and the reference electrode, R_{f} represents the resistance for lithium ion mobility in the surface layer (including SEI layer and/or surface modification layer), CPE refers to the constant phase-angle element depicting the non-ideal capacitance of the surface layer and double layer, R_{ct} refers to the charge transfer resistance, R_{w} represents the Warburg impedance (which is inversely proportional to lithium ion diffusion coefficient) describing the lithium ion diffusion in the bulk material. Among these parameters, R_{ohm}, R_{ct}, and R_{f} can be used to quantify the polarization behaviors, that is, ohmic polarization, charge transfer polarization, and resistance due to surface layer, respectively. These resistance values are provided in **Table 1** and the other EIS spectra parameters obtained from the fitted curves are provided in **Table S1**. The R_{ohm} remains almost constant for all, uncoated and coated, electrodes alike. In the impedance analysis of all the cells, only one semicircle was observed and therefore the spectra are fitted using a combination of surface-film and charge-transfer resistance, $R_{(f+ct)}$. The impedance parameters for the UC and 50Ce cells clearly show that the former electrodes develop slow kinetics upon cycling. For the fresh cells, the difference in $R_{(f+ct)}$ values between the uncoated and coated samples, is narrow, but when the cells were charged and discharged for 1,000 cycles, the difference between the $R_{(f+ct)}$ values of the UC and 50Ce samples become almost double (176.0 and 95.5 Ω, respectively), which clearly demonstrates that the kinetics of the surface films developed on the cathode material during cycling.[21] Furthermore, the total $R_{(f+ct)}$ values of the 5Zr and 5Al cells (128.7 and 154.2 Ω, respectively) were much higher than that of the 50Ce cell (95.5 Ω). The resulting trend for 5Zr and 5Al are supported by literature.[15, 27] So, the lowest surface-film and charge-transfer resistance values confirm that the 50Ce cells have higher conductivity than the UC, 5Al, and 5Zr samples. Ha et al. also reported the similar trend for their uncoated and CeO_2 coated (using pechini method) $LiMn_2O_4$.[21] The $LiMn_2O_4$ modified with an adequate CeO_2 content, as in the case of 10Ce, 30Ce, and 50Ce, resulting in a thin ALD coating layer of amorphous CeO_2, decreases the $R_{(f+ct)}$. The $R_{(f+ct)}$ of 50Ce was much less than the pristine both before and after the cycling. The resistance of the other samples increased significantly after the 1,000 cycles probably due to the formation of a SEI layer.[28] It is identified that the 50Ce has faster charge-transfer kinetics and is less influenced by cycling, compared to the UC. However, thicker ALD coating of CeO_2, as evident from the 100Ce conductivity data (described later), has a higher resistance than the other coated samples. This clearly proves that only certain thickness of the CeO_2 ALD coating is beneficial for the improved cycling performance of a LIB.

In order to further investigate the electrochemical property change as a function of cycling number, EIS measurements of the UC and 50Ce cells were recorded at 3.8 V for 0, 50, 100, 200, 500, and 1000 charge/discharge cycles. The impedance spectra recorded after certain number of charge/discharge cycles for the UC and 50Ce cells are shown in **Figures 7**a and **7**b, respectively. As the number of charge/discharge cycles increased, the semicircle of the UC cell increased distinctively. For the UC cell, the increased resistance as a function of cycle number was associated to changes occurring as a result of the unstable interfacial surface layer due to SEI layer formation, dissolution, and mechanical fracture.[29, 30] This degradation inhibited the charge transfer at the material surface, causing increase in the radius of the semi-circle. After 1,000 charge-discharge cycles, the Nyquist plot of the UC shows a partial second semicircle which indicates a separation of the higher resistance due to severe formation of the SEI layer.[31] In other words, R|C has the unit of time and is called "relaxation time", which itself has an inverse relationship with the critical frequency at which the process occurs. With increase in the number of charge/discharge cycles, the SEI resistance increases (in Figure 7a for the UC after 1,000 cycles) which leads to an increase in the time constant and consequently the merged R|C elements become separated as the critical frequency of the processes varies. In the case of the 50Ce cells, very less impedance change was recorded even after 1,000 cycles, as shown in Figure 7b. The 50Ce sample exhibited the resilience to any increased resistance caused by charge-discharge cycling of the system. The consistency of the 50 Ce sample indicates that the SEI formation was at minimal which was reflected in the longevity of the system during charge-discharge cycling.

For conductivity comparison, pellets of the UC, 5Al, 5Zr, 30Ce, 50Ce, and 100Ce materials were prepared. Each pellet contained only cathode material. It is important to note here that this conductivity measurement method using ac complex plane impedance analysis was employed for the measurement of mixed ionic conductivity and electronic conductivity.[32-34] The impedance curves were fitted using the equivalent circuit shown in Figure 8. The bulk ac conductivity of uncoated $LiMn_2O_4$ particles was calculated to be ~10^{-6} Scm^{-1}, which is slightly lower than reported values.[35-37] This was caused by the fact that the pellets were not sintered or hot-pressed at high temperature, and there was ~11% porosity between particles (calculated pellet density was 3.81 g/cm^3), which increased resistivity and resulted in a lower conductivity. However, comparing the results among the coated and uncoated samples, which were prepared with the same procedure and material composition, from **Figure 8**, it is certain to conclude that the 30Ce and 50Ce cells show much higher conductivity than the UC. The 50Ce sample is about two orders of magnitudes higher than the UC sample. This shows the direct effect of the CeO_2 coating on the $LiMn_2O_4$. The results of 5Zr and 5Al are slightly better than the UC, but not as significant as the CeO_2 coated samples. The 100Ce showed poor conductivity because the thicker coating could increase the imperfection, such as vacancies, dislocation, and grain boundary lengths, so the frictional forces impeding the movement of the species, and leading to high resistance.[26, 38] The equivalent circuit used to fit the EIS spectra is shown in inset of Figure 8. The parameters obtained from fitting those curves are provided in **Table S2**. The conductivity has been found to obey the Arrhenius equation,[39, 40]

$$\sigma \cdot T = \sigma_0 \cdot exp\left(\frac{-E_a}{k_B T}\right)$$

where, σ_0 is pre-exponential factor, k_B is the Boltzmann constant, T is the absolute temperature, and E_a is the activation energy for the migration of lithium ions. The linear relation in the Arrhenius plots, shown in **Figure 9**, of conductivity prolonged to ~330 K assures that neither the Li-deficit nor any structural change occurs during measurements. The activation energy of the UC sample is ~0.4 eV, which is similar to the reported values.[41, 42] In contrast, the 50Ce has a lower activation energy of ~0.3 eV, which further solidifies the better conductivity and the corresponding improved cycling results.

Changes in CeO_2 film thickness were sensitive towards the stable performance and life of the battery systems. The specific discharge capacity of the 100Ce cells was 57 mAh/g for the first few cycles and finally decreased to ~28 mAh/g after 1,000 cycles tested at room temperature. This behavior can be attributed to the fact that the CeO_2 ALD film of 100 cycles was too thick. Also, the appearance of the second semicircle in the impedance spectra of 100Ce, as shown in Figure 6, is another indication of the adverse effect of the thicker coating. The delayed transport process at the interface will increase the effective charge transfer resistance. The increased R_f with the increased CeO_2 film thickness is the evidence of disturbance of blocking layer.

Dissolution of manganese ions into the electrolyte was the major issue for the poor electrochemical performances of the $LiMn_2O_4$ materials at elevated temperatures. The successive electrolyte degradation and Mn^{3+} dissolution into the electrolyte could have been involved the uncoated $LiMn_2O_4$ cathode's capacity loss.[15, 43] The most effective way to block Mn^{3+} dissolution is to completely encapsulate the spinel particles with oxides that are resistant to acidic HF, but are conductive for electron and Li^+. The CeO_2 coated cells showed far more superior stability and higher discharge capacity than the ZrO_2 and Al_2O_3 coated materials. Although, the alumina coated cell showed stability throughout the cycle life testing, its initial discharge capacity was lower than that of the uncoated samples. The ZrO_2 coated samples showed a slightly better discharge capacity than the Al_2O_3 coated sample. However, it was not comparable to the 30Ce and 50Ce samples.

Further, the capacity of 5Zr and 5Al decreased with an increase in the number of charge-discharge cycles. Previous studies indicated that the oxide coating on $LiMn_2O_4$ scavenged trace HF in LIBs and, thus, slowed dissolution of the manganese ions and degradation of the organic electrolyte at the cathode, resulting in a better electrochemical performance of $LiMn_2O_4$.[6, 44] This was true for a low number of charge-discharge cycles. Such a thin film is not thick enough for a large number of charge-discharge cycles, since a partial dissolution of thin film coating could occur during charge-discharge cycling,[45] and cause the capacity to fade. However, if the film is a bit thicker, the capacity will remain even after hundreds of cycles, but the initial capacity would decrease significantly. Coating a conductive layer with a certain thickness can overcome this trade-off. This study indicated that a CeO_2 film, with 50 cycles of ALD coating (3 nm thick), was optimal for enhancing the initial capacity and cycling performances of an electrode and thick enough to protect the particles without hindering transport of the lithium ions into the particles. The robust CeO_2 film coating suppresses the chemical instability leading to the resistance increase.

3. Conclusion

In summary, we have successfully demonstrated that coating an ultra-thin Li^+ conductive CeO_2 film can overcome the trade-off between Li^+ diffusion and the protection. The 50 cycles of CeO_2 coated $LiMn_2O_4$ cathode exhibited significantly higher initial capacity (24% increase compared to the uncoated one) and much better stability than the uncoated samples, and ZrO_2 and Al_2O_3 ALD coated samples. The 50 cycles of CeO_2 coated material showed an extraordinary capacity retention, both at room temperature (96% of its initial capacity) and at 55 °C (95% of its initial capacity), after 1,000 cycles of charge-discharge at the 1C rate. The detailed electrochemical data reveal that the suppression of the impedance rise and the facile transport of the species are the main contributors to the success. In depth study of mechanical/chemical stability was not the focus for this article, however, there is an on-going research, for future publications, to explore the subject area. To the best of our knowledge, this is the first reported instance of both a simultaneous initial capacity increase and excellent capacity retention at room temperature and at high temperature after 1,000 cycles of charge-discharge at the 1C rate. This strategy can also be applied to other cathode and anode materials. This significant consistency, in terms of stability and capacity retention of cerium oxide coating, can be useful for many applications that demand rechargeable batteries with longer cycle life performance. The ALD process can prepare these conductive films and, thus, provide new opportunities for the electrochemical industry to design novel nanostructured electrodes that are highly durable and highly functional at high rates.

4. Experimental Section

ALD coating: Different thicknesses of CeO_2 thin films were coated on $LiMn_2O_4$ powders by ALD in a fluidized bed reactor, described in detail elsewhere.[46] Tris(i-propylcyclopentadienyl)cerium ($Ce(iPrCp)_3$) (99.9%, Strem Chemicals) and de-ionized water were used as precursors. The reaction temperature was 250 °C. Alumina ALD was performed using alternating reactions of trimethylaluminum (TMA, 97 %, Sigma-Aldrich) and deionized water at 177 °C. ZrO_2 ALD was carried out using alternating reactions of tetrakis(dimethylamido)zirconium(IV) (electronic grade, ≥99.99%, Sigma-Aldrich) and deionized water at 250 °C. All chemicals were used as received. For a typical run, 10 g of particles were loaded into the reactor. The minimum fluidization superficial gas velocity was determined by measuring the pressure drop across the particles bed versus the superficial gas velocity of purge gas. The base pressure was ~5 Torr at a minimum fluidization velocity of 8 sccm argon flow rate. During the ALD reaction, a needle valve was used to control the flow rate of H_2O and ensure that the H_2O pressure was high enough to promote particle fluidization. The vapor of solid precursors was delivered into the reactor using a heated bubbler. The reactor was subjected to vibration using two vibro-motors to improve the quality of particle fluidization. The feed lines were kept at ~120°C to avoid excessive adsorption of precursors on the internal walls of the system that could promote chemical vapor deposition (CVD) side-reactions. The entire coating sequence process was controlled and monitored using a LabVIEW program. Ar gas flow rate was controlled by an MKS mass flow controller during the process. Before the reaction, the particles were outgassed at 150 °C with a continuous Ar flow for at least 5 hr. Each ALD coating cycle consisted of six steps: precursor A dose, Ar flush, vacuum; precursor B, Ar flush, and vacuum. The ALD films were visualized with an FEI Tecnai F20 field emission gun high resolution TEM/STEM equipped with an energy dispersive X-ray spectrometer system for the elemental analysis of samples while imaging.

Coin cell preparation: For preparing the cathodes, a mixture of 10 wt.% polyvinylidene fluoride (PVDF) in N-methyl-2-pyrrolidone (NMP) was prepared and added to 80 wt.% $LiMn_2O_4$ and 10 wt.% carbon black. The slurry was spread on an aluminum foil rested on a glass plate using a razor blade. Air-dried coated foil was then put in a vacuum at 120 °C for 8 hr. The coated foil was punched into discs of 8-13 mm diameter. Two-electrode CR2032 coin cells were assembled to investigate the electrochemical behaviors of $LiMn_2O_4$ cathodes used as a working electrode. Lithium foils (Sigma-Aldrich, 99.9%) served as both the counter and reference electrodes. The two electrodes were separated by a porous Celgard-2320 separator composed of a 20 μm thick polypropylene (PP)/polyethylene/PP trilayer film. The commercial electrolyte from MTI Corporation was composed of lithium hexafluorophosphate ($LiPF_6$, 1 mol/L) dissolved in a mixed solvent of ethylene carbonate, dimethyl carbonate, and diethyl carbonate (1:1:1 volume ratio). All CR2032 coin cells were assembled in an argon-filled glove box.

Electrochemical testing: The galvanostatic charge-discharge measurements were carried out using an 8-channel battery analyzer (Neware Corporation) in a potential range between 3.4 V and 4.5 V. The prepared cells were tested for charge-discharge capacity at different C rates, cycleability, and impedance, both at room temperature and at 55 °C. An IviumStat electrochemical interface and impedance analyzer was used for cyclic voltammetry and impedance measurements of the prepared cells. The impedance tests were performed at 5 mV and 0.01-1M Hz frequency range. For conductivity measurements, pellets of the samples (diameter = 13 mm; thickness = 1.3 mm) were cold pressed at 20 MPa. The pellets were coated on both sides with silver paste (Sigma Aldrich) to create the blocking electrodes. Copper wires were attached to opposite pellet faces using the same silver paste. Then, the pellets were dried under vacuum at 85 °C for 6 hr. The measurements were performed using the *ac* complex plane impedance method [32, 34] at frequencies ranging from 0.1 Hz to 1 MHz and at a 1 mV signal excitation using an IviumStat impedance/gain phase analyzer. The impedance spectra were analyzed using Zview software (Scribner Associates, Inc.). Since the objective was to investigate the effect of the coating on conductivity of the uncoated material, no four-point dc measurements were performed to separate the electronic conductivity to get pure ionic conductivity. The measurements were conducted for a temperature range from 20 – 55 °C in a furnace in air. The furnace and the pellets were allowed to stabilize for at least 1 hr once the temperature was reached.

Acknowledgements

This work was partly supported by the Materials Research Center at the Missouri University of Science and Technology. The authors thank Clarissa A. Wisner at the Materials Research Center for the TEM analysis, and Dr. Manashi Nath in the Chemistry Department for the assistance with impedance measurements.

References

[1] Z. H. Chen, J. R. Dahn, *Journal of the Electrochemical Society* **2002,** 149, A1184.

[2] J. Cho, Y. J. Kim, B. Park, *Chemistry of Materials* **2000,** 12, 3788.

[3] Y. K. Sun, Y. S. Lee, M. Yoshio, K. Amine, *Electrochemical and Solid State Letters* **2002,** 5, A99.

[4] Z. H. Chen, J. R. Dahn, *Electrochemical and Solid State Letters* **2003,** 6, A221.

[5] A. T. Appapillai, A. N. Mansour, J. Cho, Y. Shao-Horn, *Chemistry of Materials* **2007,** 19, 5748.

[6] Z. H. Chen, Y. Qin, K. Amine, Y. K. Sun, *Journal of Materials Chemistry* **2010,** 20, 7606.

[7] Y. S. Jung, A. S. Cavanagh, A. C. Dillon, M. D. Groner, S. M. George, S.-H. Lee, *Journal of The Electrochemical Society* **2010,** 157, A75.

[8] T. Suntola, *Thin Solid Films* **1992,** 216, 84.

[9] S. M. George, *Chemical Reviews* **2010,** 110, 111.

[10] R. Beetstra, U. Lafont, J. Nijenhuis, E. M. Kelder, J. R. van Ommen, *Chemical Vapor Deposition* **2009,** 15, 227.

[11] Y. S. Jung, A. S. Cavanagh, L. A. Riley, S. H. Kang, A. C. Dillon, M. D. Groner, S. M. George, S.-H. Lee, *Advanced Materials* **2010,** 22, 2172.

[12] D. Guan, J. A. Jeevarajan, Y. Wang, *Nanoscale* **2011,** 3, 1465.

[13] C. M. Ban, M. Xie, X. Sun, J. J. Travis, G. K. Wang, H. T. Sun, A. C. Dillon, J. Lian, S. M. George, *Nanotechnology* **2013,** 24, 424002.

[14] J. Zhao, Y. Wang, *Journal of Solid State Electrochemistry* **2013,** 17, 1049.

[15] J. S. Kim, C. S. Johnson, J. T. Vaughey, S. A. Hackney, K. A. Walz, W. A. Zeltner, M. A. Anderson, M. M. Thackeray, *Journal of The Electrochemical Society* **2004,** 151, A1755.

[16] J.-T. Lee, F.-M. Wang, C.-S. Cheng, C.-C. Li, C.-H. Lin, *Electrochimica Acta* **2010,** 55, 4002.

[17] J. Liu, X. F. Li, M. Cai, R. Y. Li, X. L. Sun, *Electrochimica Acta* **2013,** 93, 195.

[18] C. Li, H. P. Zhang, L. J. Fu, H. Liu, Y. P. Wu, E. Ram, R. Holze, H. Q. Wu, *Electrochimica Acta* **2006,** 51, 3872.

[19] J. Xie, T. Tanaka, N. Imanishi, T. Matsumura, A. Hirano, Y. Takeda, O. Yamamoto, *Journal of Power Sources* **2008,** 180, 576.

[20] C. O. Avellaneda, M. A. C. Berton, L. O. S. Bulhões, *Solar Energy Materials and Solar Cells* **2008,** 92, 240.

[21] H.-W. Ha, N. J. Yun, K. Kim, *Electrochimica Acta* **2007,** 52, 3236.

[22] M.-Y. Cho, K.-C. Roh, S.-M. Park, J.-W. Lee, *Materials Letters* **2011,** 65, 2011.

[23] D. Arumugam, G. P. Kalaignan, *Electrochimica Acta* **2010,** 55, 8709.

[24] K. Edström, T. Gustafsson, J. O. Thomas, *Electrochimica Acta* **2004,** 50, 397.

[25] Z. C. Orel, B. Orel, *Journal of Materials Science* **1995,** 30, 2284.

[26] S. Azad, O. A. Marina, C. M. Wang, L. Saraf, V. Shutthanandan, D. E. McCready, A. El-Azab, J. E. Jaffe, M. H. Engelhard, C. H. F. Peden, S. Thevuthasan, *Applied Physics Letters* **2005,** 86, 131906.

[27] W.-K. Kim, D.-W. Han, W.-H. Ryu, S.-J. Lim, H.-S. Kwon, *Electrochimica Acta* **2012,** 71, 17.

[28] J. L. Lei, L. J. Li, R. Kostecki, R. Muller, F. McLarnon, *Journal of the Electrochemical Society* **2005,** 152, A774.

[29] Y. M. Chiang, E. B. Lavik, I. Kosacki, H. L. Tuller, J. Y. Ying, *Applied Physics Letters* **1996,** 69, 185.

[30] F. Zhou, X. M. Zhao, H. Xu, C. G. Yuan, *The Journal of Physical Chemistry C* **2007,** 111, 1651.

[31] C. X. Hua, X. P. Fang, Z. W. Yang, Y. R. Gao, Z. X. Wang, L. Q. Chen, *Electrochemistry Communications* **2012,** 25, 66.

[32] N. Kamaya, K. Homma, Y. Yamakawa, M. Hirayama, R. Kanno, M. Yonemura, T. Kamiyama, Y. Kato, S. Hama, K. Kawamoto, A. Mitsui, *Nature materials* **2011,** 10, 682.

[33] H. Inaba, H. Tagawa, *Solid State Ionics* **1996,** 83, 1.

[34] L. Zhao, N. H. Perry, K. Sasaki, S. R. Bishop, *Solid State Ionics* **2014,** 263, 75.

[35] Y. J. Wei, L. Y. Yan, C. Z. Wang, X. G. Xu, F. Wu, G. Chen, *The Journal of Physical Chemistry B* **2004,** 108, 18547.

[36] H. Kanoh, Q. Feng, T. Hirotsu, K. Ooi, *Journal of The Electrochemical Society* **1996,** 143, 2610.

[37] Q.-C. Zhuang, T. Wei, L.-L. Du, Y.-L. Cui, L. Fang, S.-G. Sun, *The Journal of Physical Chemistry C* **2010,** 114, 8614.

[38] I. Kosacki, C. M. Rouleau, P. F. Becher, J. Bentley, D. H. Lowndes, *Solid State Ionics* **2005,** 176, 1319.

[39] J. B. Goodenough, *Pure and Applied Chemistry* **1995,** 67, 931.

[40] A. R. West, *Berichte der Bunsengesellschaft für physikalische Chemie* **1989,** 93, 1235.

[41] E. Iguchi, Y. Tokuda, H. Nakatsugawa, F. Munakata, *Journal of Applied Physics* **2002,** 91, 2149.

[42] Y. Yang, C. Xie, R. Ruffo, H. L. Peng, D. K. Kim, Y. Cui, *Nano letters* **2009,** 9, 4109.

[43] M.-J. Lee, S. Lee, P. Oh, Y. Kim, J. Cho, *Nano Letters* **2014,** 14, 993.

[44] X. F. Li, J. Liu, X. B. Meng, Y. J. Tang, M. N. Banis, J. L. Yang, Y. H. Hu, R. Y. Li, M. Cai, X. L. Sun, *Journal of Power Sources* **2014,** 247, 57.

[45] D. Guan, Y. Wang, *Ionics* **2013,** 19, 1.

[46] X. H. Liang, L. F. Hakim, G.-D. Zhan, J. A. McCormick, S. M. George, A. W. Weimer, J. A. Spencer, K. J. Buechler, J. Blackson, C. J. Wood, J. R. Dorgan, *Journal of the American Ceramic Society* **2007,** 90, 57.

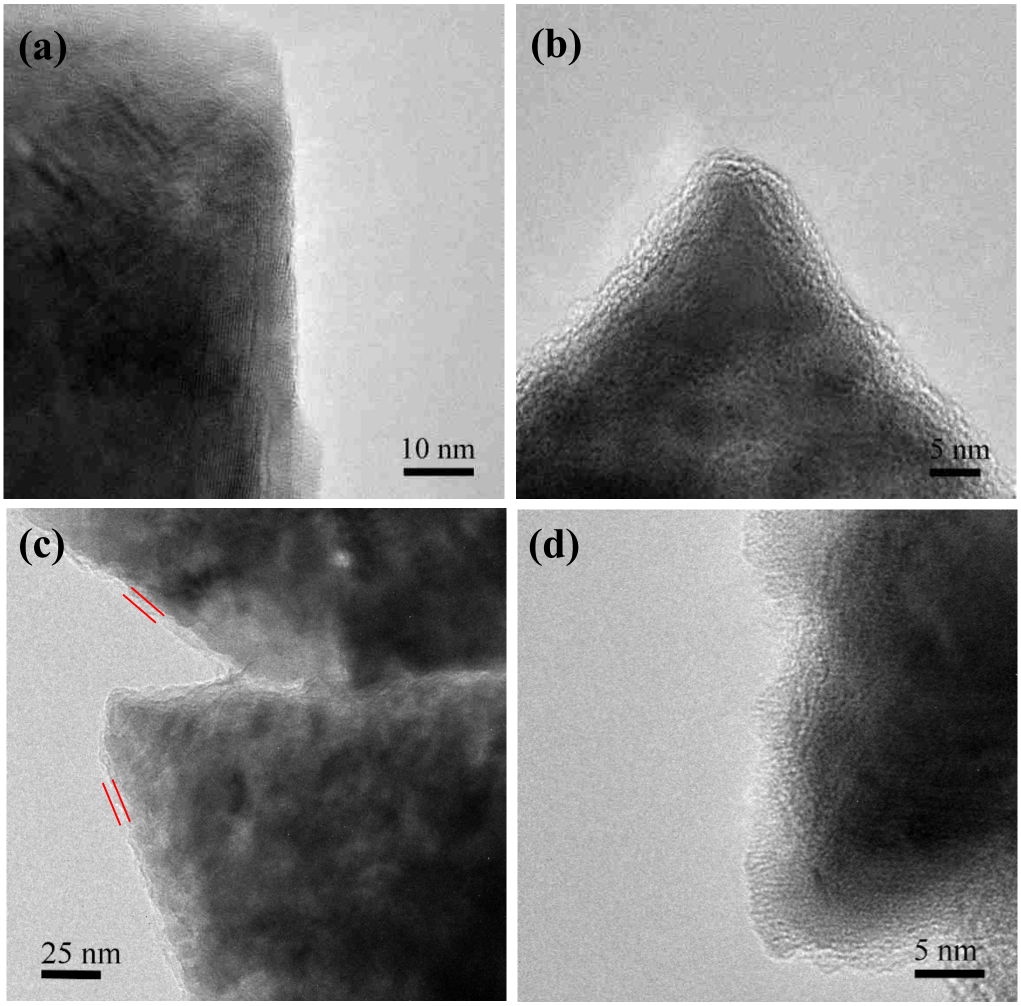

Figure 1. TEM images of (a) uncoated, (b) 50 cycles, and (c, d) 100 cycles of CeO_2 ALD coated $LiMn_2O_4$ particles.

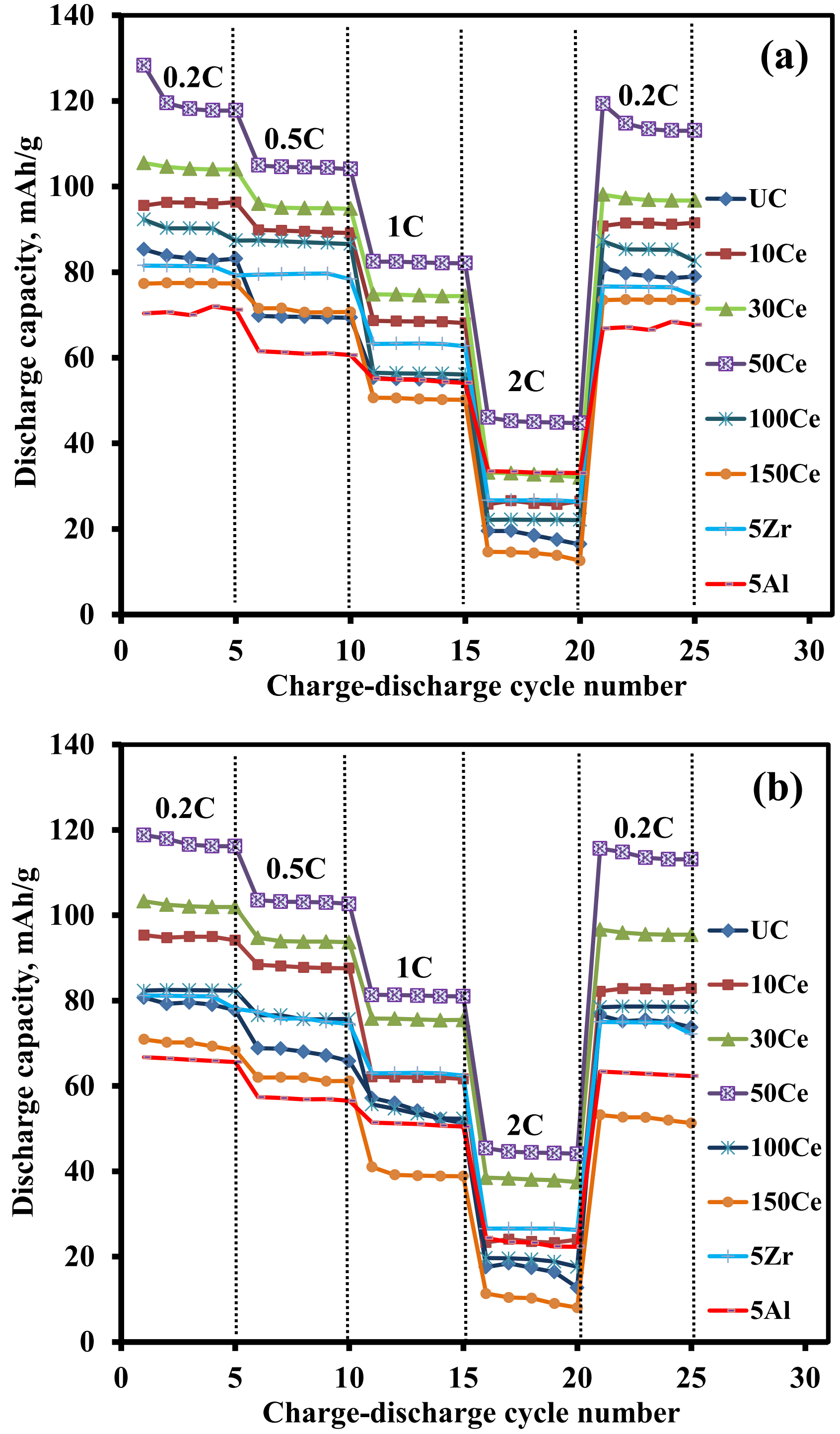

Figure 2. Galvanostatic discharge capacity at different C rates in a voltage range between 3.4 V and 4.5 V (a) at room temperature and (b) at 55 °C.

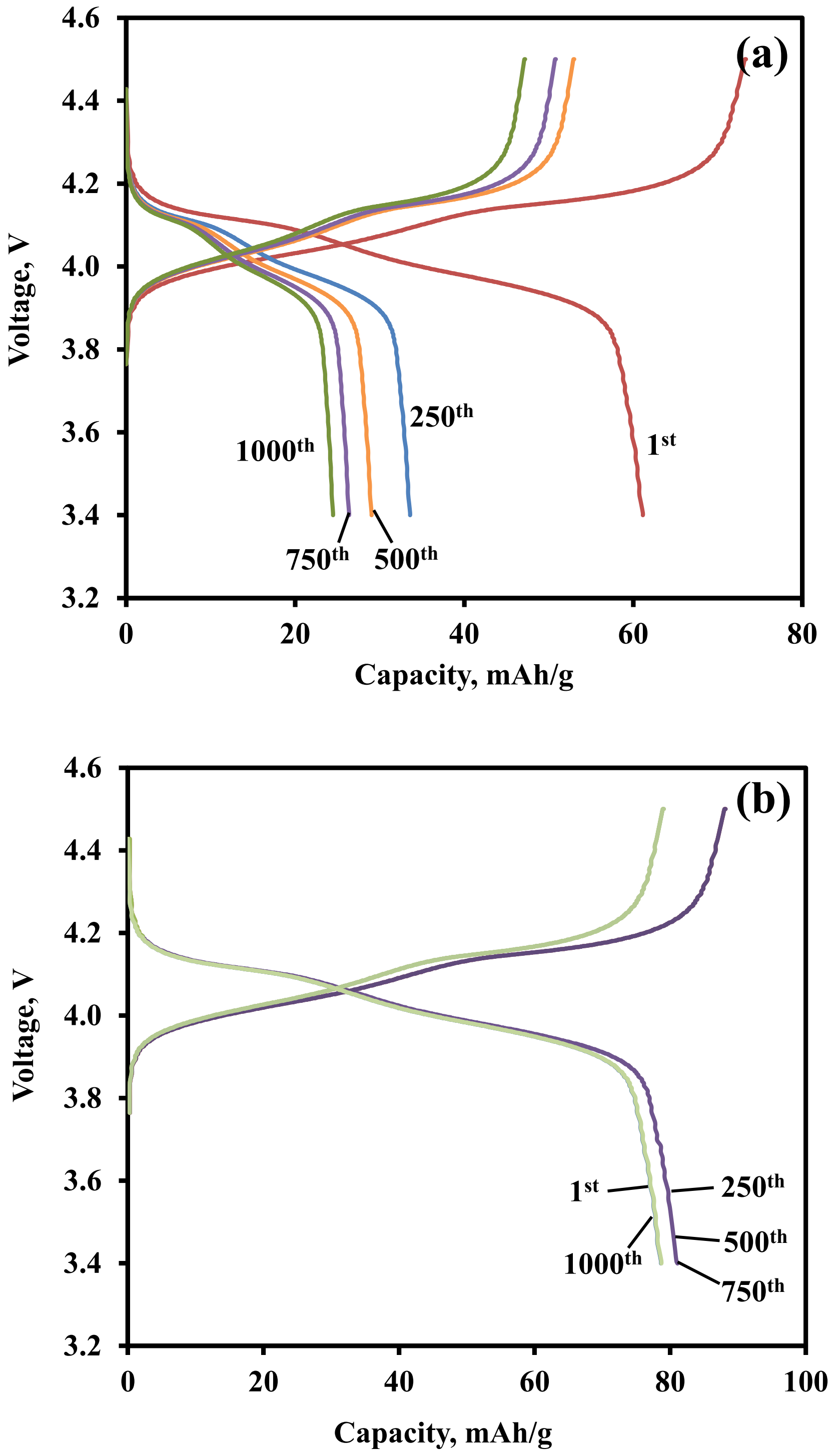

Figure 3. Galvanostatic charge-discharge capacities at various cycles of (a) uncoated and (b) 50 cycles of CeO_2 coated $LiMn_2O_4$ at room temperature. The samples were charged-discharged at a 1C rate between 3.4 V and 4.5 V.

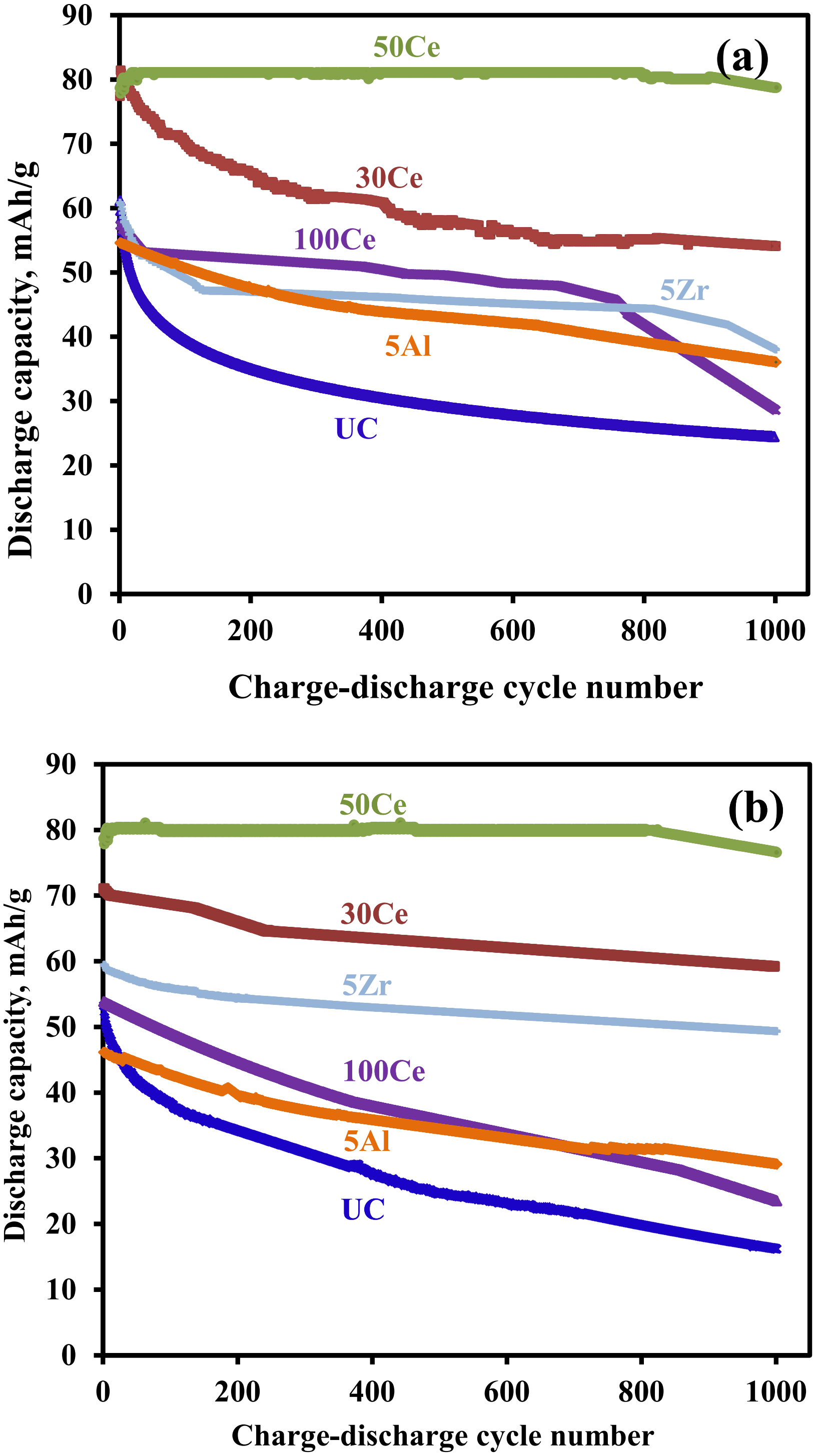

Figure 4. Discharge capacities of cells coated with various oxides at a 1C rate in a voltage range between 3.4 V and 4.5 V (a) at room temperature and (b) at 55 °C.

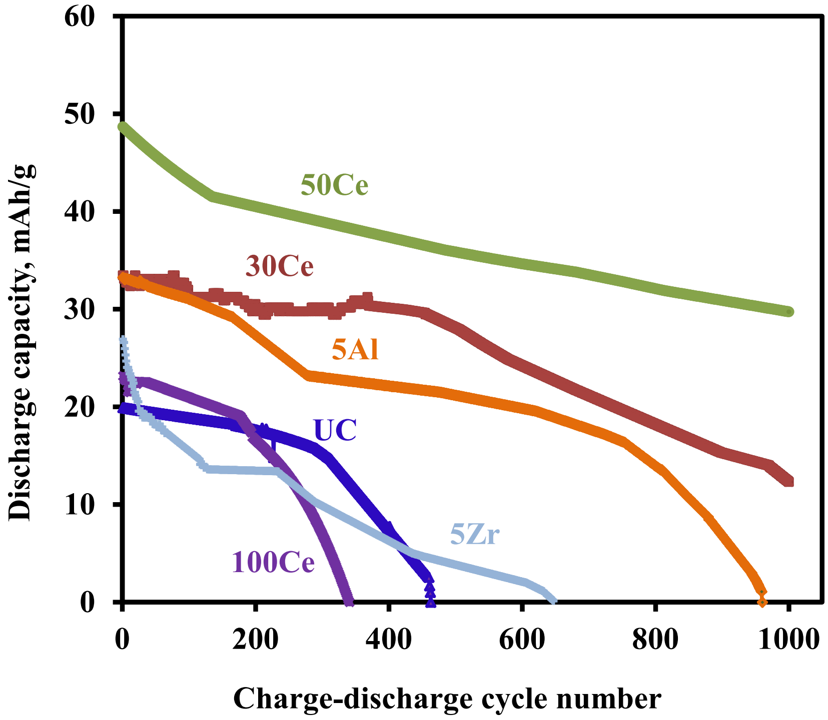

Figure 5. Discharge capacity of cells coated with various oxides at a 2C rate between 3.4 V and 4.5 V at room temperature.

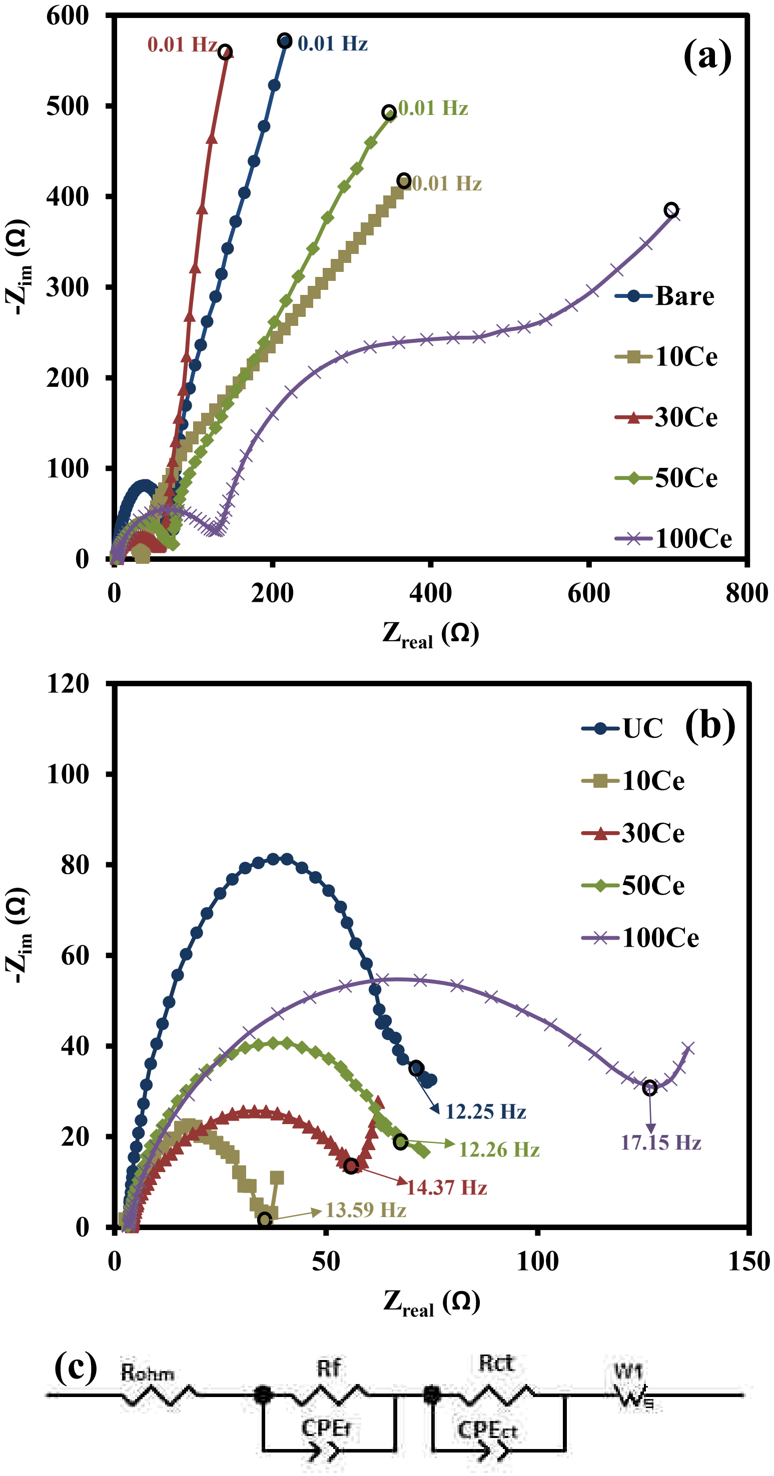

Figure 6. Electrochemical impedance spectra at 3.8 V for (a) uncoated and various oxides coated LiMn$_2$O$_4$ with 0th cycle at room temperature, (b) higher frequency (10MHz-1Hz) semi-circle region, and (c) equivalent circuit fit for the impedance spectra.

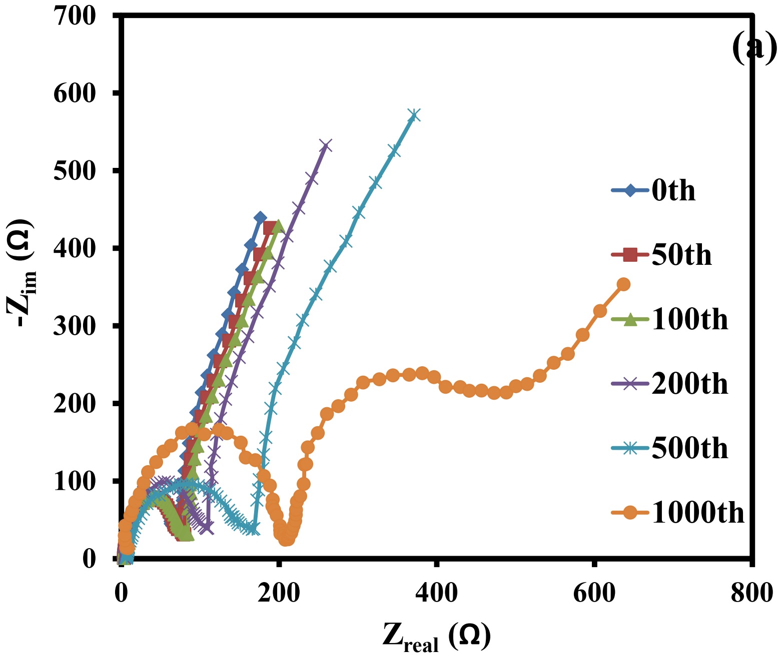

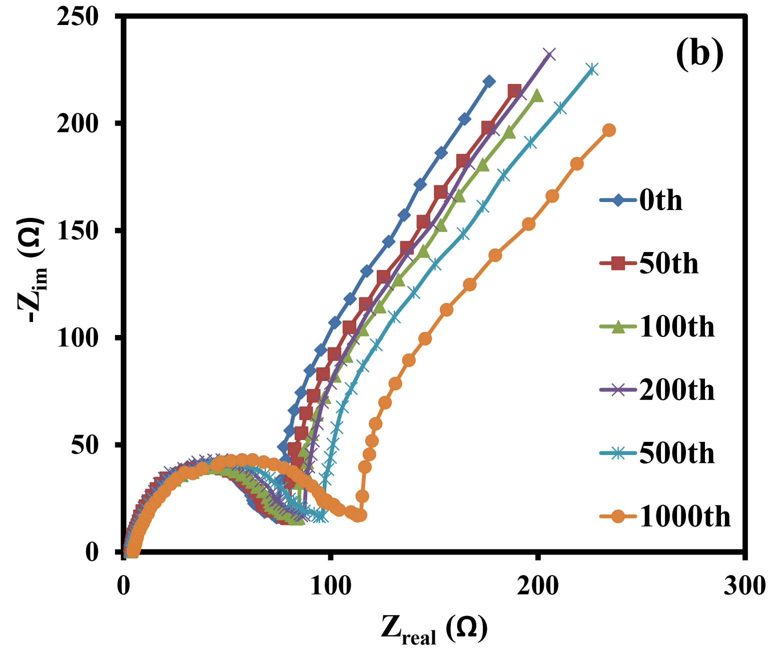

Figure 7. Electrochemical impedance spectra at 3.8 V for (a) uncoated and (b) 50 cycles of CeO_2 coated $LiMn_2O_4$ as a function of the cycle number of charge-discharge at a 1C rate in a voltage range between 3.4 V and 4.5 V at room temperature.

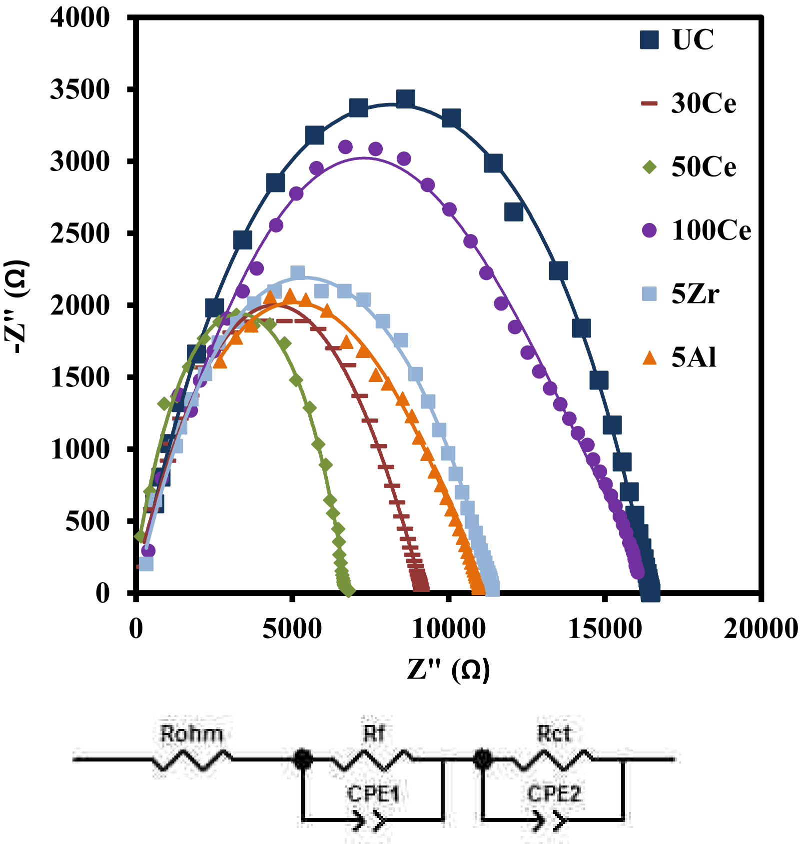

Figure 8. The ac complex impedance spectra at room temperature of the pellets made from the UC and 5Zr, 5Al, 30Ce, 50Ce, and 100Ce coated $LiMn_2O_4$ particles for the bulk conductivity measurement. Solid lines represent the fitted curve obtained using equivalent circuit model shown in the inset.

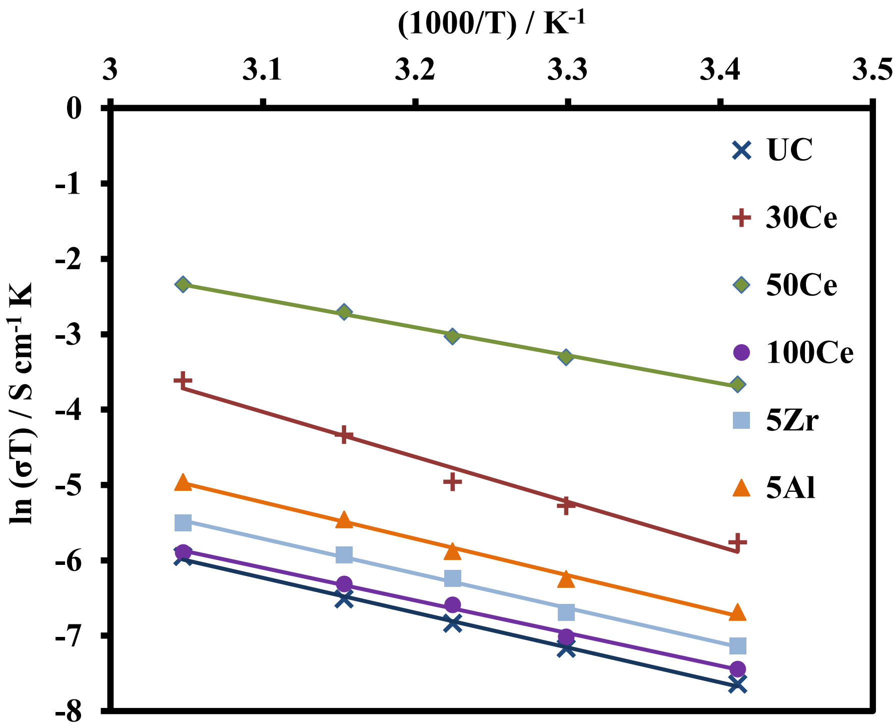

Figure 9. Arrhenius plot of the UC and 5Zr, 5Al, 30Ce, 50Ce and 100Ce coated $LiMn_2O_4$ particles for the effects of temperature on bulk conductivity.

Table 1. Impedance parameters using equivalent circuit models for the electrodes made from the UC, 5Al, 5Zr, 10Ce, 30Ce, 50Ce, and 100Ce coated $LiMn_2O_4$ particles.

Sample	**R_{ohm} (Ω)**		**R_f (Ω)**		**R_{ct} (Ω)**	
	0th	**1000th**	**0th**	**1000th**	**0th**	**1000th**
UC	9.1	11.29	19.0	36.8	88.1	139.2
10Ce	8.2	9.84	2.2	5.5	32.0	105.4
30Ce	8.9	10.68	3.2	6.7	50.4	154.2
50Ce	8.5	9	4.2	5.4	57.2	90.1
100Ce	8.6	10.32	14.2	32.4	130.3	200.1
5Al	8.7	9.87	14.5	55.1	75.1	99.1
5Zr	8.1	8.88	12.5	30.2	68.3	98.5

Supporting Information

Table S1. Impedance parameters using equivalent circuit models (shown in Figure 6) for the electrodes made from the UC, 5Al, 5Zr, 10Ce, 30Ce, 50Ce, and 100Ce coated $LiMn_2O_4$ particles.

											Warburg Short							
	R_{ohm} (Ω)		R_f (Ω)		R_{ct} (Ω)		C_f (μF)		C_{ct} (μF)		R_w (Ω)		τ (s)		P	
	0th	1000th	0th	1000th	0th	1000th	0th	1000th	0th	1000th	0th	1000th	0th	1000th	0th	1000th	0th	1000th
UC	9.1	11.29	19.0	36.8	88.1	139.2	13.05	10.59	4.65	1.29	5324	6678	112	190	0.89	0.69
50Ce	8.5	9	4.2	5.4	57.2	90.1	1.02	1.98	2.72	0.98	1205	2400	8.07	10.5	0.75	0.64
30Ce	8.9	10.68	3.2	6.7	50.4	154.2	5.14	3.78	4.06	1.87	2240	6332	24	49	0.56	0.72
10Ce	8.2	9.84	2.2	5.5	32.0	105.4	3.45	4.50	2.15	2.05	2803	5232	31	52	0.71	0.85
100Ce	8.6	10.32	14.2	32.4	130.3	200.1	15.54	3.54	6.13	5.4	4520	8750	98	160	0.82	0.90
5Al	8.7	9.87	14.5	55.1	75.1	99.1	10.52	1.52	3.5	0.21	3240	4210	95	120	0.65	0.54
5Zr	8.1	8.88	12.5	30.2	68.3	98.5	11.02	11.02	3.9	4.02	2529	2952	85	125	0.54	0.34

Table S2. Impedance parameters using equivalent circuit models (shown in Figure 8) for conductivity pellets made from UC, 5Al, 5Zr, 30Ce, 50Ce, and 100Ce coated $LiMn_2O_4$ particles.

	R_{ohm} (Ω)	R_f (Ω)	CPE1-T (F)	CPE1-P	R_{ct} (Ω)	CPE2-T (F)	CPE2-P
UC	52.11	12546	1.03E-07	0.56	4057	7.16E-06	0.41
30Ce	15.00	4.13E-09	2.10E-12	1.00	9198	5.87E-07	0.50
50Ce	11.25	6.58E-08	1.22E-13	1.00	6671	2.90E-08	0.67
100Ce	50.00	12305	2.62E-07	0.54	3654	1.55E-05	0.46
5Al	62.87	5650	2.50E-07	0.54	5180	1.82E-06	0.45
5Zr	10.42	8503	2.45E-07	0.55	2624	1.07E-05	0.40

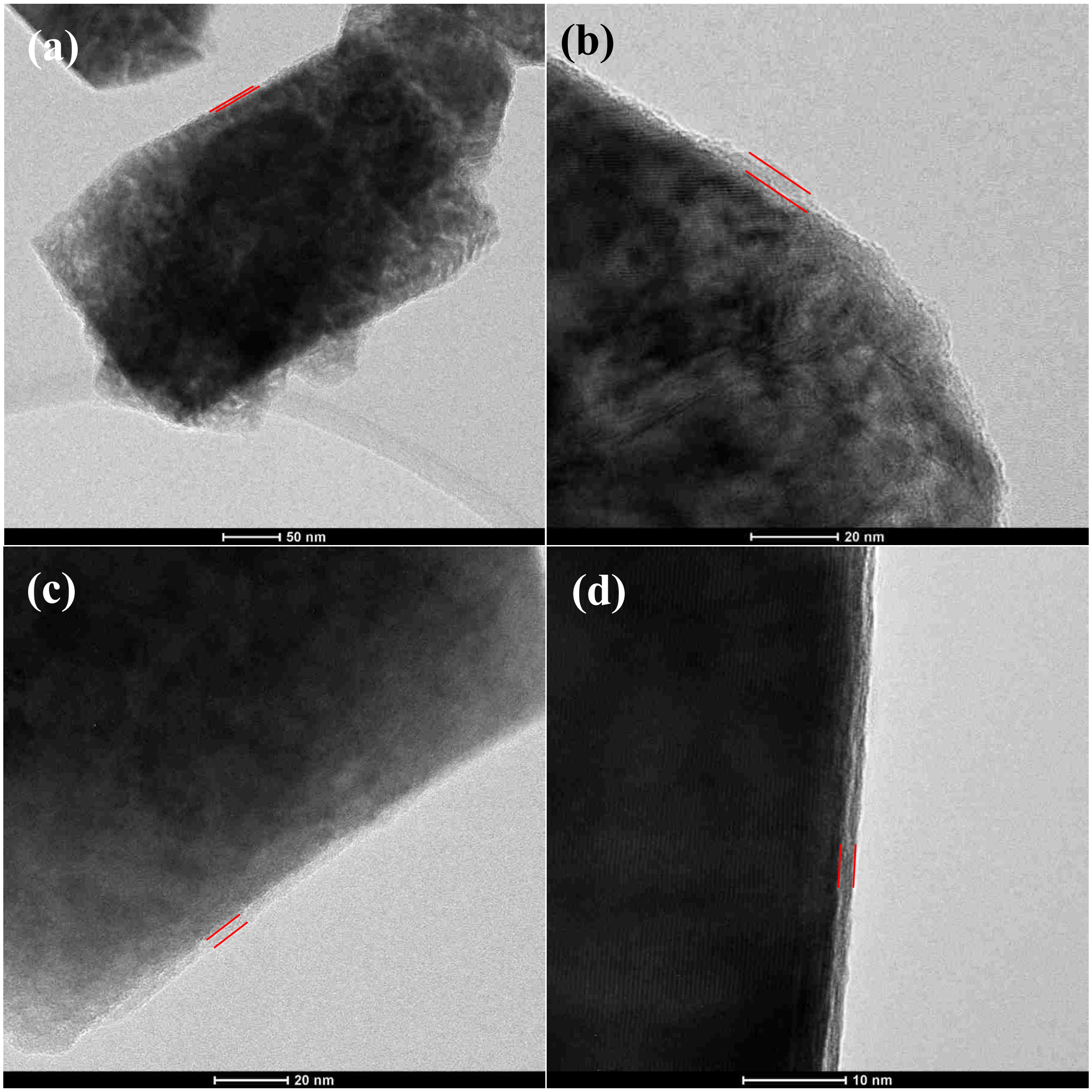

Figure S1. TEM images of $LiMn_2O_4$ particles coated with (a, b) 50 cycles CeO_2 ALD with about 3 nm thick film, (c) 5 cycles ZrO_2 ALD coated with about 3 nm thick film, and (d) 5 cycles of Al_2O_3 ALD coated with about 1.5 nm thick film. 5 cycles of Al_2O_3 ALD and 5 cycles ZrO_2 ALD in this study are among the optimal ALD film thicknesses based on previous reports.[1, 2] Thicker Al_2O_3 or ZrO_2 ALD films would significantly decrease the capacity due to the reduction in electron conductivity and possible reduction in Li-ion conductivity.[1]

References

[1] Y. S. Jung, A. S. Cavanagh, A. C. Dillon, M. D. Groner, S. M. George, S.-H. Lee, *Journal of The Electrochemical Society* **2010,** 157, A75.

[2] J. Zhao, Y. Wang, *Journal of Solid State Electrochemistry* **2013,** 17, 1049.

IV. Ionic and Electronic Conductivities of Thin Atomic Layer Deposited Film Coated Lithium Ion Battery Cathode Particles

Rajankumar L. Patel[1], Hooman Yaghoobnejad Asl[2], Amitava Choudhury[2], and Xinhua Liang[1,]*

[1] Department of Chemical and Biochemical Engineering,
Missouri University of Science and Technology, Rolla, MO 65409, United States

[2] Department of Chemistry, Missouri University of Science and Technology,
Rolla, MO 65409, United States

* Email: liangxin@mst.edu

ABSTRACT

It is imperative to ascertain the ionic and electronic components in the total conductivity of an electrochemically active material. A blocking technique called Hebb-Wagner method is normally used to explain the two components (ionic and electronic) in a mixed conductor, in combination with complex ac impedance method and dc polarization measurements. CeO_2 atomic layer deposition (ALD)-coated and uncoated, $LiMn_2O_4$ (LMO) and $LiMn_{1.5}Ni_{0.5}O_4$ (LMNO) powders were pressed into pellets and then painted with silver to act as a blocking electrode. Electronic conductivities were derived from currents obtained using dc Chronoamperometry mode. The ionic conductivities were calculated from results of the electronic conductivities and the mixed conductivities obtained from the ac impedance method. The results showed that the CeO_2 thin films coated LMO and LMNO are twice as much Li-ion conductive compared to the uncoated

LMO and LMNO. Also, insulating materials, such as alumina and zirconia ALD-coated LMO were also tested for comparison. No significant effect of substrates was noticed among coated and uncoated samples for their ionic conductivities, while the electronic conductivities of LMO was found to be higher than that of the LMNO samples. The Li-ion conductivity of the CeO_2 films and the optimal film thickness achieved by ALD indeed helped overcome the trade-off between long cycle-life and reduced initial capacity fade of LMO used as cathode in lithium ion batteries.

Introduction

A materials science and fabrication challenge is still stands in the way despite of the capacity improvements of contemporary lithium-ion batteries achieved by efficient transport of Li ions and electrons between the electrodes. The major issue lies in the cathodes used in these battery cells which are made of low electronic conductive metal oxides. The separator composition in the electrolyte, ideally, must allow ions only while establishing a safe, and electronically impermeable wall. The common problems include the low conductivity values of the electrodes, the phase transformations causing the change in the materials and their properties, and intrinsic struggle to detect and measure the microstructure and conductive properties of these materials. For example, recently, we coated $LiMn_2O_4$ (LMO) particles with ultrathin uniform CeO_2 films using atomic layer deposition (ALD) technique. In comparison to the uncoated particles, these coated particles displayed a substantial performance enhancement in capacity and charge-discharge cycling at room temperature and 55 °C for over 1,000 cycles. The samples coated with optimum film thickness of 3 nm CeO_2 improved the initial capacity by 24% compared to the uncoated LMO sample, and the coated sample retained 96% and 95% of its initial capacity even after cycling for 1,000 cycles at room temperature and 55 C at 1C rate, respectively.[1] The improved performance was due to the conductive nature of CeO_2; however the effect of CeO_2 thin films on Li ionic conductivity is yet to be investigated. It is very important to explore and explain the ionic and electronic components of the total conductivity of these thin film CeO_2 materials, which help enhance the battery performance and cycle life significantly.

Electrical conduction in materials may arise from motion in an electric field of electrons, ions, or both. For many materials, the charge carrier identity is implicit. For example, for metals and semimetals, such as carbon, charge is understood to be carried by mobile electrons, whereas for electrolyte materials such as salts dissolved in solvents and most polymer electrolytes, charge is understood to be carried by mobile ions.[2, 3] Some materials have the very interesting property that they may transport charge via both ions and electrons; such materials are known as mixed ionic electronic conductors (MIECs).[4, 5] MIEC materials are critically important in many electrochemical technologies, for example in battery electrodes,[6-10] fuel-cell electrodes,[11] and in certain types of membrane reactor.[12, 13]

Maier reported an outline to comprehend the effect of space charge regions on the ionic transport.[14] In nanocrystalline materials, interfacial regions occupy a much greater fraction of the internal volume, and subsequent research in nano-ionics has focused on achieving an improved understanding of the charge transport properties of nanostructured ionic solids. The electronic and the ionic partial conductivity can be separated by applying one or two electrodes that block either the electronic or the ionic current.[14, 15] After a waiting period of a few times, the relaxation time (τd), a steady state is reached in which only the non-blocked species move (cf. Hebb-Wagner polarization). From the steady state current-voltage (I-V) relation, the electronic partial conductivity can be calculated.

In this work, LMO and $LiMn_{1.5}Ni_{0.5}O_4$ (LMNO) particles coated with ultrathin conformal CeO_2 films by ALD were used to analyze the electronic and ionic contributions from the ultrathin films. In order to understand the true effect of coating, we deposited the same thickness of ceria films on different substrates. The same number of ALD cycles were carried out for both substrates at the same operating conditions. Since our aim was also to focus on testing the conductivities at around working temperature range, we did not test them at temperatures higher than 100 °C. The results of the conductive ceria coatings were compared with, insulating materials, alumina and zirconia ALD-coated LMO samples. A common method used to separate the various contributions, for the uncoated and CeO_2 ALD-coated LMO and LMNO samples, is the so-called *Hebb–Wagner* polarization, in which a blocking electrode, capable of supporting only one conduction type (electronic or ionic),[16] is employed along with ac impedance measurements.

Results and Discussions

Various thicknesses of CeO_2 films were conformally coated on the surfaces of LMO particles (~8 µm, L-140 from LICO Technology Corporation) and LMNO particles (~5 µm, NEI Corporation) using ALD. 30 cycles CeO_2 ALD (30Ce-LMO, 30Ce-LMNO), 50 cycles CeO_2 ALD (50Ce-LMO, 50Ce-LMNO), and 100 cycles CeO_2 ALD (100Ce-LMO, 100Ce-LMNO) were performed on different batch of particles. The transmission electron microscopy (TEM) image of an uncoated LMO particle (shown in Fig. 1a) displays a clean edge of a pristine particle. In contrast, Fig. 1b displays a distinctive conformal coating of ~3 nm layer on a LMO particle after 50 cycles of CeO_2 ALD. Fig. 1c also shows ~3 nm layer on LMNO, and Fig. 1d shows ~5 nm conformal film on LMNO. This shows that the ALD coating process is a consistently repeatable layer-by-layer technique. Due to their electronic insulating nature, different cycles of Al_2O_3 and ZrO_2 ALD-coated LMO particles were also tested the same way to distinguish the conductivities. Different thicknesses of coating 2 cycles of Al_2O_3 (2Al), 5 cycles of Al_2O_3 (5Al), 10 cycles of Al_2O_3 (10Al), 5 cycles of ZrO_2 (5Zr) and 10 cycles of ZrO_2 (10Zr) ALD-coated samples were tested. These samples with the described cycles of coating were selected because it is known to have the similar film thickness as compared to 50Ce and 100Ce samples.

The ac impedance measurements at 1 mHz – 1 MHz range were conducted for cold-pressed pellets of all eight samples. The pellets were coated with silver paste, using a blocking electrode material. All the tests were limited to 100°C temperature since we were only interested in testing the samples at real working conditions. Fig. 2 shows the Nyquist impedance plots for the samples obtained by testing across the two silver pasted coated sides of the samples. The solid curves represent the fitted curves obtained by using equivalent circuit shown in Fig. 2e. In the equivalent circuit, R_1 refers to the pure electronic resistance of the material because at very low frequency (0.01 Hz in this case), there is no movement of ions. R_2 referes to the ionic resistance which refers to the impedance measured at high frequency (1 MHz), and CPE is the constant phase-angle element depicting the non-ideal capacitance of the material. Again, the real axis intercept at zero frequency (zero phase) signifies electronic resistivity; for electronically non-conductive samples, the resistivity becomes infinite at zero frequency with a non-zero phase angel.

The fitted parameters are provided in the Table 1. The impedance value for the uncoated LMO sample is double compared to any of the ceria coated samples. Nyquist plot of 50Ce-LMO shows that its impedance is half of the LMO pellet. This shows that the LMO pellet exhibits much more resistance for the movement of ions and electrons. These trends are also noticed for the uncoated and coated LMNO substrates. It indicates that the ceria thin film coating does induce some conductivity to the substrates. The impedance for the 100Ce sample was lower than the uncoated substrates but higher than the 30Ce and 50Ce coated samples. This could be due to the thicker film of the ceria coating, which creates longer pathways for the ions migration.

As already pointed out,[14, 17] the determination of the electronic or the ionic partial conductivity requires two electrodes blocking to one of the mobile charge carriers, this leads to a polarization of the bulk, which can be observed in ac experiments at low frequencies or in dc experiments after a long waiting period. For a single crystalline mixed conductor with negligible electrode capacitance, this polarization leads to a Warburg element, and is approximately described by the equivalent circuit.

The equivalent circuit consists of elements corresponding to one Nyquist semicircle, which is consistent with the data in Fig. 3. The equivalent circuit constitutes a combination of ionic and electronic components, which are in parallel to each other. The equivalent circuit in Fig. 2b indicates that the high-frequency semicircle diameter, R_1, is the parallel combination of ionic and electronic resistance.[18, 19]

$$\frac{1}{R_1} = \frac{1}{R_i} + \frac{1}{R_e} \qquad (1)$$

where R_e is the electronic resistance. This enables determination of R_i.

Indeed EIS alone is enough for separating ionic and electronic resistances (responses at zero frequency and infinite frequency). The dc polarization tests were conducted to verify the fact that the system shows electronic behavior at zero frequency. In this way dc polarization tells us that there will be nothing new on going to slower frequencies than the one employed in the EIS test. Therefore, the results of EIS and dc polarization should converge when frequency moves to zero. In this occasion, dc polarization gave very similar results, as shown in Table 2, as the R_e resistance values obtained from the EIS measurements, as shown in Table 1. The applied dc potential and the resulting current (after a short wait time) may be assigned only to electrons, as mentioned later in the text.

Fig. 3 shows the Arrhenius plots of the electronic conductivity of LMO particles with and without 50Ce coating. The results were entirely reproducible. That is, they always returned to approximately the same value each time when equilibrium was reached at any given temperature. Each point represents the equilibrium value obtained from several determinations. The LMO itself has been noted to have semiconductor nature due to its crystal orientation.[20] One thing is very noticeable that the total conductivity of 50Ce is almost two magnitude higher than the uncoated LMO sample, which corresponds to the results shown in the Fig. 2. From the results, it is clear that conductivity was improved by the coating of CeO_2 on the LMO and LMNO primary particles. Based on the conductivity results, it can be said that CeO_2 is a promising candidate for improving the conductivity in a manganese based oxide lithium-ion battery.[17]

Electronic and ionic conductivities of all the samples by using the methods described as above, at different temperatures, and the results are shown in Fig.s 3 and 4, respectively. All samples show an increase in electronic and ionic conductivities with increasing temperature from 25 °C to 100 °C. The temperature dependence on conductivity was fit to the Arrhenius equation:

$$\sigma_a = \mathrm{A}_0 \cdot \exp\left(\frac{-\mathrm{E}_a}{\mathrm{RT}}\right) \qquad (2)$$

where σ_a is the electronic or ionic conductivity, A_0 is a pre-exponential factor, and E_a is the activation energy. The pure conductivities are plotted against temperature in Fig. 5. However, the electronic conductivities of the ceria coated sample, for both substrates, was higher than that of the uncoated sample. This could be as a result of the higher grain boundary resistance in the uncoated sample. The coated samples has conformal coating of CeO_2, which provides a continuous pathway for the electrons to move around. 50Ce coated samples for both substrates (covered with ~3 nm conformal film) showed the highest ionic conductivity. The slopes of 100Ce coated samples were slightly different than the other ceria coated samples, which could indicate that the thicker coating caused the change in the relationship between temperature and conductivity. It is important to note that the electronic conductivity of the uncoated LMNO was lower than the LMO samples. This is in support of the reported values for these materials, which is 10^{-4} S/cm for LMO and $\sim 10^{-6}$ S/cm for LMNO.[8, 21, 22] However, there was no apparent effect of substrate noticed for the coated samples. The magnitude of the improved conductivities were comparable to one another. This shows that the conformal coating of the same thickness was truly conductive in nature and as a result, it can help improve the performance of lithium-ion batteries.

From Fig. 4, the conditions, which are most favorable for ionic conduction, are the lower temperatures investigated (<373 K). This is in agreement with the results of Schmalzried's, which were performed using similar technique.[23] The ionic conductivities of the samples increased linearly with increase in temperature. However, the uncoated sample showed poor ionic conductivity compared to the 50Ce coated samples. The ionic conductivities for 50Ce-LMO and 50Ce-LMNO samples were more than one magnitude higher than the uncoated LMO and LMNO samples and it showed the linear increase of conductivity with respect to temperature. Also, ionic conductivity of the uncoated sample did not surge rapidly with temperature, which suggested that electronic conduction was playing the prominent role.[24, 25] The 100Ce coated substrates showed better conductivity than the uncoated samples, but their different slopes indicated that the thicker coating affected the temperature relationship with conductivity.

The insulating materials showed much less conductivity as expected, shown in Fig. 5. The faint conductivity enhancement observed in the 2Al, and 5Al samples can be attributed to the fact that the existence of Al_2O_3 films acts as contact bridges between the spinel particles. Thus, the inter-particle resistance is reduced and the insertion/extraction process can proceed across the electroactive material. It should be emphasized that the metal oxide dispersed cannot originally increase the electrical conductivity of the $LiMn_2O_4$ film, due to its higher resistance. Indeed, the ultra-thin Al_2O_3 film provides an opportunity for easier diffusion of Li ions through the electroactive film. However, if the thickness is increased enough, such as in 10Al, the film resistance increases significantly, due to the inherent insulating nature of alumina. It has been reported that adding thick Al_2O_3 atomic layers (20–40 ALD) could increase the ionic and electronic resistance and thus increase polarization.[26] The R^2 values of all the samples are at least more than 0.995. The slopes of electronic conductivities of the alumina and zirconia ALD-coated samples changed slightly more positive, indicating the higher activation energy requirement. The

2Al and 5Zr samples showed about one order of magnitude higher electronic conductivity and almost no ionic conductivity, compared to the uncoated LMO sample. Table 3 shows the dc conductivities of the alumina and zirconia coated samples. The values are very close to the electronic resistance of the impedance curves for each samples.

It is noticeable that the difference in conductivities of alumina and zirconia coated samples with same film thickness is small. Also, with increase in film thickness (i.e., more ALD cycles), both ionic as well as electronic conductivities of the samples drop. This could be explained by the fact that decreasing the feature size (grain size or film thickness) from the micrometer to the nanometer scale usually results in a remarkable change in the transport properties of materials.[27] In comparison with their microstructured counterparts, the most remarkable characteristic of nanostructured materials is the high interfacial density. This leads to two nano-effect: the trivial size effect and the true size effect.[28, 29] Thus, the samples with higher thickness of ceria, alumina, and zirconia coating are showing negative effects on the conductivity of the coated samples. So, even though the ALD coating reduces the gap between two particles in the case of alumina and zirconia coated samples, the inherent nature of the coating does not help improve the conductivity. That resulted in the lower performance of coin cell as tested previously.[1]

The study of the electronic conductivities of LMO helped to understand the effects of CeO_2 to be a predominantly ionic conductor depending on temperature. The comparable results of the ceria coated LMO and LMNO samples shows that the deposited films were indeed more ionically conductive than the uncoated samples. This results satisfactorily explain the significant improvement in electrochemical performance of the ceria coated LMO samples reported previously.[1] The Li-ion conductivity of the CeO_2 films and the optimal film thickness achieved by ALD indeed helped overcome the trade-off between long cycle-life and initial discharge capacity.

Conclusions

The effective ionic and electronic conductivity contributions in the CeO_2 ALD-coated and uncoated LMO and LMNO were obtained from the mixed conductivities. An ac impedance spectroscopy enabled the determination of electronic and ionic conductivity in the samples. The electronic conductivity measurements were verified using dc measurements. The clear distinction among the ionic conductivities of the CeO_2 coated and the uncoated LMO and LMNO indicated that the ALD coated ultrathin ceria films is much more Li-ion conductive. Also, the insulating materials like Al_2O_3 and ZrO_2 optimal-thin-film coated samples showed almost no ionic conductivity compared to the 50Ce-LMO sample, which showed about 1.5 times higher order of magnitude of ionic conductivity. The electronic conductivity of the LMO samples was higher than that of the LMNO samples, while the ionic conductivities for LMO was about one magnitude higher than the LMNO. The pure electronic conductivity contributions were significantly higher than pure ionic conductivity contributions for the samples from both substrates. The experiments were also able to show that the thicker coating of ceria films are less conductive than the optimal thin film (50Ce). This was expected since the material under test is slightly semiconductor in nature. This work provided supporting explanation for our previous work, as in the reason for significantly better performance of the optimal ultrathin ceria films coated LMO particles compared the uncoated cathodes.

Experimental Section

ALD coating: A fluidized bed reactor was used to perform ALD to coat different thicknesses of CeO_2 thin layers on $LiMn_2O_4$ powders and $LiMn_{1.5}Ni_{0.5}O_4$ at 250 °C. The two reactant chemicals were Tris(ipropylcyclopentadienyl) cerium ($Ce(iPrCp)_3$) (99.9%, Strem Chemicals) and de-ionized water. All chemicals were used as received. The ALD coating processes for the CeO_2, Al_2O_3, and ZrO_2 are described elsewhere.[1] The coated particles were visualized using FEI Tecnai F20 TEM/STEM supported with an energy dispersive X-ray spectrometer system.

Conductivity measurements: Different samples were cold pressed (20 MPa) into pellets and then coated with silver conductive paste (Sigma Aldrich) to make the blocking electrodes for conductivity measurements. The paste was vacuum dried at 85 °C for 8 hr. The conductivity measurements were performed at 1 mHz – 1 MHz frequency range using IviumStat impedance analyzer.[30, 31] The impedance spectra were examined by EC-Lab software (Bio-Logic SAS). The dc measurements were conducted using the same setup under vacuum to verify the electronic conductivity of each samples. The pellets were tested at a constant increment of 0.2 V up to 1.4 V and the corresponding current was monitored after 60 s stabilization time at each step. The samples were tested at a temperature ranging from 25 °C – 100 °C in a box furnace. The furnace and the pellets were allowed to stabilize for at least 1 hr once the temperature was reached. For dc measurements, the same IviumStat was used in the dc mode with ChronoAmperometry transient. The measurement current direction was parallel to the film plane. The recorded impedance spectra were analyzed using complex non-linear least squares (CNLS) fitting to find the appropriate electrical equivalent circuit. The calculated resistance components were confined within 4% of uncertainties.

References

1. Patel, R. L.; Xie, H.; Park, J.; Asl, H. Y.; Choudhury, A.; Liang, X., Significant Capacity and Cycle-Life Improvement of Lithium-Ion Batteries through Ultrathin Conductive Film Stabilized Cathode Particles. *Advanced Materials Interfaces* **2015,** 2, (8), 1500046.

2. Bard, A.; Faulkner, L., *Electrochemical Methods: Principles and Applications*. John Wiley and Sons: 2001.

3. Kittel, C., *Introduction to Solid State Physics*. Wiley: 2005.

4. Yokota, I.; Miyatani, S., Conduction and Diffusion in Ionic-electronic Conductors. *Solid State Ionics* **1981,** 3, 17-21.

5. Weppner, W.; Huggins, R. A., Electrochemical Methods for Determining Kinetic Properties of Solids. *Annual Review of Materials Science* **1978,** 8, (1), 269-311.

6. Peter, L., A Systematic Approach to the Impedance of Surface Layers with Mixed Conductivity Forming on Electrodes. *Journal of Solid State Electrochemistry* **2013,** 17, (12), 3075-3081.

7. Patel, S. N.; Javier, A. E.; Balsara, N. P., Electrochemically Oxidized Electronic and Ionic Conducting Nanostructured Block Copolymers for Lithium Battery Electrodes. *ACS Nano* **2013,** 7, (7), 6056-6068.

8. Park, M.; Zhang, X.; Chung, M.; Less, G. B.; Sastry, A. M., A Review of Conduction Phenomena in Li-ion Batteries. *Journal of Power Sources* **2010,** 195, (24), 7904-7929.

9. Ma, J.; Wang, C.; Wroblewski, S., Kinetic characteristics of mixed conductive electrodes for lithium ion batteries. *Journal of Power Sources* **2007,** 164, (2), 849-856.

10. Chen, Y. H.; Wang, C. W.; Zhang, X.; Sastry, A. M., Porous Cathode Optimization for Lithium Cells: Ionic and Electronic Conductivity, Capacity, and Selection of Materials. *Journal of Power Sources* **2010,** 195, (9), 2851-2862.

11. Tsipis, E. V.; Kharton, V. V., Electrode Materials and Reaction Mechanisms in Solid Oxide Fuel Cells: A Brief Review. *Journal of Solid State Electrochemistry* **2008,** 12, (9), 1039-1060.

12. Wei, Y.; Yang, W.; Caro, J.; Wang, H., Dense Ceramic oxygen Permeable Membranes and Catalytic Membrane Reactors. *Chemical Engineering Journal* **2013,** 220, 185-203.

13. Leo, A.; Liu, S.; da Costa, J. C. D., Development of Mixed Conducting Membranes for Clean Coal Energy Delivery. *International Journal of Greenhouse Gas Control* **2009,** 3, (4), 357-367.

14. Maier, J., Ionic Conduction in Space Charge Regions. *Progress in Solid State Chemistry* **1995,** 23, (3), 171-263.

15. Tschope, A.; Sommer, E.; Birringer, R., Grain Size-dependent Electrical Conductivity of Polycrystalline Cerium Oxide I. Experiments. *Solid State Ionics* **2001,** 139, (3-4), 255-265.

16. Riess, I., 4-Point Hebb-Wagner Polarization Method for Determining the Electronic Conductivity in Mixed Ionic-electronic Conductors. *Solid State Ionics* **1992,** 51, (3-4), 219-229.

17. Huang, W.; Gopalan, S.; Pal, U., Measurement of Partial Oxygen Ion Conductivity of Sr-doped Lanthanum Manganite. *Journal of Power Sources* **2007,** 173, (2), 887-890.

18. Huggins, R. A., Simple Method to Determine Electronic and Ionic Components of the Conductivity in Mixed Conductors: A Review. *Ionics* **2002,** 8, (3-4), 300-313.

19. Jamnik, J.; Maier, J., Treatment of the Impedance of Mixed Conductors Equivalent Circuit Model and Explicit Approximate Solutions. *Journal of The Electrochemical Society* **1999,** 146, (11), 4183-4188.

20. Mandal, S.; Amarilla, J. M.; Ibáñez, J.; Rojo, J. M., The Role of Carbon Black in $LiMn_2O_4$-based Composites as Cathodes for Rechargeable Lithium Batteries. *Journal of The Electrochemical Society* **2001,** 148, (1), A24-A29.

21. Kunduraci, M.; Al-Sharab, J. F.; Amatucci, G. G., High-Power Nanostructured $LiMn_{2-x}Ni_xO_4$ High-Voltage Lithium-Ion Battery Electrode Materials: Electrochemical Impact of Electronic Conductivity and Morphology. *Chemistry of materials* **2006,** 18, (15), 3585-3592.

22. Kunduraci, M.; Amatucci, G., Synthesis and Characterization of Nanostructured 4.7 V $Li_xMn_{1.5}Ni_{0.5}O_4$ Spinels for High-Power Lithium-Ion Batteries. *Journal of The Electrochemical Society* **2006,** 153, (7), A1345-A1352.

23. Schmalzried, H., Electrical Conduction in Magnesium Oxide. *The Journal of Chemical Physics* **1960,** 33, (3), 940-941.

24. Saab, A. P.; Garzon, F. H.; Zawodzinski, T. A., Determination of Ionic and Electronic Resistivities in Carbon/polyelectrolyte Fuel-cell Composite Electrodes. *Journal of the Electrochemical Society* **2002,** 149, (12), A1541-A1546.

25. Siroma, Z.; Hagiwara, J.; Yasuda, K.; Inaba, M.; Tasaka, A., Simultaneous Measurement of the Effective Ionic Conductivity and Effective Electronic Conductivity in a Porous Electrode Film Impregnated with Electrolyte. *Journal of Electroanalytical Chemistry* **2010,** 648, (2), 92-97.

26. Li, J.; Xiao, X.; Cheng, Y.-T.; Verbrugge, M. W., Atomic Layered Coating Enabling Ultrafast Surface Kinetics at Silicon Electrodes in Lithium Ion Batteries. *The Journal of Physical Chemistry Letters* **2013,** 4, (20), 3387-3391.

27. Iguchi, E.; Tokuda, Y.; Nakatsugawa, H.; Munakata, F., Electrical transport properties in $LiMn_2O_4$, $Li_{0.95}Mn_2O_4$, and $LiMn_{1.95}B_{0.05}O_4$ (B= Al or Ga) around room temperature. *American Institute of Physics* **2002,** 91, (4), 2149-2154.

28. Maier, J., Nanoionics: Ion transport and electrochemical storage in confined systems. *Nature Materials* **2005,** 4, (11), 805-815.

29. Maier, J., Nanoionics: Ionic charge carriers in small systems. *Physical Chemistry Chemical Physics* **2009,** 11, (17), 3011-3022.

30. Atkinson, A.; Baron, S. A.; Brandon, N. P., AC Impedance Spectra Arising from Mixed Ionic Electronic Solid Electrolytes. *Journal of the Electrochemical Society* **2004,** 151, (5), E186-E193.

31. Lai, W.; Haile, S. M., Impedance Spectroscopy as a Tool for Chemical and Electrochemical Analysis of Mixed Conductors: A Case Study of Ceria. *Journal of the American Ceramic Society* **2005,** 88, (11), 2979-2997.

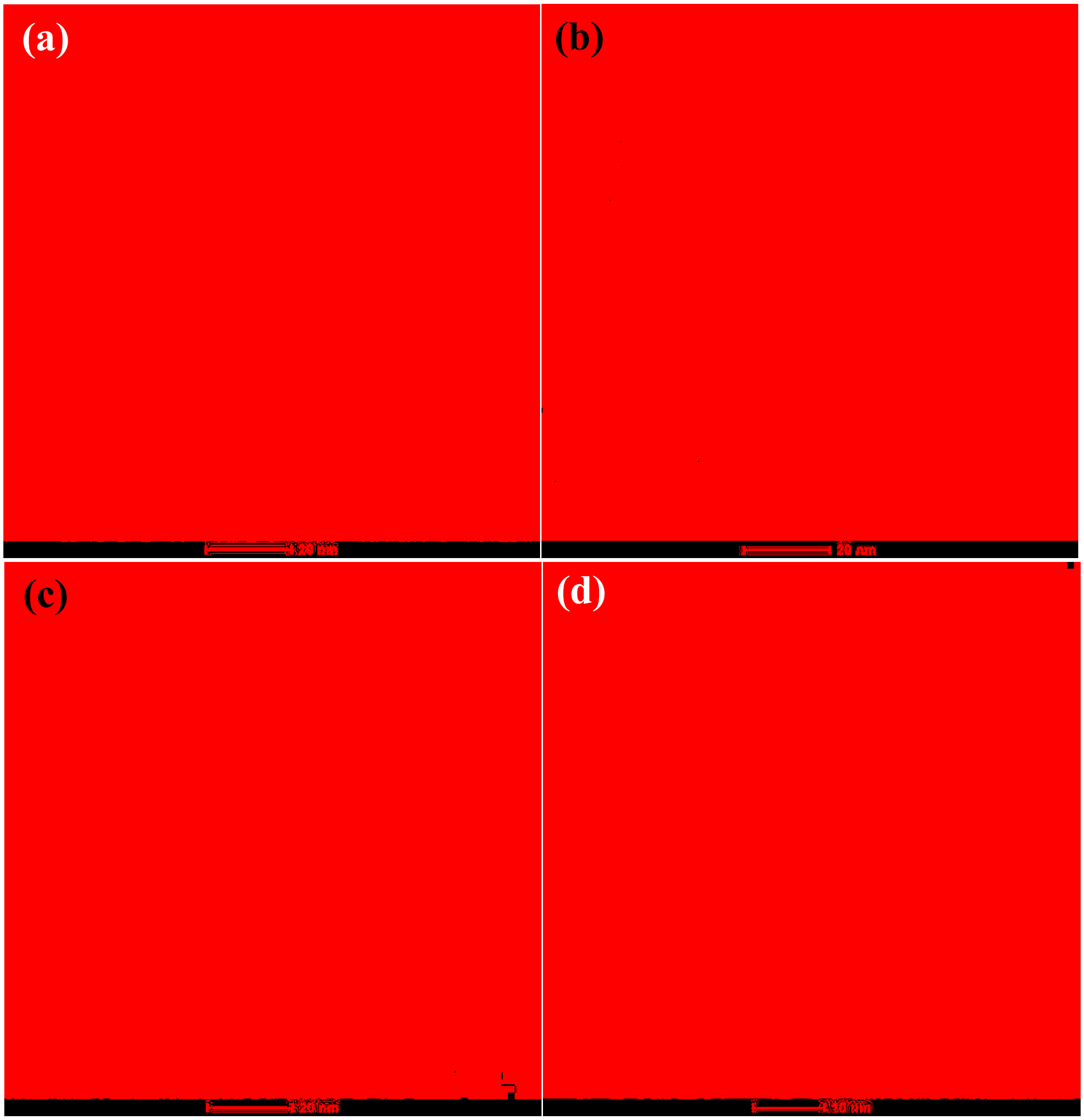

Fig. 1. TEM images of (a) uncoated, and (b) 50Ce coated $LiMn_2O_4$ particles, and (c) 50Ce, and (d) 100Ce coated $LiMn_{1.5}Ni_{0.5}O_4$ particles.

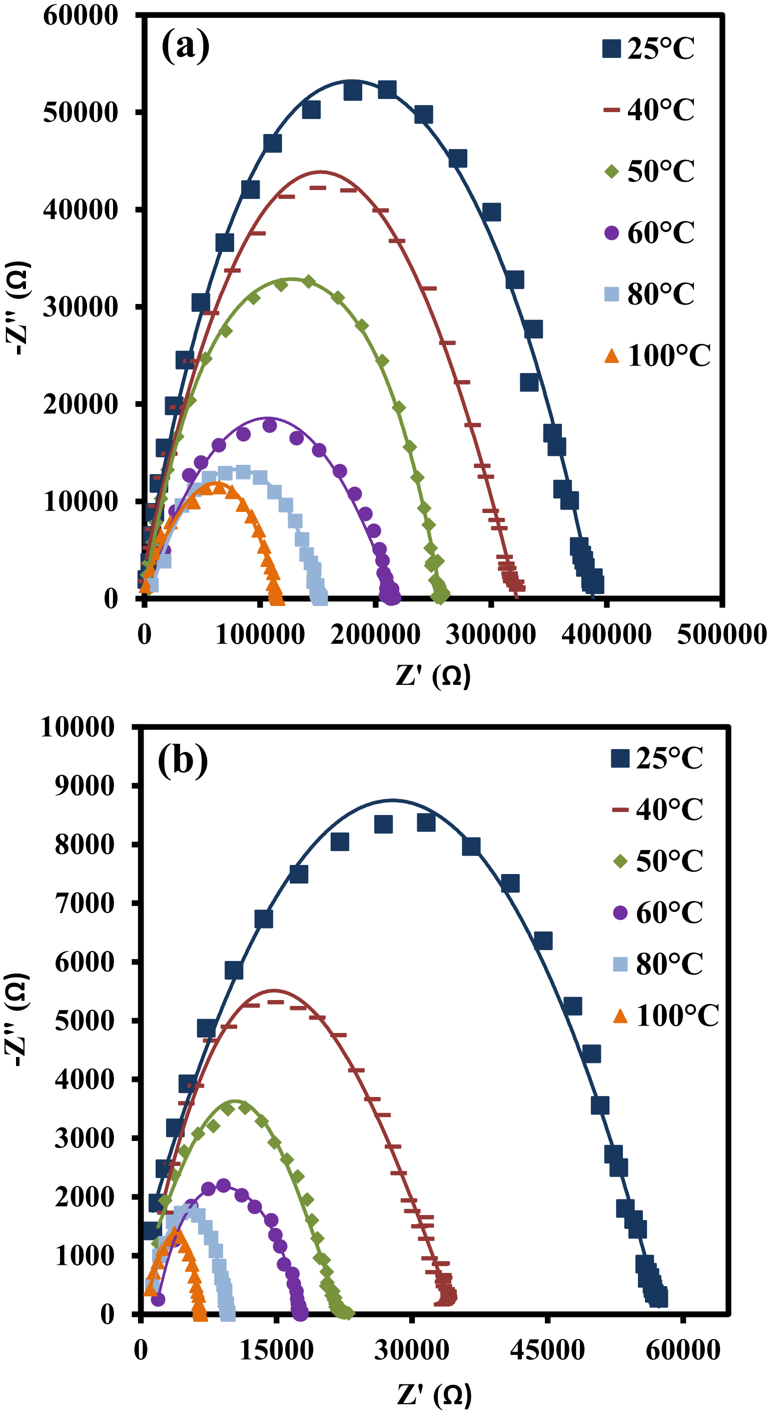

Fig. 2. Nyquist impedance plots at different temperatures for (a) uncoated and (b) 50Ce coated $LiMn_2O_4$, and (c) uncoated and (d) 50Ce coated $LiMn_{1.5}Ni_{0.5}O_4$, with corresponding fit (solid curve) using (e) the proposed equivalent circuit.

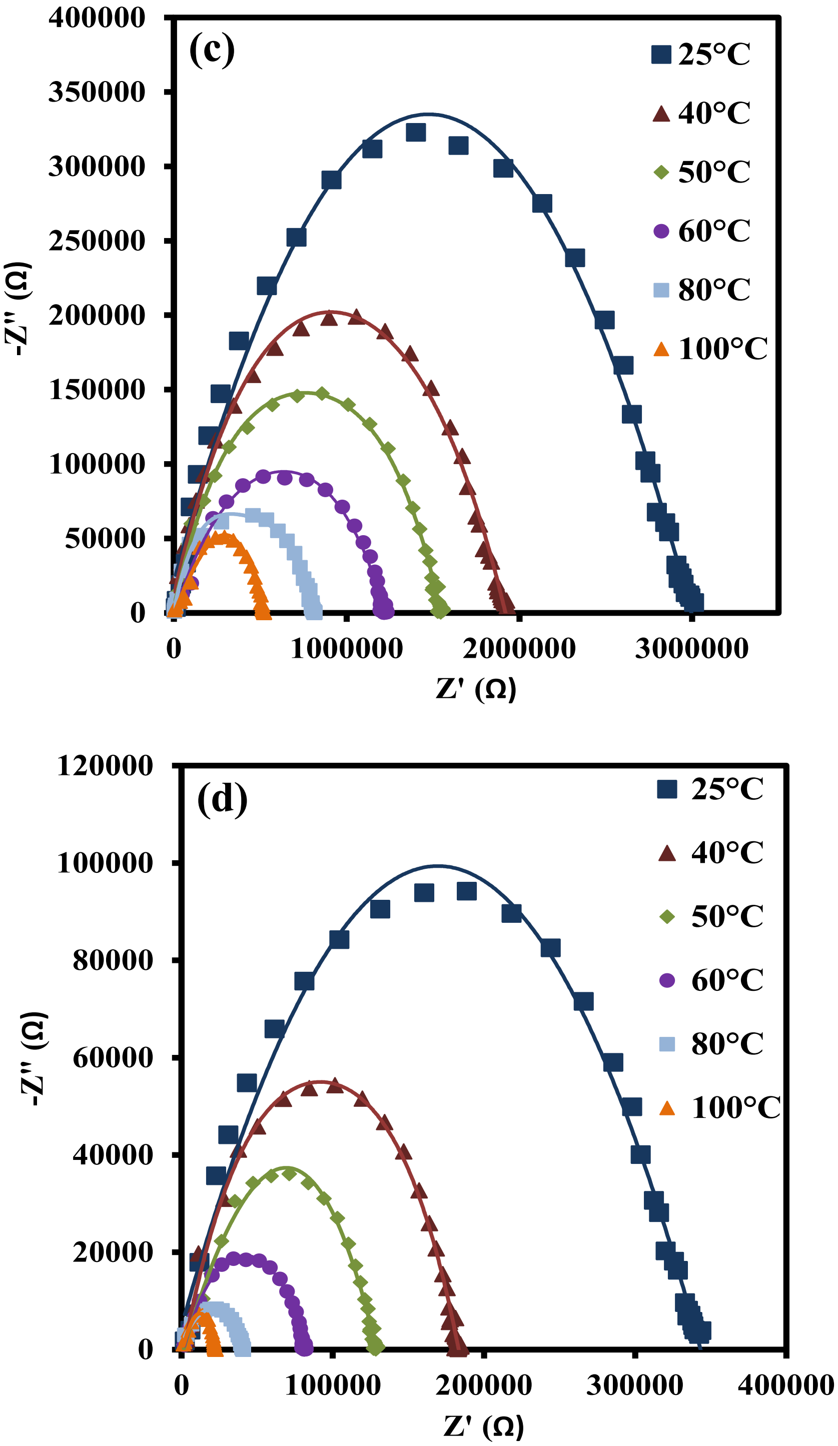

Fig. 2. Nyquist impedance plots at different temperatures for (a) uncoated and (b) 50Ce coated $LiMn_2O_4$, and (c) uncoated and (d) 50Ce coated $LiMn_{1.5}Ni_{0.5}O_4$, with corresponding fit (solid curve) using (e) the proposed equivalent circuit. (Cont.)

(e)

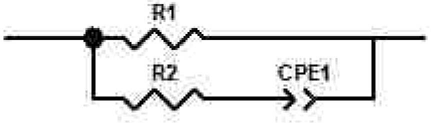

Fig. 2. Nyquist impedance plots at different temperatures for (a) uncoated and (b) 50Ce coated $LiMn_2O_4$, and (c) uncoated and (d) 50Ce coated $LiMn_{1.5}Ni_{0.5}O_4$, with corresponding fit (solid curve) using (e) the proposed equivalent circuit. (Cont.)

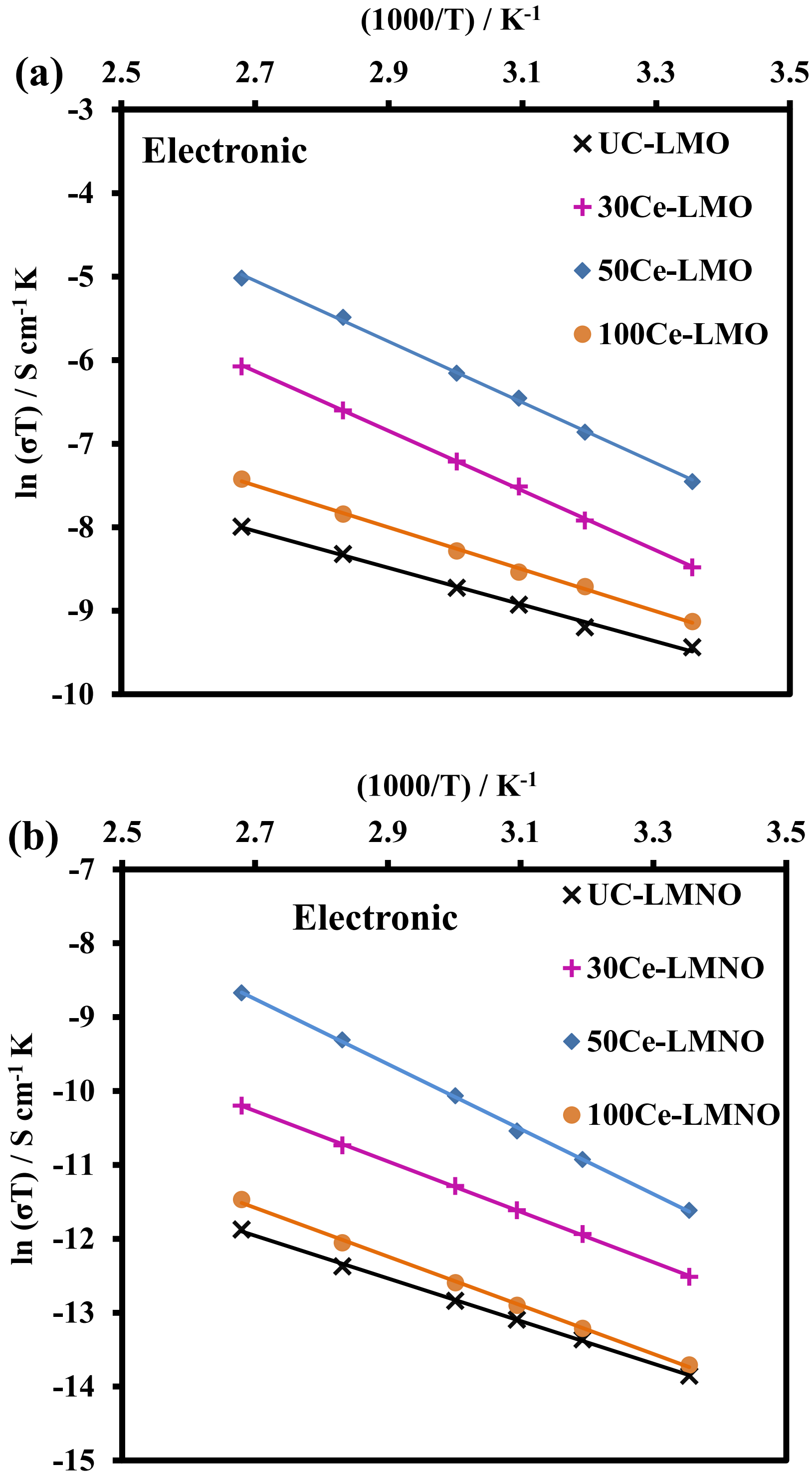

Fig. 3. Arrhenius plots for the effects of temperature on electronic conductivity of uncoated and CeO_2 coated (a) $LiMn_2O_4$ and (b) $LiMn_{1.5}Ni_{0.5}O_4$ particles.

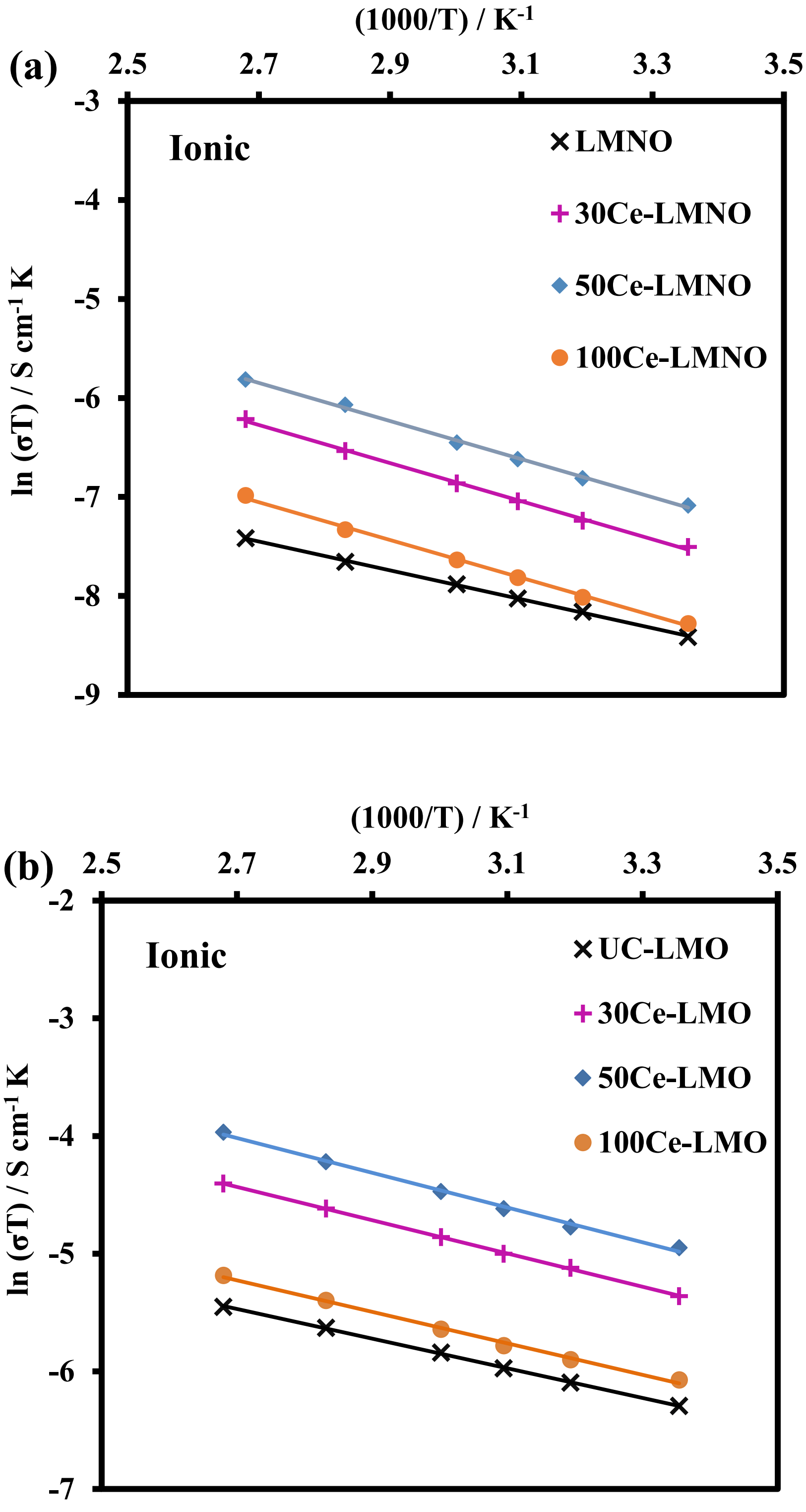

Fig. 4. Arrhenius plots for the effects of temperature on ionic conductivity of uncoated and CeO_2 coated (a) $LiMn_2O_4$ and (b) $LiMn_{1.5}Ni_{0.5}O_4$ particles.

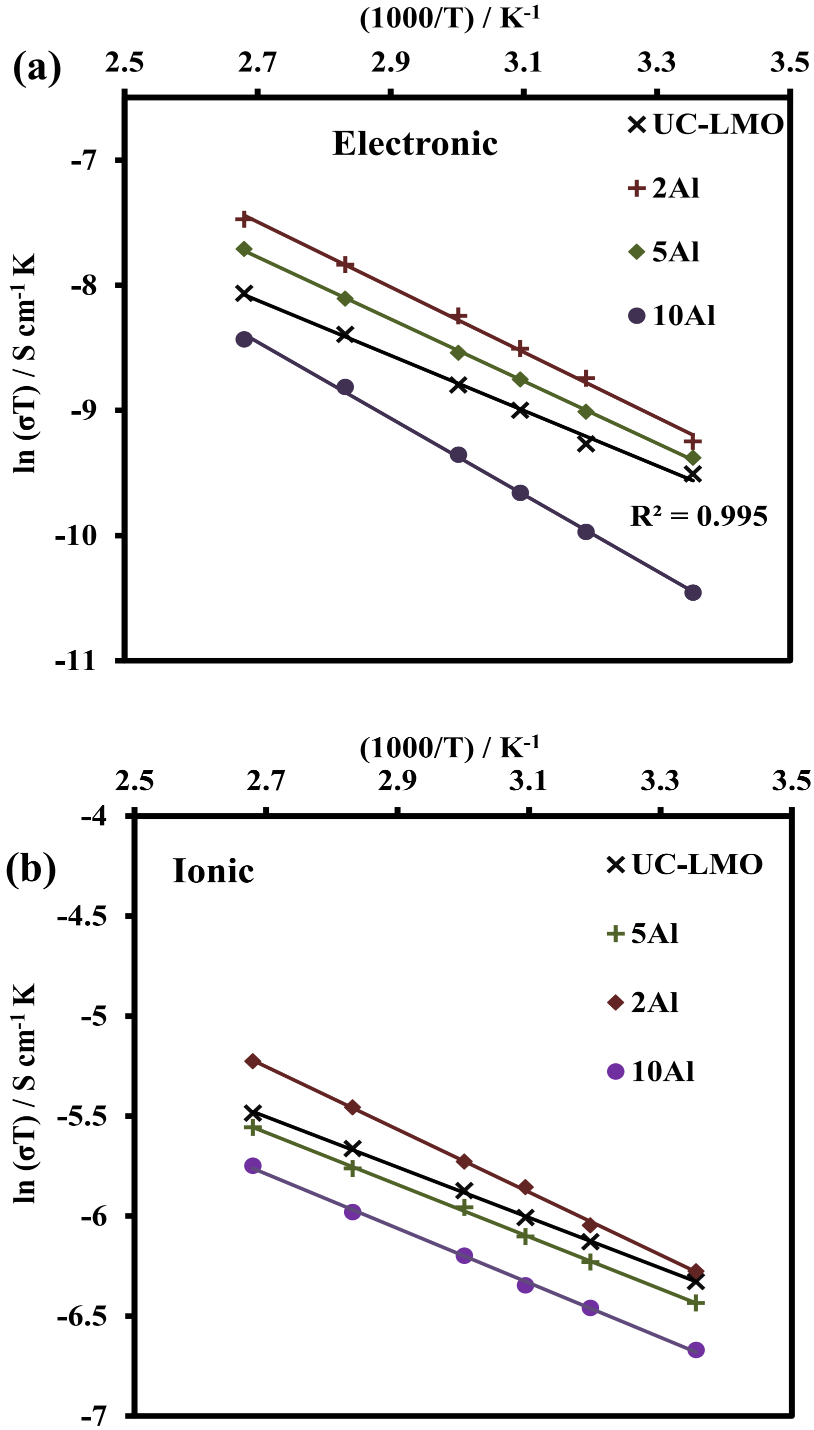

Fig. 5. Arrhenius plots for the effects of temperature on electronic and ionic conductivity of (a,b) Al_2O_3 and (c,d) ZrO_2 coated $LiMn_2O_4$ particles.

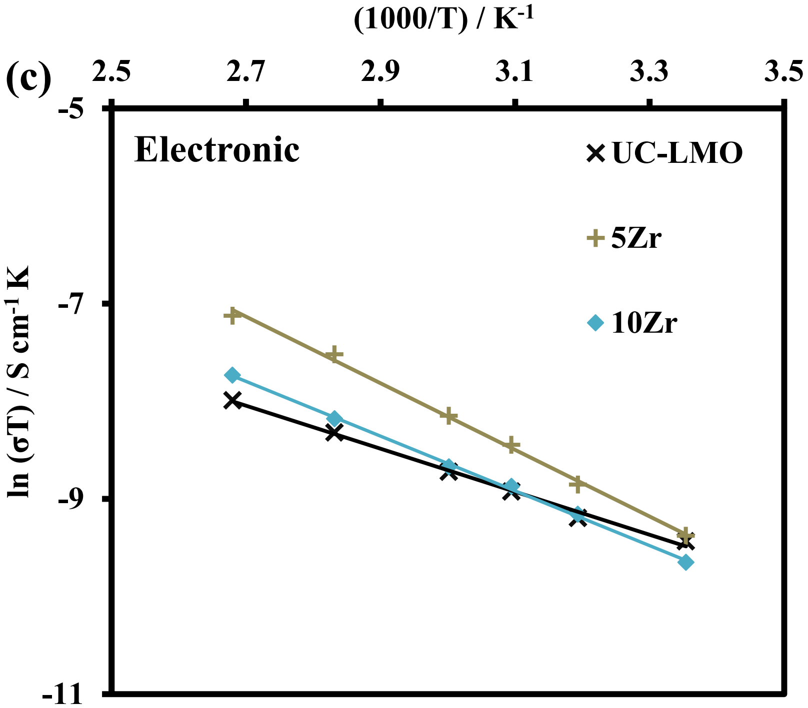

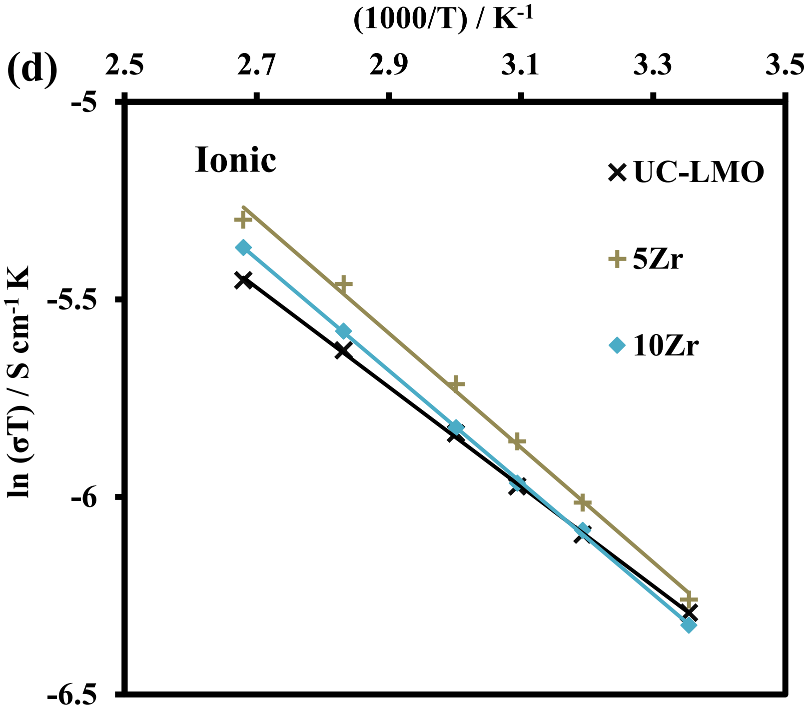

Fig. 5. Arrhenius plots for the effects of temperature on electronic and ionic conductivity of (a, b) Al_2O_3 and (c, d) ZrO_2 coated $LiMn_2O_4$ particles. (Cont.)

Table 1. Fitted parameters for the Nyquist plots using electrical equivalent circuit shown in Fig. 2.

	Temperature	**UC LMO**	**30Ce LMO**	**50Ce LMO**	**100Ce LMO**	**UC LMNO**	**30Ce LMNO**	**50Ce LMNO**	**100Ce LMNO**
R1 (Ω)	**25°C**	371178	152778	54773	292717	2845735	801511	325567	2634675
	40°C	306829	91634	31805	202140	1827267	471888	171682	1685498
	50°C	241974	62940	21846	175251	1447267	352034	120456	1273403
	60°C	203761	48137	16708	140311	1155749	262006	77235	967369
	80°C	144173	27648	9073	95528	767927	159942	38421	597060
	100°C	109784	17279	5997	66485	492394	98744	21472	351612
R2 (Ω)	**25°C**	17382.9	7322.9	4853.4	14916.8	14086.6	6076.8	4002.0	13148.1
	40°C	14977.6	6050.8	3988.8	12325.5	11453.8	4896.9	3193.2	10595.2
	50°C	13685.1	5541.6	3524.9	11288.2	10359.9	4153.1	2717.2	8985.8
	60°C	12340.4	4963.0	3143.2	10109.6	9243.1	3574.8	2367.6	7734.6
	80°C	10601.4	4121.2	2586.8	8394.9	7807.1	2733.5	1714.6	6043.1
	100°C	9378.9	3524.4	2125.2	7179.2	6507.1	2089.3	1403.7	4520.6
CPE (µF)	**25°C**	0.00025	0.00075	0.00056	0.00107	0.00212	0.00622	0.00465	0.00891
	40°C	0.00024	0.00086	0.00045	0.00088	0.00203	0.00714	0.00377	0.00736
	50°C	0.00014	0.00065	0.00063	0.00063	0.00117	0.00541	0.00522	0.00524
	60°C	0.00013	0.00063	0.00059	0.00062	0.00110	0.00522	0.00488	0.00518
	80°C	0.00021	0.00096	0.00107	0.00074	0.00179	0.00802	0.00892	0.00617
	100°C	0.00036	0.00163	0.00059	0.00082	0.00300	0.01360	0.00492	0.00687
P	**25°C**	0.086	0.084	0.087	0.084	0.717	0.696	0.7238	0.701
	40°C	0.088	0.085	0.088	0.084	0.733	0.707	0.7317	0.696
	50°C	0.092	0.088	0.090	0.088	0.764	0.734	0.752	0.731
	60°C	0.093	0.090	0.092	0.089	0.774	0.747	0.769	0.741
	80°C	0.088	0.088	0.088	0.088	0.734	0.735	0.7367	0.735
	100°C	0.085	0.088	0.092	0.088	0.71	0.733	0.767	0.737

Table 2. DC resistance measurements of CeO_2-coated and uncoated $LiMn_2O_4$ and $LiMn_{1.5}Ni_{0.5}O_4$ samples at different temperature.

	Temperature	**UC LMO**	**30Ce LMO**	**50Ce LMO**	**100Ce LMO**	**UC LMNO**	**30Ce LMNO**	**50Ce LMNO**	**100Ce LMNO**
DC resistance (Ω)	**25°C**	390714	160819	57656	308123	3011360	848159	344516	2788016
	40°C	322977	96457	33479	212779	1933616	499352	181674	1783596
	50°C	254710	66252	22996	184474	1531499	372522	127467	1347517
	60°C	214485	50670	17587	147696	1223014	277255	81730	1023671
	80°C	151761	29104	9551	100556	812621	169251	40657	631809
	100°C	115562	18189	6313	69984	521052	104491	22722	372076

Table 3. DC resistance measurements of uncoated and Al_2O_3 and ZrO_2 coated $LiMn_2O_4$ samples at different temperature

	Temperature	**UC LMO**	**2Al**	**5Al**	**10Al**	**5Zr**	**10Zr**
DC resistance (Ω)	**25°C**	56597	220590	336483	982459	461535	275881
	40°C	46785	139929	216171	634912	276822	160198
	50°C	36896	113885	160326	479680	190138	110033
	60°C	31070	90446	125939	364399	145418	84154
	80°C	21984	63640	84276	224907	83524	45699
	100°C	16740	46806	59245	162449	52199	30208

V. Employing Synergetic Effect of Doping and Thin Film Coating to Boost the Performance of Lithium-Ion Battery Cathode Particles

Rajankumar L. Patel[1], Ying-Bing Jiang[2], Amitava Choudhury[3] & Xinhua Liang[1,*]

[1] Department of Chemical and Biochemical Engineering, Missouri University of Science and
Technology, Rolla, Missouri 65409, United States

[2] TEM Laboratory, University of New Mexico, Albuquerque, New Mexico 87131,
United States

[3] Department of Chemistry, Missouri University of Science and Technology, Rolla,
Missouri 65409, United States

* Email: liangxin@mst.edu

ABSTRACT

Atomic layer deposition (ALD) has evolved as an important technique to coat conformal protective thin films on cathode and anode particles of lithium ion batteries to enhance their electrochemical performance. Coating a conformal, conductive and optimal ultrathin film on cathode particles has significantly increased the capacity retention and cycle life as demonstrated in our previous work. In this work, we have unearthed the synergetic effect of electrochemically active iron oxide films coating and partial doping of iron on $LiMn_{1.5}Ni_{0.5}O_4$ (LMNO) particles. The ionic Fe penetrates into the lattice structure of LMNO during the ALD process. After the structural defects are saturated, the iron starts participating in formation of ultrathin oxide films on LMNO particle surface. Owing to the conductive nature of iron oxide films, with an optimal film thickness of ~0.6 nm, the initial capacity improved by ~25% at room

temperature and by ~26% at an elevated temperature of 55°C at a 1C cycling rate. The synergy of doping of LMNO with iron combined with the conductive and protective nature of the optimal iron oxide film leads to a high capacity retention (~93% at room temperature and ~91% at 55°C) even after 1,000 cycles at a 1C cycling rate.

Introduction

$LiMn_{1.5}Ni_{0.5}O_4$ (LMNO) has received much attention as alternate cathode materials for lithium ion batteries (LIBs) due to its improved cycling behavior relative to the pristine spinel[1]. The operating voltage window of LMNO makes it a potential candidate for use in hybrid electric vehicles (HEV) due to its nominal cost, enhanced thermal stability and enhanced rate capability owing to its three-dimensional structure[2-5]. However, it has not gained commercial usability in HEV due to high capacity fade during cycling at elevated temperatures and Mn^{3+} dissolution by HF[6,7]. Doping LMNO with ions has been considered to be an effective way to better the core properties of LMNO for enhanced electrochemical performance. In a typical cycling curve of $LiNi_{0.5-x}Fe_xMn_{1.5}O_4$, the oxidation-reduction pairs, Fe^{IV}/Fe^{III}, Ni^{IV}/Ni^{II}, and Mn^{IV}/Mn^{III}, corresponds to the three stages of addition or subtraction of electrons in and out of the d-spacing of the compounds[8]. Liu et al.[9] reported that Fe doping could subdue the solid electrolyte interface (SEI) formation by enabling certain surface enhancements, which is very important to improve the electrochemical performances of the 5 V spinel cathode materials. Doping alone cannot, however, significantly improve the cycleability and capacity retention of LMNO as it cannot avoid dissolution of Mn^{3+} ions by HF[10]. One approach to solve this problem is to form a protective film around the LMNO structure, thereby significantly reducing Mn^{3+} dissolution and improving capacity retention and cycling performance.

Several researchers have used wet chemical methods including sol-gel methods to coat protective film over pristine LMNO[11,12]. The protective coating improved cycling life and capacity retention of LMNO. However, there was always a bargain between increasing the capacity and longer cycle life of the battery. In these studies, it was difficult to precisely control the thickness of the coating, and the films were not conformally coated on the particle surfaces. The increased thickness causes increased mass transfer resistance that delays the movement of species, electrons, and ions. Hence, an optimal thickness of the film is crucial for the best performance enhancement. This can be achieved by atomic layer deposition (ALD).

ALD is best known for its ability to deposit high-quality, ultra-thin conformal films of materials based on alternating dosing of chemical vapors that react with surfaces[13-16]. ALD ensures control of film thickness at nanometer level. However, if the ALD film is insulating, such trade-off still exists[14], which has also been demonstrated in our recent work and an effective solution was proposed[17]. It has been demonstrated that coating an optimal thickness of conductive metal oxide films could improve both specific capacity and cycling performance. In our recent work[17], ultrathin 3 nm ALD CeO_2 film was coated on $LiMn_2O_4$ particles that showed 24% improvement in specific capacity, compared to the uncoated one, and high capacity retention of 96% at room temperature and 95% at an elevated temperature of 55 °C even after 1,000 cycles at a 1C rate. Herein, we propose that iron oxide would be an excellent candidate as the coating layer due to its electrochemical activity, low cost, environmental benignity, and natural abundance. The conductive nature of iron oxide coating using sputtering or liquid phase method has improved electrochemical performance of carbon nanotubes[18] and SnO_2 particles[19], but the results were restricted to small number of cycles and the coatings were not optimal to make it a viable solution. Conformal iron oxide films with controlled thickness can be coated by ALD. Due to the relative high temperature of iron oxide ALD coating process and the surface defects of LMNO, we expected that Fe could also be doped in the crystal strucutre of LMNO.

To the best of our knowledge, there has been no successful study, so far, exploring the synergetic effect of iron doping and ultra-thin film coating of iron oxide using ALD on LIB electrode particles. In this study, large quantities of LMNO particles were coated with ultra-thin iron oxide films by ALD in a fluidized bed reactor. The ALD coated samples demonstrated both longer cycle life with improved stable performance for more than 1,000 cycles of electrochemical cycling at room temperature and at 55 °C. We also report the first time a unique phenomenon of ionic Fe entering the lattice structure of LMNO during the ALD coating process. We believe the combined effect of the doping of Fe into the structure of LMNO and the conductive optimal ultrathin coating of iron oxide films has significantly enhanced cycleability and reduced capacity fade of LMNO.

Results and Discussion

Iron oxide films coated on $LiMn_{1.5}Ni_{0.5}O_4$ particles

Different numbers of iron oxide ALD coating cycles were applied on the surfaces of LMNO particles (4-5 μm, NANOMYTE® SP-10, NEI Corporation). ALD reaction was carried out for 10 (10Fe), 20 (20Fe), 25 (25Fe), 30 (30Fe), 40 (40Fe), 80 (80Fe), and 160 (160Fe) cycles. The transmission electron microscopy (TEM) image of an uncoated (UC) LMNO particle (shown in Figure 1a) displays a blank edge of a pristine particle. In contrast, a distinctive conformal coating of ~3 nm layer on a LMNO particle after 160 cycles of iron oxide ALD, is seen in Figure 1b. Figures S1a – d (see supporting information) show images at different magnification level for one particle. It is clear from the series of images that the iron oxide coating was conformal and covering the entire particle surface. Based on this 160Fe sample, the growth rate of iron oxide films on the LMNO particles was ~0.02 nm/cycle. The iron oxide growth rate is in sync with the previously reported values[20]. The growth rate value is derived from TEM images only and it does not represent the actual number of layers since ALD process experiences nucleation period at the beginning of the cycles. The Figures S2a and S2b (see supporting information) show the selective area electron diffraction (SAED) pattern of those two samples. Both powders exhibited well-developed octahedral shapes, although a secondary phase appeared to grow on the corner of the octahedral particle after coating 160 cycles of iron oxide ALD, as indicated in Figure S2b. In order to confirm the diffusion and distribution of iron inside the particle structure, about 80 nm thick thin section across the center of the 160Fe sample particle was cut using focused-ion beam (FIB) and elemental mapping was performed using energy dispersive x-ray spectroscopy (EDS). Figure 1c is the regular TEM image of the thin-section across the center of a particle. Figure 1d is the Fe elemental map of the same particle as shown in Figure 1c, acquired in the scanning TEM (STEM) mode combined with EDS collection. Figure 1e is the Fe element distribution along the red line as shown in Figure 1c, and EDS line scan in the STEM mode was used to acquire this information. It clearly shows the Fe penetration ~400 nm deep below the 160Fe LMNO particle surface. The EDS spectrum from the surface vicinity of the UC and the 160Fe samples are shown in Figure S3. It is evident from those spectra that there was no Fe in the UC sample, while there was a large amount of Fe on the particle surface of the 160Fe sample. This study in addition to the

TEM images (as in Figure 1b) provides evidence needed to support the claim that the doping and coating both occurred during the ALD coating process. This unique phenomenon has never been reported during ALD coating process.

The Fe content on the LMNO particles was measured using inductively coupled plasma atomic emission spectroscopy (ICP-AES). As shown in Figure S4 in supporting information, iron content increased almost linearly with increase in the number of ALD cycles. The thicknesses of iron oxide films were reflected by the content of Fe on the particles. The iron oxide film thickness was several magnitudes smaller than the 4-5 micron sized cathode particles. The plot trend clearly indicated a linear growth rate of iron oxide ALD films onto the particles surface except for the short initial period for the first 10 ALD cycles. The surface area of the UC samples was 1.8 m^2/g measured by using Quantachrome Autosorb-1. Based on the surface area of particles, percentage of Fe in the 160Fe sample obtained from ICP-AES, and assuming the oxide films being Fe_3O_4, the expected thickness of the ultrathin film was found to be ~10 nm. However, the TEM analysis showed the film thickness to be only 3 nm. This discrepancy also indirectly supported that Fe had entered the lattice structure of LMNO.

Figure 2 shows the powder X-ray diffraction (PXRD) pattern of the UC, 10Fe, 30Fe, 80Fe, and 160Fe samples. The PXRD patterns of pristine and modified samples confirm the existence of cubic spinel structure. All the main diffraction peaks are sharp, which indicates that the tested samples are well-crystallized. The pattern for the UC differs significantly from the 160Fe sample. For the 160Fe sample, the main peaks are not so sharp and some of the peaks have a significant shift in their position, indicating the significant amount of Fe substituted into the LMNO structure. The weak reflections observed at around 18.2º, 30º, and 57.5º in the 160Fe sample are absent in the 10Fe sample and only 30º peak in 30Fe and 80Fe. The presence of Fe_3O_4 was confirmed for the case of 160Fe by the additional peaks at 30º and 57.5º, which are consistent with the reported results[21-23]. The PXRD patterns, consistent with the SAED pattern, indicate that the iron oxide ALD coated LMNO does not have the same phase as its uncoated counterpart. X-ray photoelectron spectroscopy (XPS) results further confirmed the presence of Fe_3O_4 phase in the 160Fe sample (see Figure S5 in supporting information). For the 30Fe and 40Fe samples, the Fe content was much lower than that of the 160Fe sample, and PXRD showed very weak peaks to indicate the presence of Fe. Iron content in 10Fe was too low to detect any particular iron oxide phase confidently. This all could be explained with the fact that the ALD deposition of iron oxide using ferrocene and oxygen precursor at high temperature (in this case 450 °C) resulted in formation of Fe_3O_4 as evidence from the PXRD[24,25], which could be pure Fe_3O_4 spinel with $\mathrm{Fe_{tet}^{3+}[Fe^{2+}Fe^{3+}]_{oct}O_4}$ (magnetite) composition, a defect non-stoichiometric spinel, $Fe_{3-x}O_4$ or γ-Fe_2O_3 (maghemite). γ-Fe_2O_3 is the end member of non-stoichiometric $Fe_{3-x}O_4$, given as $\mathrm{Fe_{tet}^{3+}[Fe_{5/3}^{3+}\square_{1/3}]_{oct}O_4}$ [$\square$ represents vacant site][26]. Unfortunately, PXRD of these phases have subtle differences, which make it difficult to distinguish between them especially when the amount of Fe-content is less and particle sizes are small. To get a better insight into the nature of Fe_3O_4 phase, we carried out Mössbauer spectroscopy of the 160Fe sample, since this sample had substantial amount of Fe for reliable Mössbauer signal. The room temperature (25 °C) Mössbauer spectrum of 160Fe of broad sextet indicates hyperfine magnetic component together with a central quadrupolar doublet (Figure S6 in supporting information). The broadness of resonance lines in sextet is indication of small particle size and a distribution of hyperfine magnetic fields. The isomer shift (δ), quadrupolar splittings (Q.S.) and hyperfine field (B_{hf}) of the sextet are 0.32(5) mm/s, 0.016(6) mm/s, and 44.6(5)T, respectively, consistent with γ-Fe_2O_3 and rules of possibility of octahedral Fe^{2+} as in spinel Fe_3O_4, which produces another sextet subspectra with high δ value (~0.63 mm/s)[27]. The δ and Q.S. for the quadrupolar splitting for the central doublet are 0.36 and 0.74 mm/s, respectively. The δ and Q.S. values for the central doublet are characteristic of Fe^{3+} ions in octahedral coordination[28], which may arise from the doping of Fe^{3+} in LMNO phase as hypothesized based on the TEM studies and shifting of PXRD lines of coated LMNO with respect to pristine sample. However, there is a note of caution here; such central doublet can also arise due to the presence of superparamagnetic iron-oxide particles. In summary, the results from PXRD, TEM-SAED, STEM-EDS, and XPS strongly suggest that during the ALD coating process, some amount of Fe doping occurred (in some valance state Fe penetrated into the lattice structure of LMNO) and Fe_3O_4 ultra-thin film formed. With increment in iron oxide ALD cycles, Fe_3O_4 can be further oxidized to provide γ-Fe_2O_3 [29], as here in the case of 160Fe.

Electrochemical testing

The charge-discharge analysis was carried out in a 3.5 V – 5 V voltage range. Figures 3a and 3c show the discharge capacities of the UC, 10Fe, 20Fe, 25Fe, 30Fe, 40Fe and 80Fe samples that were discharged at different C rates, of 0.1C, 0.2C, 0.5C, 1C, and 2C, for five cycles at room temperature and 55 ºC, respectively. For these conditions, almost all of the iron oxide ALD coated samples showed higher initial discharge capacity than the UC. The increased discharge capacity of iron oxide coated samples can be attributed to synergetic effect between doped Fe and conductive iron oxide overlayer. In Figure 3b, the normalized discharge capacities obtained at various C rates are plotted for all samples in reference to capacity obtained at 0.1 C. The results clearly demonstrate that the 30Fe sample showed superior rate capability as compared to other samples at room temperature. At a 2C rate where charge/ discharge cycle was about 30 min, the 80Fe sample performed poor due to the increased mass transfer resistance caused by the thicker coating. At 55 °C, in Figure 3d, a similar trend is observed. Overall the 30Fe sample performed better than any other coated or uncoated samples. At a 2C rate, the 80 Fe sample performed much poorer as compared to room temperature testing due to degradation of cell performance at high temperature. The diffusional and kinetic overpotential, solid electrolyte interphase (SEI) layer induced resistance, and contact/ohmic resistance are the main cause of the voltage drop in a typical LIB. The ultrathin iron oxide ALD film can significantly alter the most of these causes of the voltage drops. However, if the Li concentration ratio between the particle surface and the bulk is not affected by the coating, then the overpotential caused by the diffusional forces remains unchanged. The layer formed on the cathode surface (known as solid permeable interface) is usually much thinner than the SEI layer formed on the anode surface, and its thickness increases with charge-dischare cycling and the temperature[30].

Figure 4a shows the results of discharge cycling at a 1C rate between 3.5 V – 5 V for the UC, 10Fe, 20Fe, 25Fe, 30Fe, 40Fe, and 80Fe cells at room temperature up to 1,000 cycles. The discharge capacity of the UC was initially 114 mAh/g, and it declined to 80 mAh/g after 1,000 cycles. In contrast, the 30Fe and 40Fe samples exhibited much higher initial discharge capacities than the UC. The 30Fe showed a remarkable initial discharge capacity of 143 mAh/g, which is ~25% increment compared to the UC. The differance between 30Fe and 40Fe became much less with increase in cycle numbers. The stable discharge capacity at ~133 mAh/g was maintained (which is ~19 mAh/g higher than the UC cell's initial capacity) for the case of 30Fe even after 1,000 cycles, which means that it dropped only by less than 7 %, compared to its initial capacity. Similarly, 40Fe showed remarkable ~95% capacity retention after 1,000 cycles at room temperature. This is the only time when 40Fe showed better results than 30Fe. The reason is not apparent, but it could be argued that the structural similarity of the iron oxide film and perhaps the amount of doped Fe are the reason that 30Fe and 40Fe showed very comparable results throughout this study. In addition, as seen in Figure 4b, the ALD coated LMNO showed significantly improved cycling performance, even at an increased testing temperature of 55 ºC. The 30Fe and 40Fe cells exhibited an initial discharge capacity of ~140 mAh/g. After 1,000 cycles, the capacity of 30Fe was stabilized at around 125 mAh/g after a gradual decrease from its initial capacity. The 30Fe and 40Fe samples showed much higher capacity than the UC sample, which indicated that iron oxide coated LMNO particles was much more chemically and thermally stable. The 10Fe sample showed higher initial capacity than the 20Fe and 25Fe, which is in sync with the different C rate results. However, in a long run, it declined very significantly. This could be explained by the same reason that the Fe doped into the structure of the LMNO helped improve the initial capacity of the material and the iron oxide coating which occured after more ALD cycles (as in 20Fe and 25Fe) gave stability to the material. The 80Fe sample showed poor stability over the testing time of 1,000 charge-discharge cycles. The reason could be that it has relatively thicker coating than other coated samples. The thick film induces more stresses during lithium ion insertion and deinsertion. These increased stresses combined with more mass transfer resistance of Li^+ due to the relatively thick films as compared to 30Fe/40Fe lead to poorer performance of the 80Fe sample. With increase in charge-discharge cycling, less Li^+ inserted into cathode due to the increasing thickness of the SEI layer on lithium. This explains the worst performance of the 80Fe sample.

As learned from our previous work[17], the drawback of coating on particles is slower species transport. Consequently, a demonstration of performance improvement via ALD coatings at a high C rate is significant because the diffusivity of ions in the solid phase becomes significant as the input current increases. Also, the inside temperature of a cell increases with faster charge-discharge cycle rate, and that also increases the stress level due to developed concentration gradient inside particles. There is also a possibility of phase transition at the particle surface from overlithiation during this cycling process. So, in order to examine the perfomance of these coated samples, they were cycled at a 2C rate, shown in Figure 5. The performance of 10Fe improved slightly due to initial iron doping. The trend is similar to the test at a 1C rate as disscussed earlier and the higher initial capacity of 10Fe did not last longer than the 20Fe and 25Fe coated samples. A conformal coating of iron oxide with a larger number of ALD coating cycles provided a protection, which resulted in a significant improvement in initial capacity fade and remarkable stable performance, as in the case of 30Fe. The 30Fe and 40Fe samples still had far better discharge capacity and stability than the UC sample, even after 1,000 cycles at a 2C rate at both room temperature and 55 ºC. The 30Ce and 40Fe samples showed more than 90% capacity retention after 1,000 cycles, while the UC sample could not withstand the high rate of charge-discharge cycling and the capacity kept dropping. Overall, the 30Fe cells showed consistentantly better than any other prepared cells. The excellent cycling behavior of the iron oxide ALD-coated LMNO electrodes, compared to the UC cell, clearly indicates that the synergetic effect of ALD deposited iron oxide coating and Fe doping into the LMNO structure (see STEM-EDS and TEM-FIB results) could well be the reason for the significantly improved electrochemical performances even at high C rates and high temperature cycling.

The interface change due to ALD thin film coating was further investigated using electrochemical impedance spectroscopy (EIS). A three electrode configuration was used for the EIS measurements. The cathode in the coin cell served as the working electrode, whereas Li metal anode served as both the reference and the counter electrode. All the impedance measurements were performed at open circuit voltage. The impedance spectra were fitted using equivalent circuit that consisted of three resistance elements, two constant phase elements and a warburg diffusion element (see Figure 6c). The details about the fitted parameters are explained elsewhere[17]. Among the fitted parameters, ohmic resistance (R_{ohm}), charge-transfer resistance (R_{ct}), and surface film resistance (R_f) can be used to quantify the polarization behaviors. The W1 element represents the warburg impedance, which can be used to quantify Li-ion mass transfer resistance. Table 1 provides the list of all the fitted parameters value obtained after fitting the impedance curves to an equivalent circuit . The semicircle from the impedance analysis of all the cells was fitted using a combination of two R|C units (resistor|capacitor) to represent surface-film and charge-transfer resistance, $R_{(f+ct)}$. For clarification, the lines in resultant impedance curves were not obtained after fitting the equivalent circuit to the impedance curves. One semicircle was observed for the UC and the iron oxide ALD coated cells, as shown in Figure 6. Upon a close look at the semicircle, it reveals that they in fact are two semicircles overlapped, which could be contributed from the SEI film (at higher frequency region) and the charge-transfer resistance at the particle surface (at mid to high frequency regions)[9,14]. After the 1st and 1,000th charge-discharge cycles, the radius of the semicircles of the 30Fe and 40Fe cells are smaller in comparison to the UC cell, as evident in Figure 6a and 6b. With the increase in the thickness of iron oxide ALD films, the radius of the semicircle increased, as in the case of 80Fe, which was mainly due to the increased charge-transfer resistance (see Table 1), indicating that the sluggish transit of Li through the longer pathway. After 1,000 charge-discharge cycles, the warburg resistance (the element that is representative of Li^+ ion diffusion resistance) was the highest for the UC sample as compared to the coated samples. The charge transfer resistance first decreased with increase in the number of ALD coating cycles, reached a minimal value for the 30Fe sample and then increased with the increase in number of ALD coating cycles. This trend is indicative that 30Fe sample has the optimal thick coating as comapred to the other samples. The film resistance also followed a similar trend as the ultrathin film is conductive.

EIS study was also performed at high temperature (55 ºC), as shown in Figure 7. The UC sample experienced much more increment in charge transfer resistance than the iron oxide ALD coated samples except for the 80Fe sample. The higher impedance of the UC sample at an elevated temperature has been attributed to the degradation reactions between the cathode and the electrolyte[3]. As discussed above, the 80Fe sample exprienced large stresses coupled with high mass transfer resistance due to the relatively thick coating. That could be due to high charge transfer resistance from the distorted lattice structure. Comparing the impedance parameters of the 30Fe and 40Fe cells with the UC cell, it is clear that the UC cell was experiencing slower kinetics after cycling. The 30Fe cell showed the best results among all the other cells tested. With increase in charge-discharge cycling, the charge-transfer and the film resistance increased, and the difference between the UC cell and the coated cells grew significantly. For example, after 1,000 charge-discharge cycles, the combined film and charge transfer resistance of the 30Fe was 173.9 Ω, while it was 300.5 Ω for the UC cell, which was greatly increased from the value of the fresh cell. The resistance values explain that the kinetics of the surface film developed on the electrodes[31,32]. R_{ohm} values for the UC sample and the other samples are not the same. The change could be due to the structure modification of LMNO by iron doping and iron oxide coating. The 30Fe sample performs the best as compared to the other samples. This is because of the lowest charge transfer and film resistance of the 30Fe sample. For the 20Fe sample, the film was just not thick enough to provide good protection as compared to the optimal coating of 30Fe. Lower charge tranfer and film resistance could also mean that more Li^+ ions are available at the 30Fe cathode surface, thereby compensating for increased diffusion resistance. The lower film resistance is due to the conductive iron oxide film coating. The trend of the charge transfer and the film impedance values confirm that the 30Fe sample has the optimal ultrathin coating of iron oxide.

Pellets of only the UC, 20Fe, 30Fe, 40Fe, 80Fe, and 160Fe particles were prepared for conductivity measurements. The ac complex plane impedance analysis was used for the experiement[33,34] and the same impedance analyzer was used to obtain the impdance curves. This experimental procedure was similar to the conductivity experiments carried out in our recent study[17]. The fitting of those curves were also perfomed and equivalent circuits were obtained. The equivalent circuit used to fit the impedance curves is shown in Figure

8b. The equivalent circuit does not contain the warburg element as there is no conduction or movement of ions during this experiment. The obtained film resistance (R_f) and charge transfer resistance (R_{ct}) are combined in series to obatin an equivalent resistance value, which is used for conductivity calculations. For measuring the resistivity, the pellet thickness and diameter is found from which the area is calculated. This procedure helps us to calculate only the mixed ionic and electronic conductivites. Our work on the seperation of these coductivities including the detailed methods and analysis will be illustrated in a future publication. Comparing the results among the uncoated and the coated samples (Figure 8), which were prepared using the same procedure and material compositions, it is certain to conclude that iron oxide coating can improve the conductivity of the LMNO particles. The 160Fe sample shows the best conductivity compared to any other samples, which could also be true due to the presence of highly conductive Fe_3O_4 (or γ-Fe_2O_3). This is in contrast to our previous work[17], where the highest conductivity was achieved with an optimum CeO_2 thickness of 3 nm. In this case, the iron oxide ALD film growth rate was very low (the thickness of 160 cycles of iron oxide ALD is only 3 nm) and, hence it is thin enough to provide better conductivity for the coated samples with higher number of ALD cycles. The conductivity has been found to obey the Arrhenius equation[33,34],

$$\sigma \cdot \mathrm{T} = \sigma_0 \cdot \exp\left(\frac{-\mathrm{E_a}}{\mathrm{k_B T}}\right) \qquad (1)$$

where, σ_0 is the pre-exponential factor, k_B is the Boltzmann contant, T is absolute temperature, and E_a is the activation energy for Li ion movement. Figure 8 shows the direct co-relation between the mixed conductivity and the temperature (a linear Arrhenius plot). Since the testing temperature were limited to 328 K, there was no phase or structural change observed during the measurements.

Conclusions

In summary, we have sucessfully demonstarted that the cycle life and the capacity retention of LMNO can be significantly improved by the synergetic effect of ultrathin film coating of iron oxide combined with Fe ionic doping in the lattice structure LMNO particles. The ionic Fe penetration into the lattice structure of LMNO was verified by cross-sectional STEM-EDS of iron oxide coated samples and the ultra-thin iron oxide films were directly observed by TEM. Mössbauer and XPS results confirmed the valance state of the iron for the ALD coated samples. It can be seen that the 30Fe sample has a high initial capacity of 143 mAh/g, which is about 25% higher than that of the UC sample at a 1C rate. It shows 93 % capacity retention after 1,000 cycles at room temperature. More importantly, at elevated temperatures, the 30Fe sample performs the best as compared to the UC sample and other iron oxide coated samples. This work reports the first time the synergetic effect of doping and thin film coating on LMNO particles. ALD coating of iron oxide provided much better improvement in performance of LMNO than what could potentially be due to only doping effect. ALD has the potential to prepare these ultrathin electrochemically active films with optimal thickness and synergetic effect of conductive coating and element doping, providing the industry to design novel electrodes that are durable as well as functional at high temperature and fast cycling rates. Further in depth analysis of this unique technique could provide major breakthrough to solve the current shortcoming in the field of energy storage.

Methods

ALD coating

The ALD coating was carried out in a fluidized bed reactor, described elsewhere in detail[35]. There was a filter employed to contain the particles in the reactor, while allowing only gas to pass. Ferrocene (99% pure, Alfa Aesar) and oxygen (99.9%, Airgas) were used as precursors, and were delivered into the reactor in alternate doses at 450 ºC. Ferrocene was delivered into the reactor using a heated bubbler and nitrogen was used as a carrier gas. Then N_2 was used to purge the reactor to remove any unreacted ferrocene and by-products. After that, O_2 was fed into the reactor, followed by another N_2 purge. All lines were heated to 120 ºC to avert any vapor deposition inside the lines.

Materials characterization

The iron oxide films was verified using a FEI Tecnai F20 field emission gun high resolution TEM equipped with EDS system. ICP-AES was used to quantify the mass percent of iron on the particles. To check the Fe element distribution within the particles, about 80 nm thick thin section across the center of the particle was prepared by focused ion beam, using an FEI Q3D dual-beam system. The thin section was subsequently checked by a JEOL 2010F TEM in both TEM mode and scanning TEM mode at 200kV acceleration voltage. The crystal structure of the uncoated and coated particles was determined via powder XRD (Phillips Powder Diffractometer, CuKα radiation, λ = 1.5406 Å). The PXRD analysis was performed using a scan rate of 2º/min and a step size of 0.2º.

^{57}Fe Mössbauer spectroscopy was performed on the as-prepared, chemically oxidized, and different state-of-charge cathode materials in transmission geometry using a constant acceleration spectrometer equipped with a ^{57}Co (25 mCi) gamma source embedded in Rh matrix. The instrument was calibrated for velocity and isomer shifts with respect to α-Fe foil at room temperature. The resulting Mössbauer data were analyzed using Lorentzian profile fitting by RECOIL software[36].

Coin cell assembly

An 80:10:10 wt.% mixture of $LiMn_{1.5}Ni_{0.5}O_4$, carbon black (super P conductive, 99+%, Alfa Aesar) and polymer binder poly(vinylidene fluoride) (Alfa Aesar) was used to prepare cathodes. The slurry of the mixture was spread on the Al-foil, and then it was dry-heated at 120 ºC. The cathode discs/working electrodes were made after the coated foil was punched. The reference/counter electrode was Li metal (99.9% trace metal basis, Sigma-Aldrich) and $LiPF_6$ (1 mol/L in a mixed solvent of ethylene carbonate, dimethyl carbonate, and diethyl carbonate with a volume ratio of 1:1:1, MTI Corporation) in all the cells prepared. The CR2032 cells fabrication was carried out in an Ar-filled glove box.

Electrochemical analysis

The charge-discharge analysis was carried out using an 8-channel battery analyzer (Neware Corporation) for 3.5 – 5 V potential range at various C rates, and at different temperatures (room temperature and 55 ºC). The electrochemical impedance spectroscopy of the prepared cells were carried out using an IviumStat impedance analyzer. The EIS analysis was performed at 5 mV and 0.01 – 1M Hz frequency range. Conductivity measurements were carried out using the same analyzer for cold pressed pellets of the samples. The pellets were coated with Ag (paste from Sigma Aldrich) on both sides to act as the blocking electrodes. These pellets were vacuum-dried at ~85 ºC for 6 hr. The analysis were performed for a range of 1 Hz to 1 MHz and at 1 mV. The test temperature range was

20 – 55 ºC. The spectra were analyzed using Zview software (Scribner Associates, Inc.). The conductivity tests were performed to compare the coated and uncoated samples and to examine the conductive nature of the coating with respect to the substrate only. Necessary steps were taken to make sure that all the cells and pellets were exposed to the same conditions for their respective batches of experiments.

Author Contributions

X.L. proposed the concept of coating iron oxide ALD films on LMNO particles and designed the experiments. R. L. P. conducted the experiments. R.L.P. and X.L. analyzed the results and drafted the manuscript. Y.J. performed FIB-TEM and STEM-EDS characterizations and analyzed the related results. A.C. performed Mössbauer spectroscopy measurement and analyzed the related results. All authors reviewed the manuscript.

Acknowledgements

The authors thank Clarissa A. Wisner at the Materials Research Center at Missouri University of Science and Technology for TEM analysis. The authors also thank Dr. Manashi Nath in the Chemistry Department for the assistance with impedance measurements.

References

1 Singhal, R., Das, S. R., Oviedo, O., Tomar, M. S. & Katiyar, R. S. Improved electrochemical properties of a coin cell using $LiMn_{1.5}Ni_{0.5}O_4$ as cathode in the 5 V range. *J. Power Sources* **160**, 651-656 (2006).

2 Chen, Z. Y. *et al.* Performance of $LiNi_{0.5}Mn_{1.5}O_4$ prepared by solid-state reaction. *J. Power Sources* **189**, 507-510 (2009).

3 Duncan, H., Duguay, D., Abu-Lebdeh, Y. & Davidson, I. J. Study of the $LiMn_{1.5}Ni_{0.5}O_4$/electrolyte interface at room temperature and 60°C. *J. Electrochem. Soc.* **158**, A537-A545 (2011).

4 Goodenough, J. B. & Park, K.-S. The Li-ion rechargeable battery: A perspective. *J. Am. Chem. Soc.* **135**, 1167-1176 (2013).

5 Hai, B., Shukla, A. K., Duncan, H. & Chen, G. The effect of particle surface facets on the kinetic properties of $LiMn_{1.5}Ni_{0.5}O_4$ cathode materials. *J. Mater. Chem. A* **1**, 759-769 (2013).

6 Sun, Y.-K., Lee, Y.-S., Yoshio, M. & Amine, K. Synthesis and electrochemical properties of ZnO-coated $LiNi_{0.5}Mn_{1.5}O_4$ spinel as 5 V cathode material for lithium secondary batteries. *Electrochem. Solid-State Lett.* **5**, A99-A102 (2002).

7 Han, J.-M., Myung, S.-T. & Sun, Y.-K. Improved electrochemical cycling behavior of ZnO-coated $Li_{1.05}Al_{0.1}Mn_{1.85}O_{3.95}F_{0.05}$ spinel at 55°C. *J. Electrochem. Soc.* **153**, A1290-A1295 (2006).

8 Vicente, C. P., Lloris, J. M. & Tirado, J. L. Understanding the voltage profile of Li insertion into $LiNi_{0.5-y}Fe_yMn_{1.5}O_4$ in Li cells. *Electrochim. Acta* **49**, 1963-1967 (2004).

9 Liu, J. & Manthiram, A. Understanding the improved electrochemical performances of Fe-substituted 5 V spinel cathode $LiMn_{1.5}Ni_{0.5}O_4$. *J. Phys. Chem. C* **113**, 15073-15079 (2009).

10 Zhong, G. B., Wang, Y. Y., Yu, Y. Q. & Chen, C. H. Electrochemical investigations of the $LiNi_{0.45}M_{0.10}Mn_{1.45}O_4$ (M=Fe, Co, Cr) 5V cathode materials for lithium ion batteries. *J. Power Sources* **205**, 385-393 (2012).

11 Şahan, H., Dokan, F. K., Ülgen, A. & Patat, Ş. Improvement of cycling stability of $LiMn_2O_4$ cathode by Fe_2O_3 surface modification for Li-ion battery. *Ionics* **20**, 323-333 (2014).

12 Qing, C., Bai, Y., Yang, J. & Zhang, W. Enhanced cycling stability of $LiMn_2O_4$ cathode by amorphous $FePO_4$ coating. *Electrochim. Acta* **56**, 6612-6618 (2011).

13 George, S. M. Atomic layer deposition: An overview. *Chem. Rev.* **110**, 111-131 (2010).

14 Jung, Y. S. *et al.* Enhanced stability of $LiCoO_2$ cathodes in lithium-ion batteries using surface modification by atomic layer deposition. *J. Electrochem. Soc.* **157**, A75-A81 (2010).

15 Knoops, H. C. M., Donders, M. E., van de Sanden, M. C. M., Notten, P. H. L. & Kessels, W. M. M. Atomic layer deposition for nanostructured Li-ion batteries. *J. Vac. Sci. Technol. A* **30**, 010801 (2012).

16 Peng, Q., Lewis, J. S., Hoertz, P. G., Glass, J. T. & Parsons, G. N. Atomic layer deposition for electrochemical energy generation and storage systems. *J. Vac. Sci. Technol. A* **30**, 010803 (2012).

17 Patel, R. L. *et al.* Significant capacity and cycle-life improvement of lithium-ion batteries through ultrathin conductive film stabilized cathode particles. *Adv. Mater. Interfaces* **2**, 1500046 (2015).

18 Wu, Y., Wei, Y., Wang, J., Jiang, K. & Fan, S. Conformal Fe_3O_4 sheath on aligned carbon nanotube scaffolds as high-performance anodes for lithium ion batteries. *Nano Lett.* **13**, 818-823 (2013).

19 El-Shinawi, H., Schulze, A. S., Neumeier, M., Leichtweiß, T. & Janek, J. FeO_x-coated SnO_2 as an anode material for lithium ion batteries. *J. Phys. Chem. C* **118**, 8818-8823 (2014).

20 Scheffe, J. R. *et al.* Atomic layer deposition of iron(III) oxide on zirconia nanoparticles in a fluidized bed reactor using ferrocene and oxygen. *Thin Solid Films* **517**, 1874-1879 (2009).

21 Ma, Y., Fang, C., Ding, B., Ji, G. & Lee, J. Y. Fe-doped Mn_xO_y with hierarchical porosity as a high-performance lithium-ion battery anode. *Adv. Mater.* **25**, 4646-4652 (2013).

22 Shin, D. W., Bridges, C. A., Huq, A., Paranthaman, M. P. & Manthiram, A. Role of cation ordering and surface segregation in high-voltage spinel $LiMn_{1.5}Ni_{0.5-x}M_xO_4$(M = Cr, Fe, and Ga) cathodes for lithium-ion batteries. *Chem. Mater.* **24**, 3720-3731 (2012).

23 Amine, K., Tukamoto, H., Yasuda, H. & Fujita, Y. Preparation and electrochemical investigation of $LiMn_{2-x}Me_xO_4$ (Me: Ni, Fe, and x= 0.5, 1) cathode materials for secondary lithium batteries. *J. Power Sources* **68**, 604-608 (1997).

24 Zhang, Y. *et al.* Atomic layer deposition of superparamagnetic and ferrimagnetic magnetite thin films. *J. Appl. Phys.* **117**, 17C743 (2015).

25 Rooth, M. *et al.* Atomic layer deposition of iron oxide thin films and nanotubes using ferrocene and oxygen as precursors. *Chem. Vap. Depos.* **14**, 67-70 (2008).

26 Cornell, R. M. & Schwertmann, U. *The Iron Oxides: Structure, Properties, Reactions, Occurences and Uses, Second Edition*. (Wiley-VCH Verlag GmbH & Co., 2003).

27 Vandenberghe, R. E., Barrero, C. A., Da Costa, G. M., Van San, E. & De Grave, E. Mössbauer characterization of iron oxides and (oxy)hydroxides: The present state of the art. *Hyperfine Interact.* **126**, 247-259 (2000).

28 Tang, Z. X., Sorensen, C. M., Klabunde, K. J. & Hadjipanayis, G. C. Preparation of manganese ferrite fine particles from aqueous solution. *J. Colloid Interf. Sci.* **146**, 38-52 (1991).

29 Corneille, J. S., He, J. W. & Goodman, D. W. Preparation and characterization of ultra-thin iron oxide films on a Mo(100) surface. *Surf. Sci.* **338**, 211-224 (1995).

30 Edström, K., Gustafsson, T. & Thomas, J. O. The cathode–electrolyte interface in the Li-ion battery. *Electrochim. Acta* **50**, 397-403 (2004).

31 Alcántara, R., Jaraba, M., Lavela, P. & Tirado, J. L. X-ray diffraction and electrochemical impedance spectroscopy study of zinc coated $LiNi_{0.5}Mn_{1.5}O_4$ electrodes. *J. Electroanal. Chem.* **566**, 187-192 (2004).

32 Lee, S.-W. *et al.* Electrochemical characteristics of Al_2O_3-coated lithium manganese spinel as a cathode material for a lithium secondary battery. *J. Power Sources* **126**, 150-155 (2004).

33 Iguchi, E., Tokuda, Y., Nakatsugawa, H. & Munakata, F. Electrical transport properties in $LiMn_2O_4$, $Li_{0.95}Mn_2O_4$, and $LiMn_{1.95}B_{0.05}O_4$ (B=Al or Ga) around room temperature. *J. Appl. Phys.* **91**, 2149-2154 (2002).

34 Yang, Y. *et al.* Single nanorod devices for battery diagnostics: A case study on $LiMn_2O_4$. *Nano Lett.* **9**, 4109-4114 (2009).

35 Liang, X. H. *et al.* Novel processing to produce polymer/ceramic nanocomposites by atomic layer deposition. *J. Am. Ceram. Soc.* **90**, 57-63 (2007).

36 Lagarec, K. & Rancourt, D. G. Extended Voigt-based analytic lineshape method for determining N-dimensional correlated hyperfine parameter distributions in Mössbauer spectroscopy. *Nucl. Instrum. Methods Phys. Res. B* **129**, 266-280 (1997).

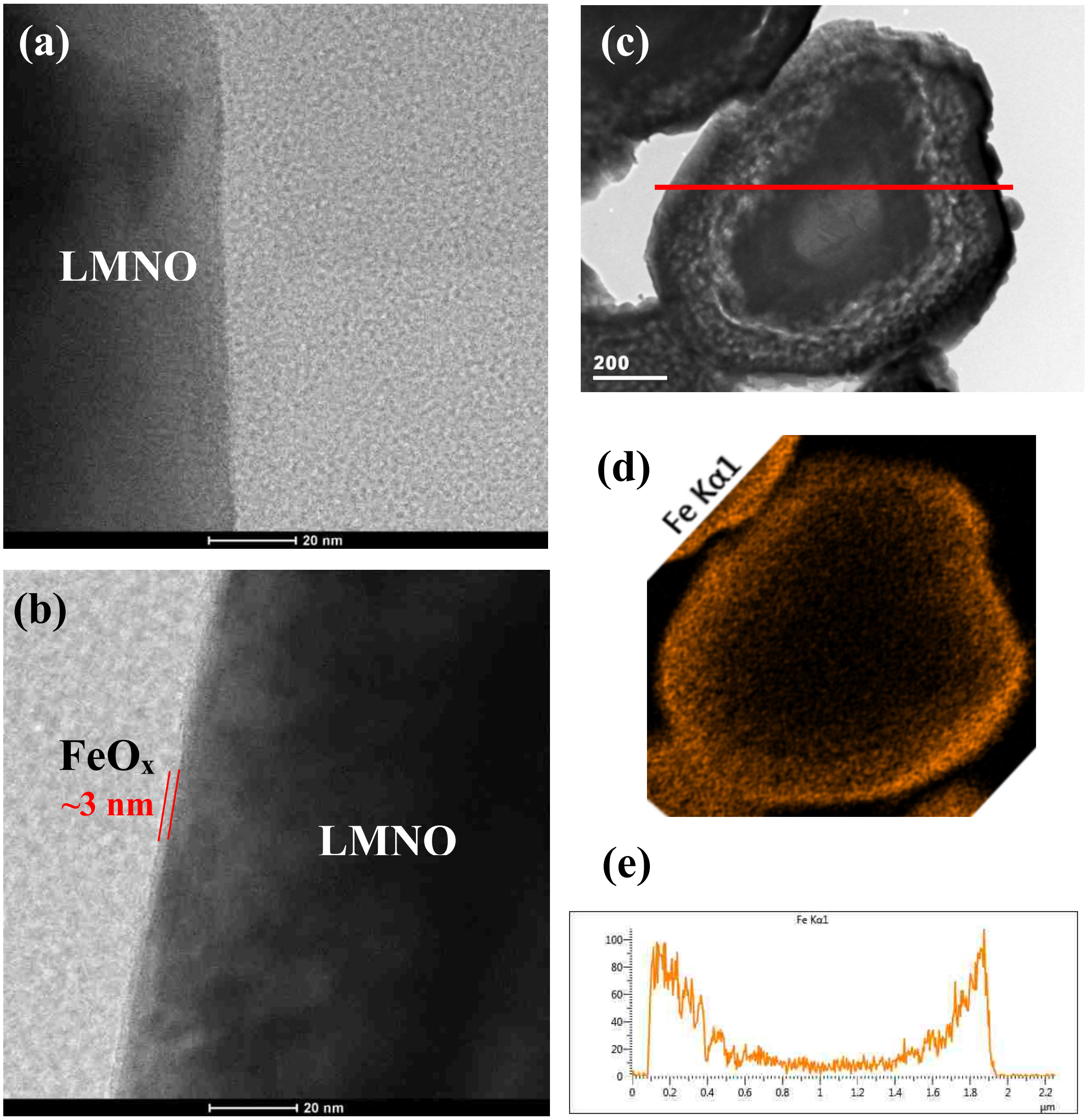

Figure 1. TEM images of (a) clean edge of an uncoated $LiMn_{1.5}Ni_{0.5}O_4$ particle, and (b) ~3 nm of conformal iron oxide film coated on one $LiMn_{1.5}Ni_{0.5}O_4$ particle after 160 cycles of iron oxide ALD, (c) cross sectional TEM image of one $LiMn_{1.5}Ni_{0.5}O_4$ particle with 160 cycles of iron oxide ALD, (d) Fe element mapping of cross-sectioned surface by EDS, and (e) Fe EDS line scanning along the red line as shown in Figure 1c. TEM image indicates that conformal iron oxide films were coated on primary $LiMn_{1.5}Ni_{0.5}O_4$ particle surface. EDS mapping and EDS element line scanning indicates that Fe was doped in the lattice structure of $LiMn_{1.5}Ni_{0.5}O_4$.

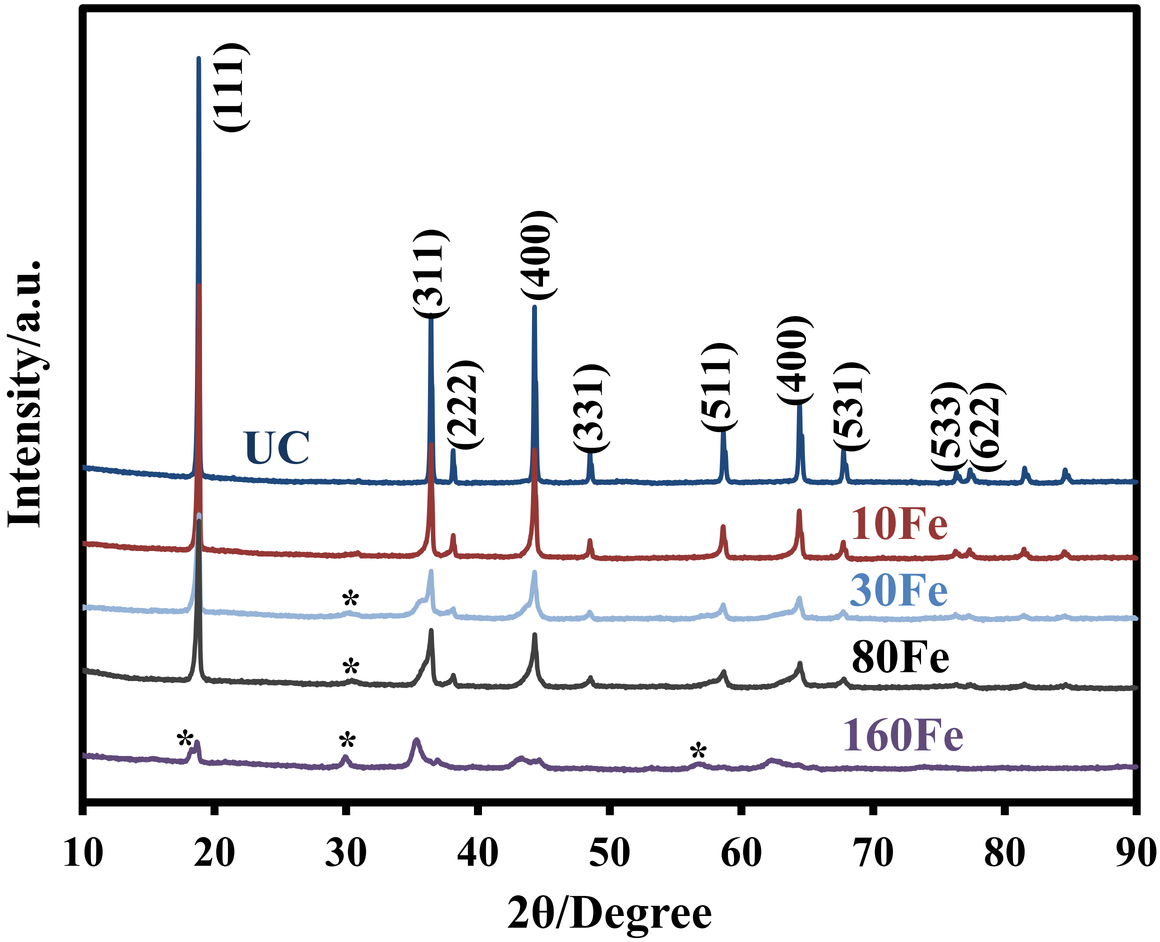

Figure 2. XRD patterns of uncoated $LiMn_{1.5}Ni_{0.5}O_4$ particles and coated with different cycles of ALD iron oxide. * indicates the dominant Fe_3O_4 phase due to iron oxide ALD coating.

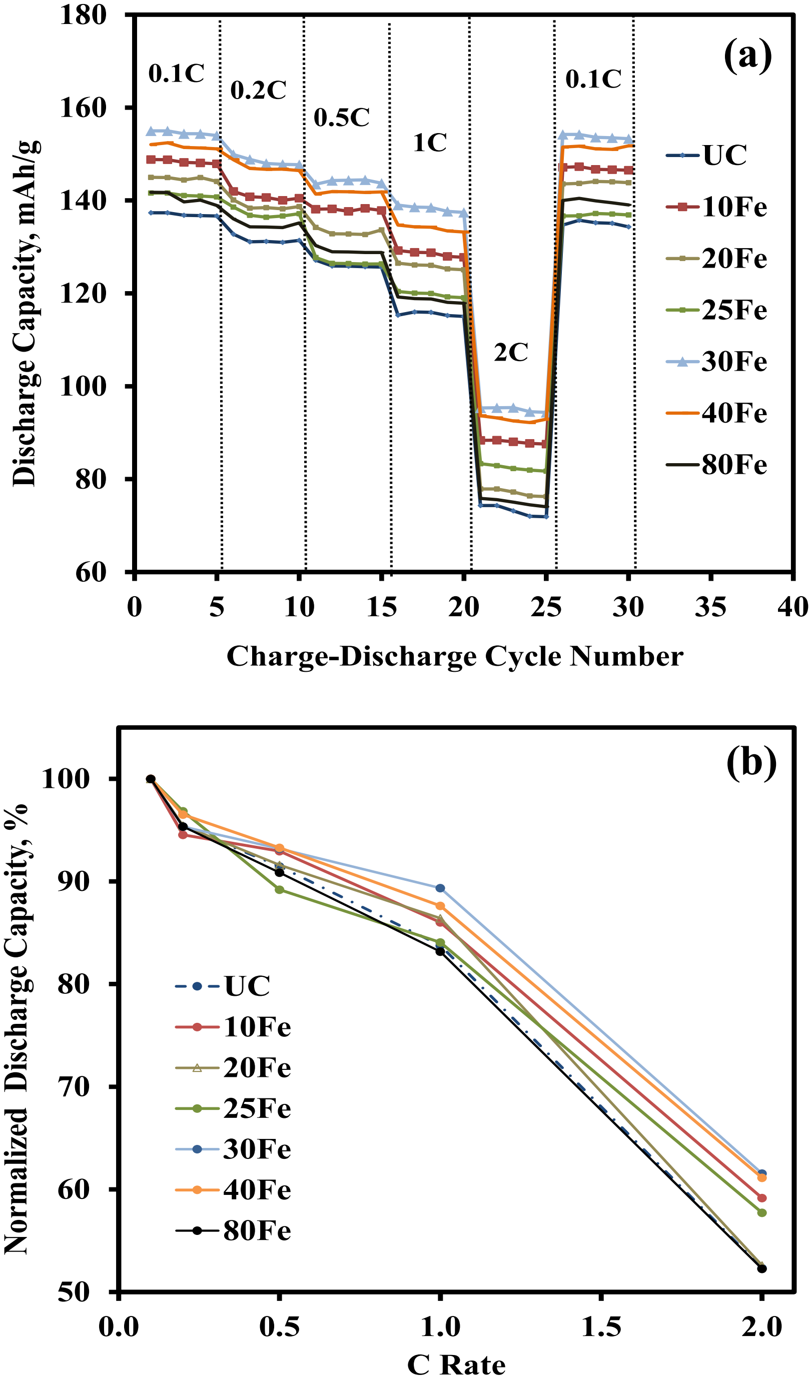

Figure 3. Galvanostatic discharge capacities of cells made of $LiMn_{1.5}Ni_{0.5}O_4$ particles coated with different thicknesses of iron oxide at different C rates in a voltage range between 3.5 – 5 V (a) at room temperature and (c) at 55 ºC; in (b) and (d) their respective normalized capacity vs. rate curves.

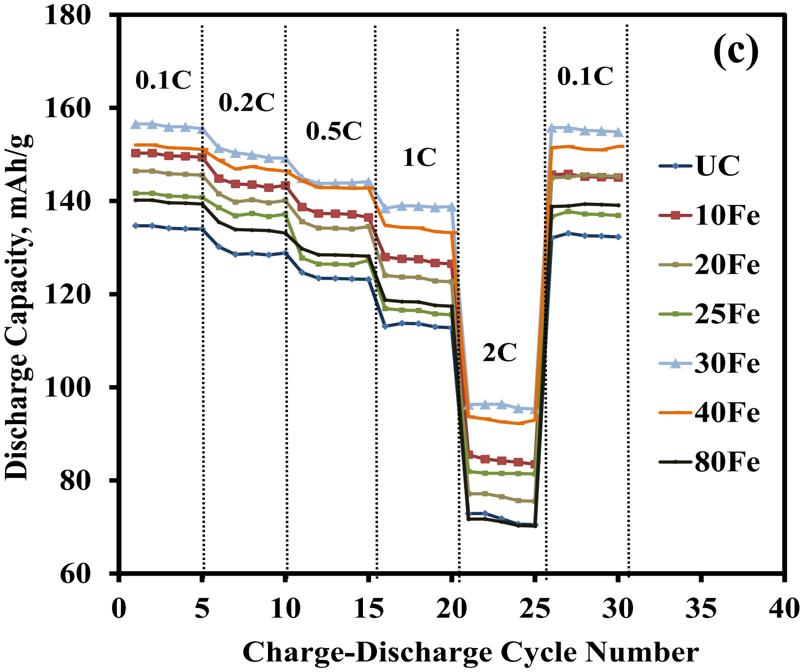

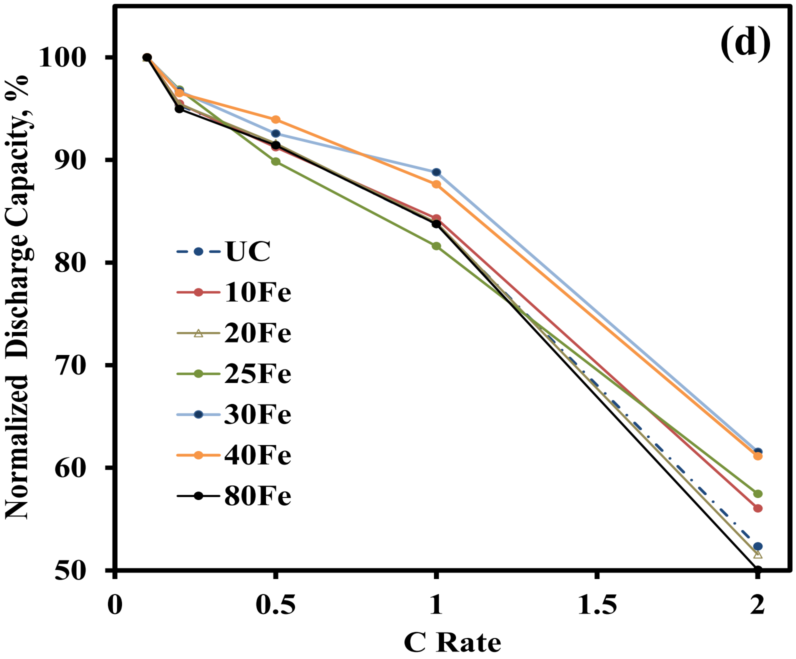

Figure 3. Galvanostatic discharge capacities of cells made of $LiMn_{1.5}Ni_{0.5}O_4$ particles coated with different thicknesses of iron oxide at different C rates in a voltage range between 3.5 – 5 V (a) at room temperature and (c) at 55 ºC; in (b) and (d) their respective normalized capacity vs. rate curves. (Cont.)

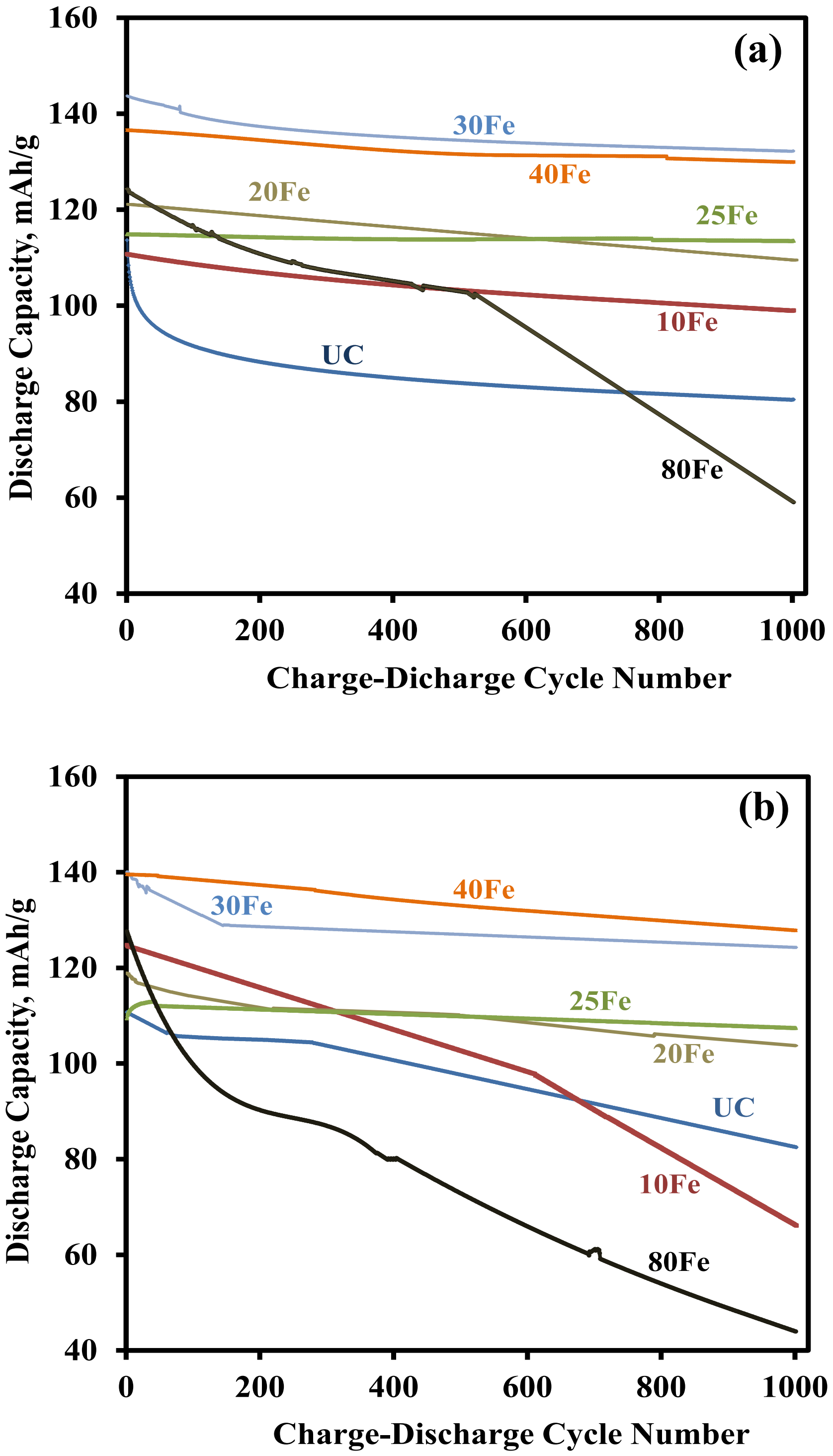

Figure 4. Discharge capacities of cells made of $LiMn_{1.5}Ni_{0.5}O_4$ particles coated with different thicknesses of iron oxide at a 1C rate in a voltage range between 3.5 – 5 V (a) at room temperature and (b) at 55 ºC.

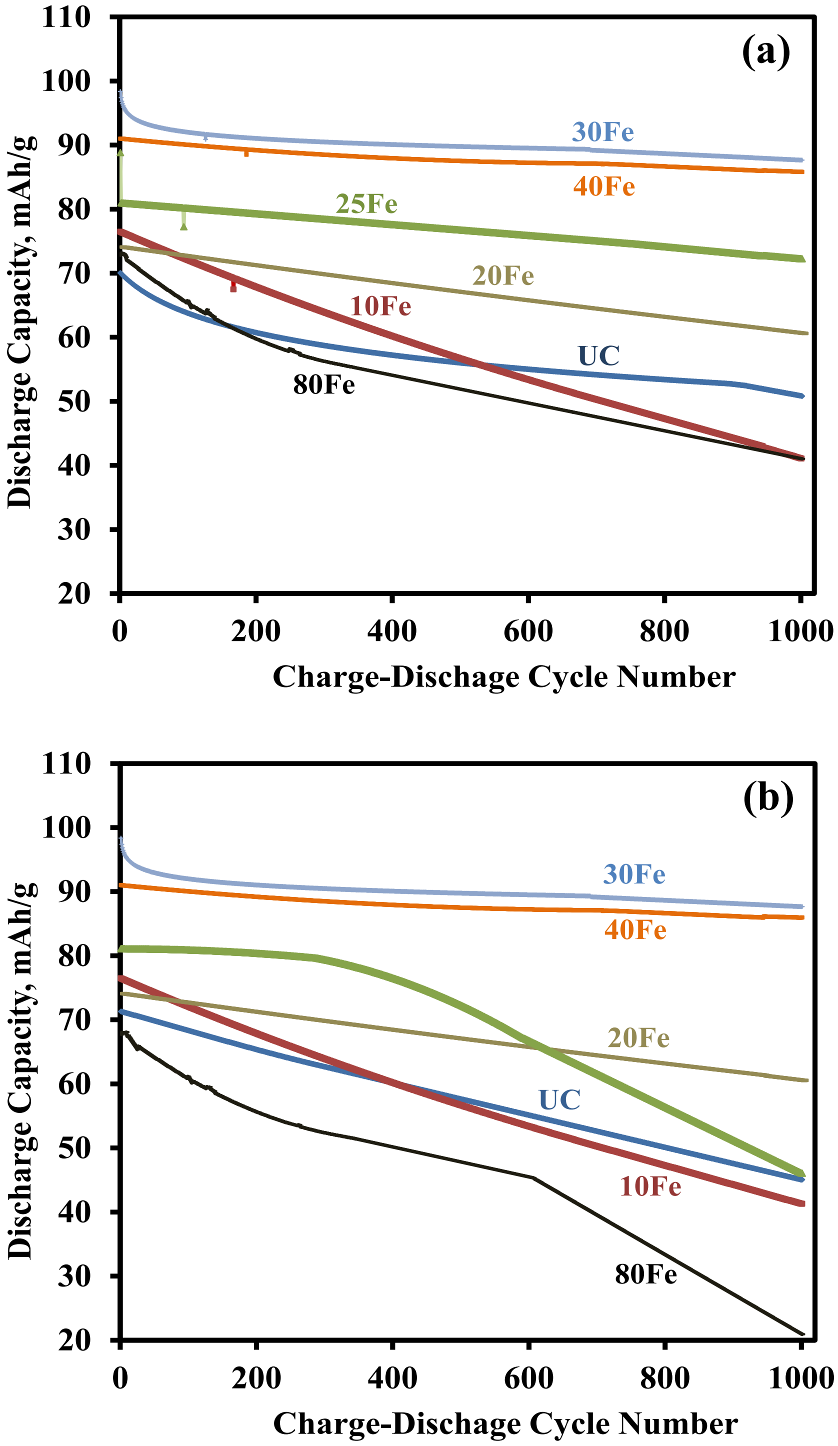

Figure 5. Discharge capacities of cells made of $LiMn_{1.5}Ni_{0.5}O_4$ particles coated with different thicknesses of iron oxide at a 2C rate in a voltage range between 3.5 – 5 V (a) at room temperature and (b) at 55 ºC.

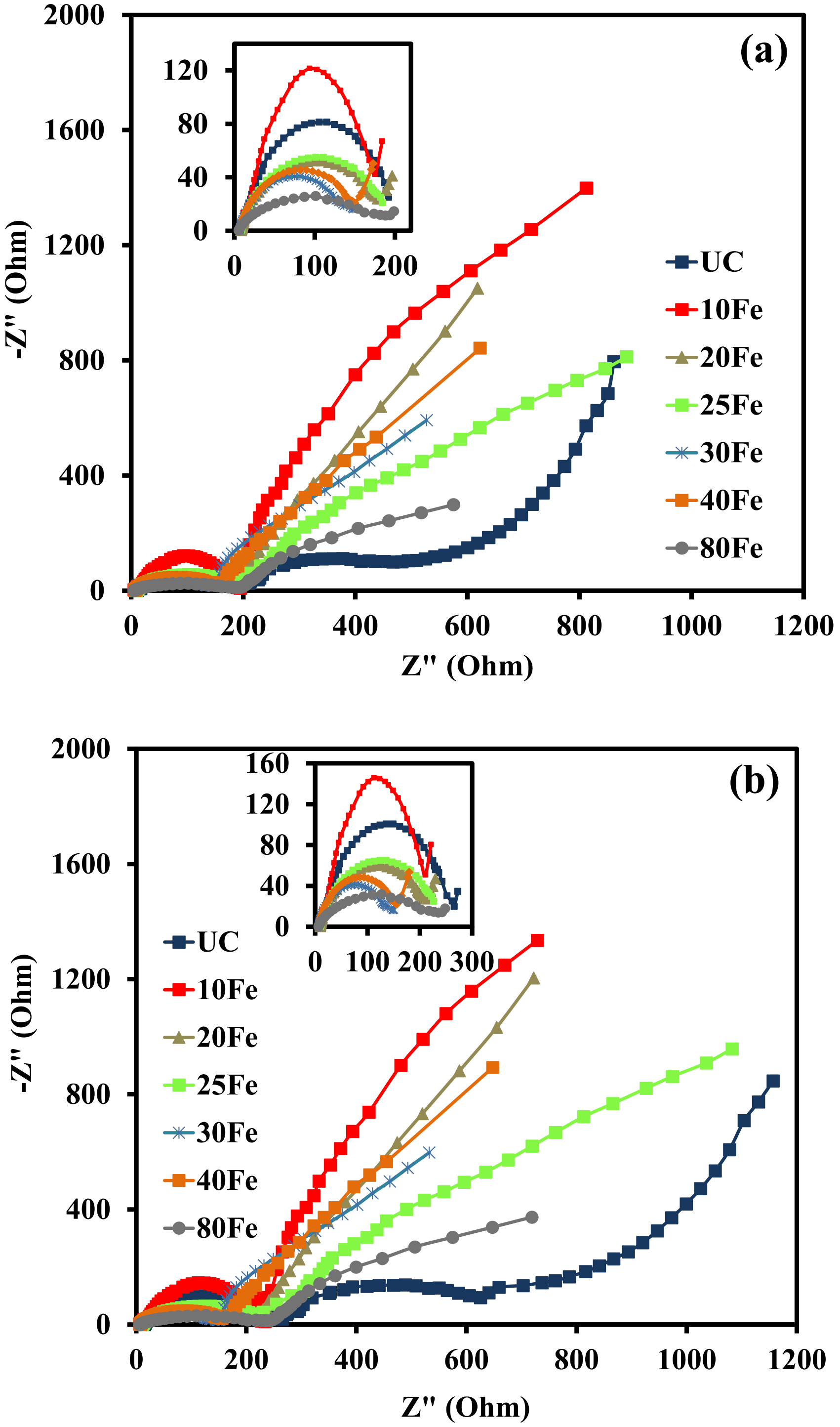

Figure 6. Electrochemical impedance spectra at room temperature for uncoated $LiMn_{1.5}Ni_{0.5}O_4$ particles and coated with various thicknesses of iron oxide after (a) 1st cycle and (b) 1,000th charge-discharge cycles, and (c) equivalent circuit fit for the impedance spectra. Inset images show the high frequency regions (1 MHz – 100 Hz) of the impedance spectra.

(c)

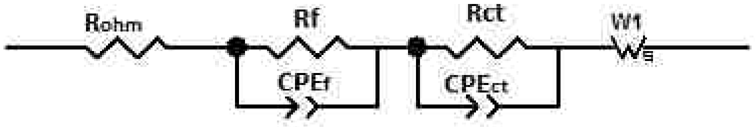

Figure 6. Electrochemical impedance spectra at room temperature for uncoated $LiMn_{1.5}Ni_{0.5}O_4$ particles and coated with various thicknesses of iron oxide after (a) 1st cycle and (b) 1,000th charge-discharge cycles, and (c) equivalent circuit fit for the impedance spectra. Inset images show the high frequency regions (1M Hz – 100 Hz) of the impedance spectra. (Cont.)

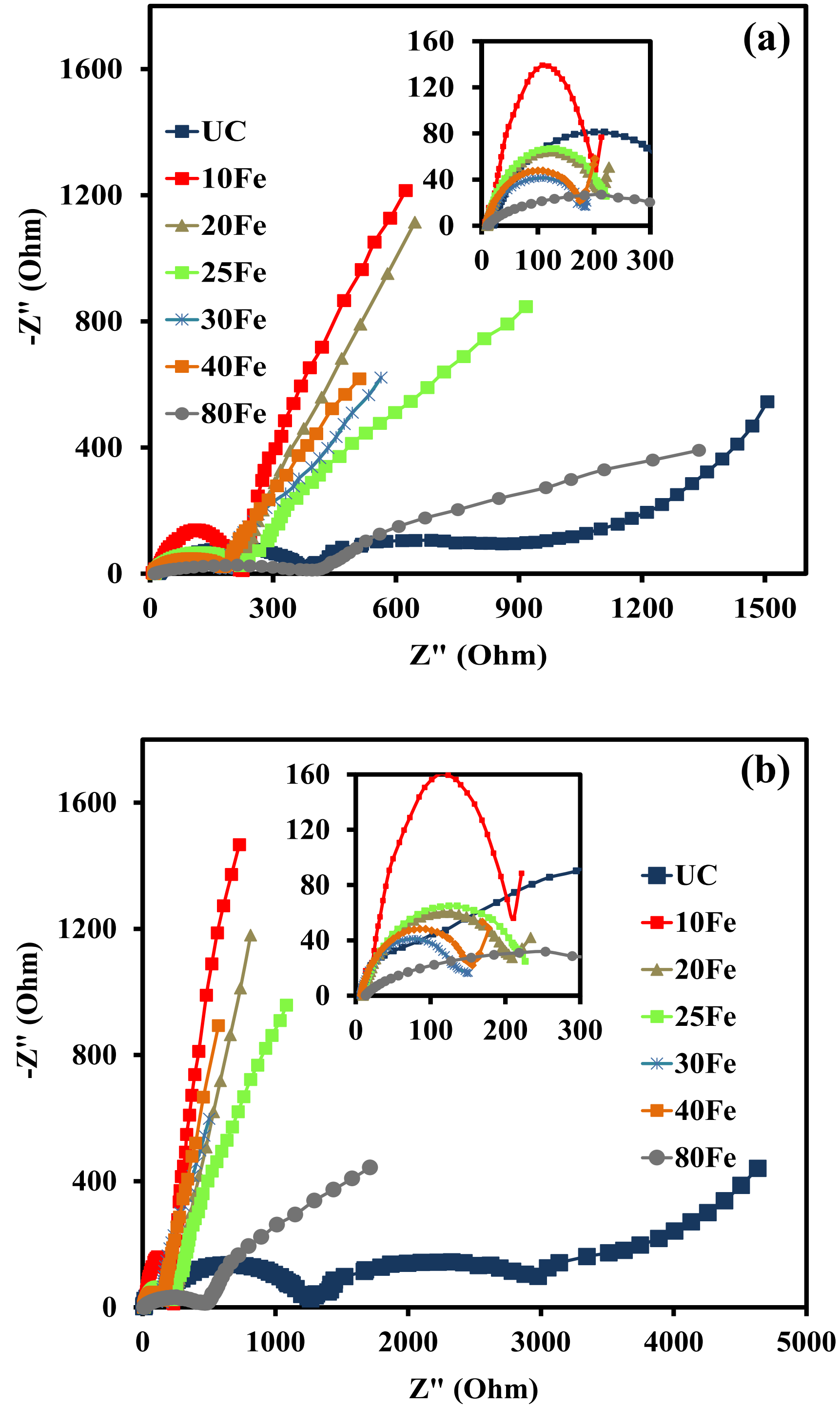

Figure 7. Electrochemical impedance spectra at 55 ºC for uncoated LiMn$_{1.5}$Ni$_{0.5}$O$_4$ particles and coated with various thicknesses of iron oxide after (a) 1st cycle and (b) 1,000th charge-discharge cycles. Inset images show the high frequency regions (1M Hz – 100 Hz) of the impedance spectra.

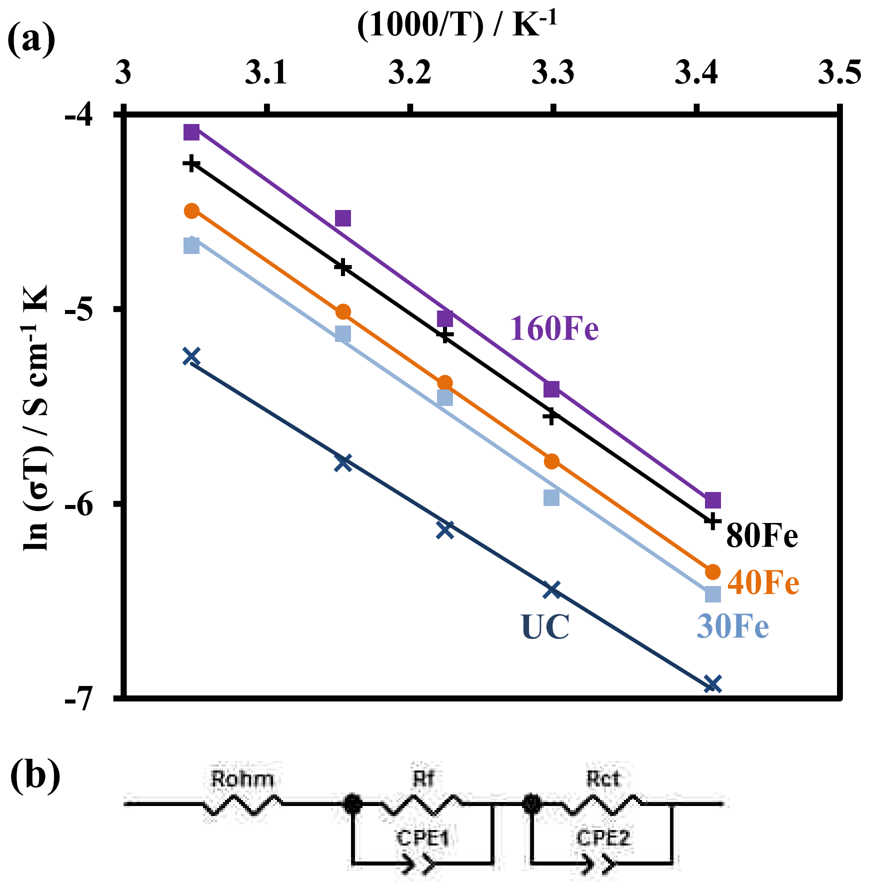

Figure 8. (a) Arrhenius plot of the UC and 30Fe, 40Fe, 80Fe, and 160Fe coated $LiMn_{1.5}Ni_{0.5}O_4$ particles for the effects of temperature on conductivity, and (b) equivalent circuit for impedance spectra.

Table 1. Impedance parameters using equivalent circuit models for electrodes made of UC, 10Fe, 20Fe, 25Fe, 30Fe, 40Fe, 80Fe coated $LiMn_{1.5}Ni_{0.5}O_4$ particles: (a) at room temperature, (b) at 55 ºC.

(a)

											Warburg Short					
RT	**R_{ohm} (Ω)**		**R_f (Ω)**		**R_{ct} (Ω)**		**C_f (μF)**		**C_{ct} (μF)**		**R_w (Ω)**		**τ (s)**		**P**	
	0th	**1000th**	**0th**	**1000th**	**0th**	**1000th**	**0th**	**1000th**	**0th**	**1000th**	**0th**	**1000th**	**0th**	**1000th**	**0th**	**1000th**
UC	4.9	5.8	25.1	30.1	175.2	210.2	17.5	21.1	6.1	1.3	5324	6678	100.8	171.0	0.8	0.6
10Fe	9.8	11.7	15.4	18.5	170.6	187.7	15.4	17.0	4.7	3.0	1205	2400	52.5	56.0	0.7	0.6
20Fe	11.8	14.0	20.2	24.2	171.9	189.1	11.2	12.3	4.1	1.9	2240	6332	21.6	44.1	0.5	0.7
25Fe	7.8	9.3	22.1	26.5	165.5	182.1	10.5	11.5	2.2	2.1	2803	5232	27.9	46.8	0.7	0.8
30Fe	8.8	10.5	13.5	16.2	135.1	141.9	4.6	3.5	2.7	1.0	2642	4199	7.3	9.5	0.8	0.8
40Fe	10.8	12.8	14.5	17.4	145.2	152.5	6.5	7.5	3.5	0.2	3240	4210	10.8	11.1	0.6	0.5
80Fe	9.8	11.7	19.5	23.4	180.6	216.7	1.2	10.5	5.9	4.0	2529	2952	76.5	112.5	0.5	0.3

(b)

											Warburg Short					
55 °C	**R_{ohm} (Ω)**		**R_f (Ω)**		**R_{ct} (Ω)**		**C_f (μF)**		**C_{ct} (μF)**		**R_w (Ω)**		**τ (s)**		**P**	
	0th	**1000th**	**0th**	**1000th**	**0th**	**1000th**	**0th**	**1000th**	**0th**	**1000th**	**0th**	**1000th**	**0th**	**1000th**	**0th**	**1000th**
UC	5.4	6.4	31.4	37.7	219.0	262.8	21.9	26.3	7.7	1.6	6655	8348	126.0	213.8	0.8	0.7
10Fe	10.8	12.8	16.9	20.3	187.7	206.4	16.7	18.7	5.1	3.3	1326	2640	57.7	61.6	0.8	0.6
20Fe	12.9	15.4	22.2	26.7	189.1	208.0	12.3	13.6	4.5	2.1	2464	6965	23.8	48.5	0.6	0.7
25Fe	8.6	10.3	24.3	29.1	182.1	200.3	11.5	12.6	2.4	2.3	3083	5755	30.7	51.5	0.7	0.9
30Fe	9.7	11.6	14.9	17.9	148.6	156.0	5.1	3.8	3.0	1.1	3205	4765	8.0	10.4	0.8	0.9
40Fe	11.9	14.1	16.0	19.2	159.7	167.7	7.2	8.3	3.9	0.2	3564	4631	11.9	12.2	0.7	0.5
80Fe	11.9	14.1	23.6	28.3	218.5	262.2	1.5	12.7	7.1	4.9	3060	3572	92.6	136.1	0.5	0.3

Supporting Information

Structural Characterization

The selective area electron diffraction (SAED) patterns obtained, aligned along their main axis, from the UC and the 160Fe samples shown in Figures S2a and S2b, respectively, clearly demonstrated the differences in the structure for $LiMn_{1.5}Ni_{0.5}O_4$ (LMNO) before and after iron oxide ALD coating, which was also confirmed by unidentified peaks in XRD spectra of 160Fe (Figure 2). In comparison, pristine LMNO showed fewer lattice peaks in the spinal diffraction pattern in the (100) zone than the 160Fe. These extra peaks, for the case of 160Fe, correspond to the cubic phase ($P4_332$)[1].

X-ray photoelectron spectroscopy (XPS, Kratos Axis 165) was used to study the oxidation state of Fe by employing Al K (α) excitation, operated at 150 W and 15 kV. The peaks were corrected with C 1s at 284.6 eV. The values for the $Fe2p_{3/2}$ peak reported in the literature differs by 0.9 eV between two extreme values 710.6 eV [2] and 711.5 eV[3]. As shown in Figure S5, the 30Fe and 40Fe samples show a very sharp peak of Fe 2p at 711.5 eV, which is very close to the observed Fe (III) $2p_{3/2}$ in Fe_2O_3[4-7]. Also, these two samples show a small peak at 724 eV, which is very close to the observed peak of Fe (III) $2p_{1/2}$ in Fe_2O_3[4-8]. This indicates that the iron oxide deposited by ALD is Fe_3O_4 or γ-Fe_2O_3 as peaks for Fe (II) as well as Fe (III) oxidation state was observed. A faint confined peak at 710.1 eV for the 40Fe sample is representing Fe_3O_4. There is also a small satellite peak at ~717 eV in the 30Fe and 40Fe samples, which indicates the existence of Fe_2O_3, as reported by Gota et al[9]. Iron at an intermediate oxidation state in Fe_3O_4 with a mixture of Fe (II) and Fe (III) presents a BE value of 710.2 eV. The Fe^{3+} component of Fe $2p_{3/2}$ in γ-Fe_2O_3 is at

710.1 eV. The peak-shifts for 30Fe, 40Fe, and 80Fe samples are because that the main difference between the two sets of samples is the coordination of the Fe^{3+} cations. In the α-compounds, the crystal structure is oriented in such a way that all of the cations are octahedrally coordinated. In the γ-compounds, on the other hand, three-quarters of the Fe^{3+} cations are octahedrally coordinated whereas the other quarter of the cations are tetrahedrally coordinated. This also explains the satellite peaks, as proven in literature[10], the XPS Fe 2p spectrum of 40Fe possesses smaller satellite intensity as compared with that of 30Fe due to the larger Fe 3d to O 2p hybridization in 40Fe, which has higher amount of γ-Fe_2O_3. The formation of a conformal iron oxide ALD layer on the surface can act as an artificial solid permeable interface (SPI) layer and helps prevent electrolyte decomposition at higher voltage[6]. The XRD and SAED results indicate that Fe in some oxidation state has penetrated into the lattice structure of LMNO[11,12].

References

1 Hai, B., Shukla, A. K., Duncan, H. & Chen, G. The effect of particle surface facets on the kinetic properties of $LiMn_{1.5}Ni_{0.5}O_4$ cathode materials. *J. Mater. Chem. A* **1**, 759-769, (2013).

2 Hawn, D. D. & DeKoven, B. M. Deconvolution as a correction for photoelectron inelastic energy losses in the core level XPS spectra of iron oxides. *Surf. Interface Anal.* **10**, 63-74 (1987).

3 Konno, H., Sasaki, K., Tsunekawa, M., Takamori, T. & Furuichi, R. X-ray photoelectron spectroscopic analysis of surface products on pyrite formed by bacterial leaching. *Bunseki Kagaku* **40**, 609-616 (1991).

4 Yamashita, T. & Hayes, P. Analysis of XPS spectra of Fe^{2+} and Fe^{3+} ions in oxide materials. *Appl. Surf. Sci.* **254**, 2441-2449 (2008).

5 Wu, C., Zhang, H., Wu, Y.-X., Zhuang, Q.-C., Tian, L.-L. & Zhang, X.-T. Synthesis and characterization of Fe@Fe_2O_3 core-shell nanoparticles/graphene anode material for lithium-ion batteries. *Electrochim. Acta* **134**, 18-27 (2014).

6 Philippe, B., Valvo, M., Lindgren, F., Rensmo, H. & Edström, K. Investigation of the electrode/electrolyte interface of Fe_2O_3 composite electrodes: Li vs Na batteries. *Chem. Mater.* **26**, 5028-5041, (2014).

7 Hu, T., Xie, M., Zhong, J., Sun, H.-T., Sun, X., Scott, S., George, S.M., Liu, C.-S. & Lian, J. Porous Fe_2O_3 nanorods anchored on nitrogen-doped graphenes and ultrathin Al_2O_3 coating by atomic layer deposition for long-lived lithium ion battery anode. *Carbon* **76**, 141-147 (2014).

8 Zhu, X., Song, X., Ma, X. & Ning, G. Enhanced electrode performance of Fe_2O_3 nanoparticle-decorated nanomesh graphene as anodes for lithium-ion batteries. *ACS Appl. Mater. Interfaces* **6**, 7189-7197 (2014).

9 Gota, S., Moussy, J. B., Henriot, M., Guittet, M. J. & Gautier-Soyer, M. Atomic-oxygen-assisted MBE growth of Fe_3O_4 (1 1 1) on α-Al_2O_3 (0 0 0 1). *Surf. Sci.* **482–485,** 809-816 (2001).

10 Fujii, T., de Groot, F.M.F., Sawatzky, G.A., Voogt, F.C., Hibma, T. & Okada, K. In-situ XPS analysis of various iron oxide films grown by NO_2-assisted molecular-beam epitaxy. *Phys. Rev. B* **59**, 3195-3202 (1999).

11 Liu, J. & Manthiram, A. Understanding the improved electrochemical performances of Fe-substituted 5 V spinel cathode $LiMn_{1.5}Ni_{0.5}O_4$. *J. Phys. Chem. C* **113**, 15073-15079 (2009).

12 Kim, J. H., Myung, S. T., Yoon, C. S., Kang, S. G. & Sun, Y. K. Comparative study of $LiNi_{0.5}Mn_{1.5}O_{4-\delta}$ and $LiNi_{0.5}Mn_{1.5}O_4$ cathodes having two crystallographic structures: $Fd\bar{3}m$ and $P4_332$. *Chem. Mater.* **16**, 906-914 (2004).

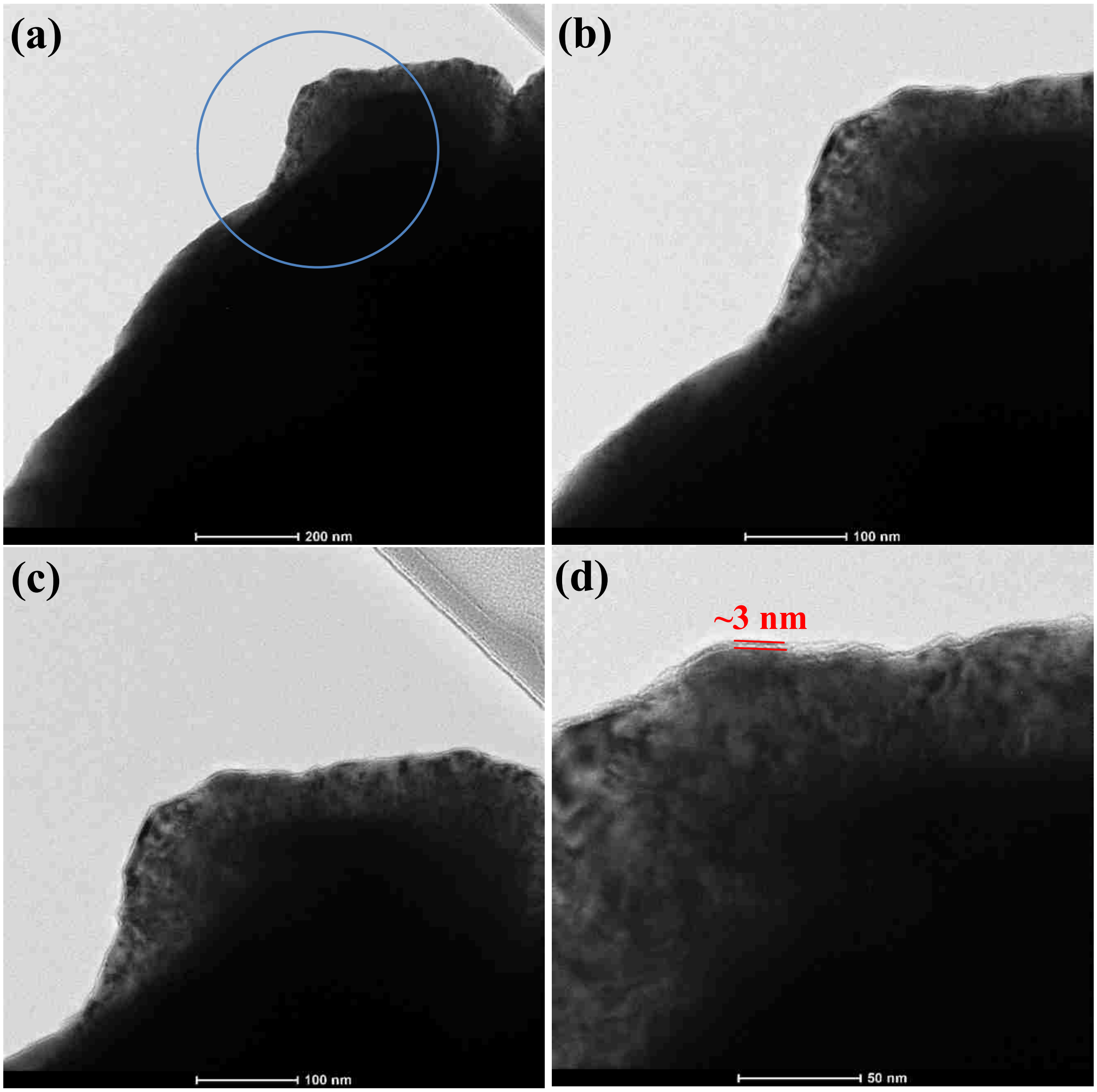

Figure S1. TEM images of 160 cycles of iron oxide ALD coated $LiMn_{1.5}Ni_{0.5}O_4$ particles. Conformal iron oxide film coverage shown in (a), (b), (c), and (d) at different magnification levels.

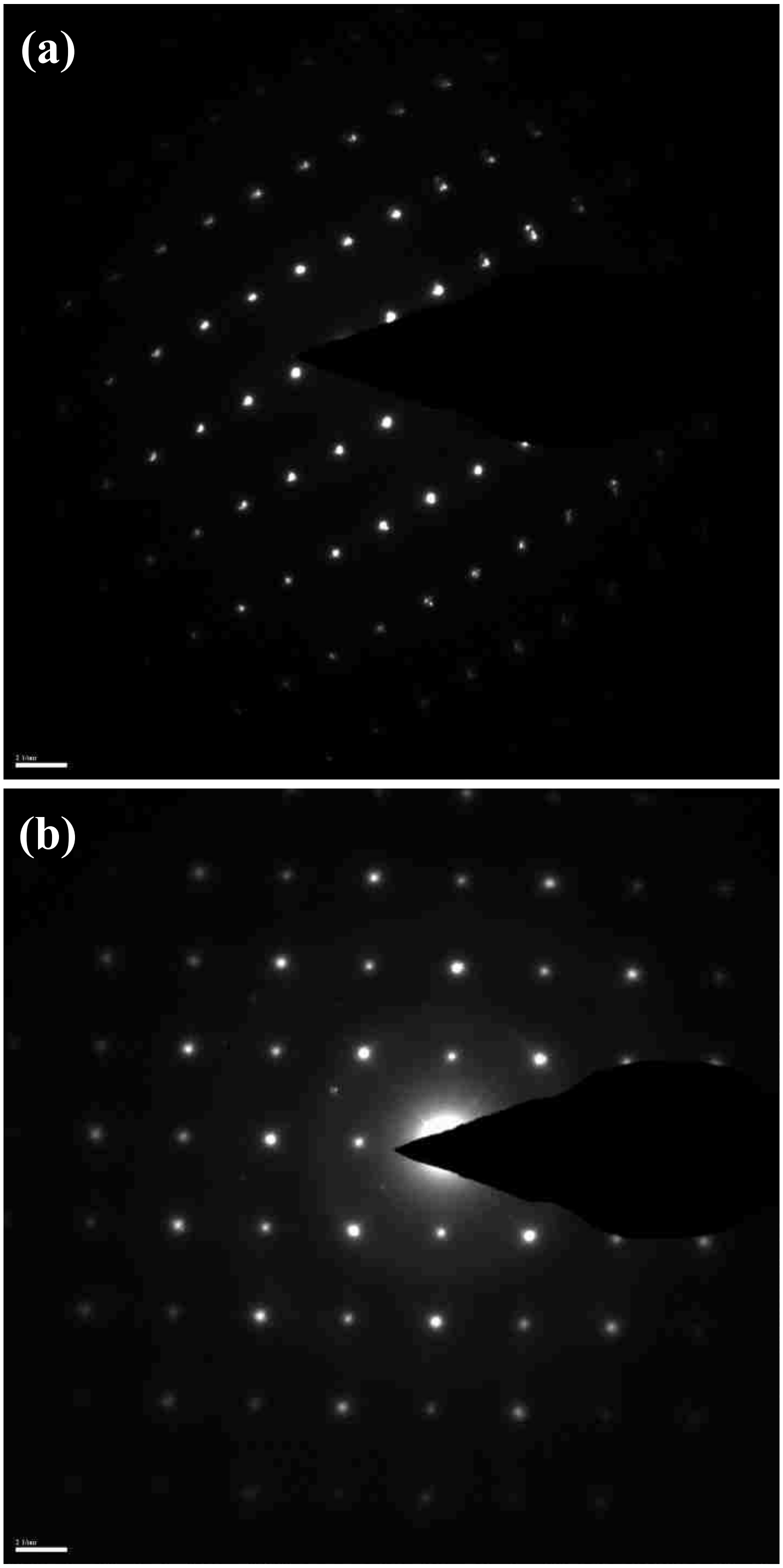

Figure S2. SAED patterns from TEM images of (a) uncoated, and (b) 160 cycles of iron oxide ALD coated $LiMn_{1.5}Ni_{0.5}O_4$ particles.

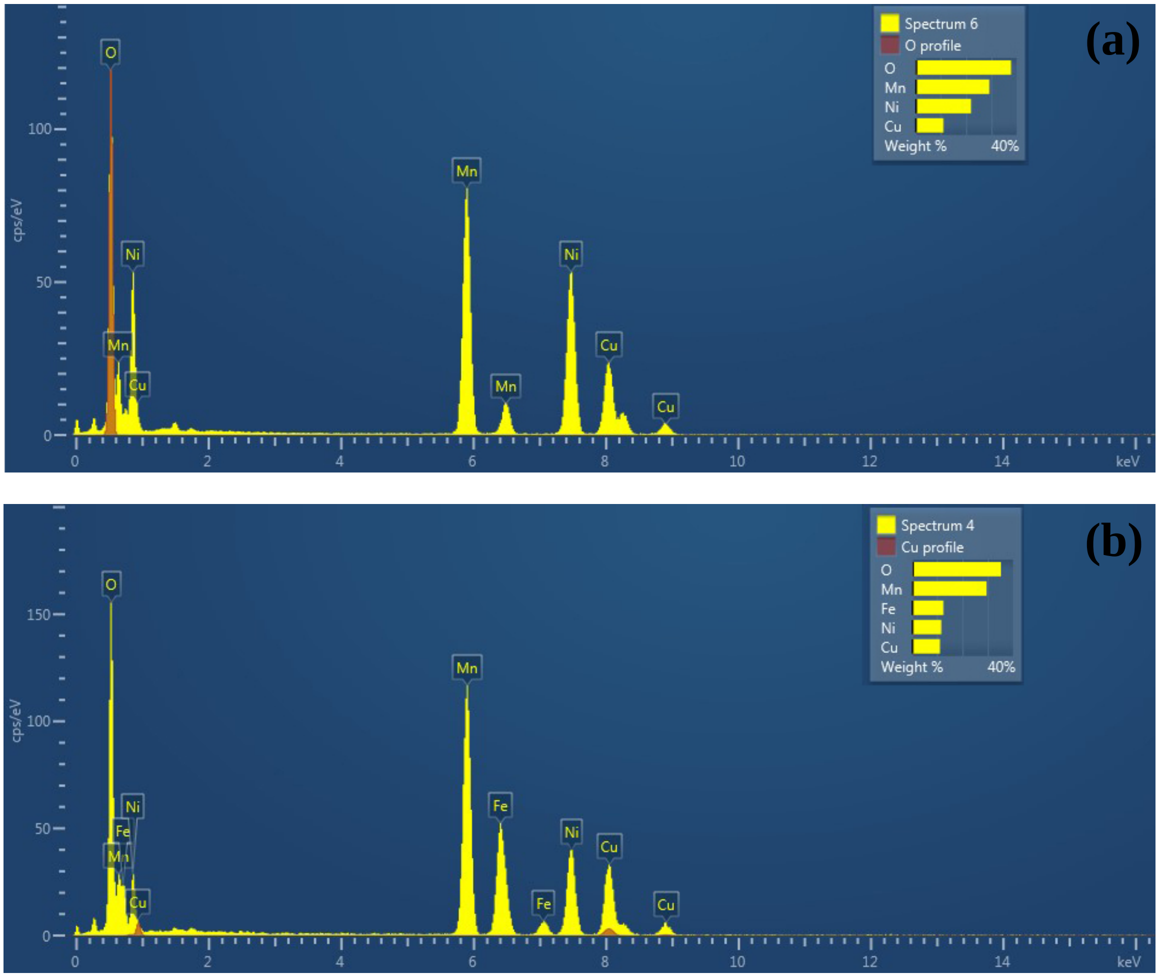

Figure S3. EDS spectra of (a) uncoated, and (b) 160 cycles of iron oxide ALD coated $LiMn_{1.5}Ni_{0.5}O_4$ particles.

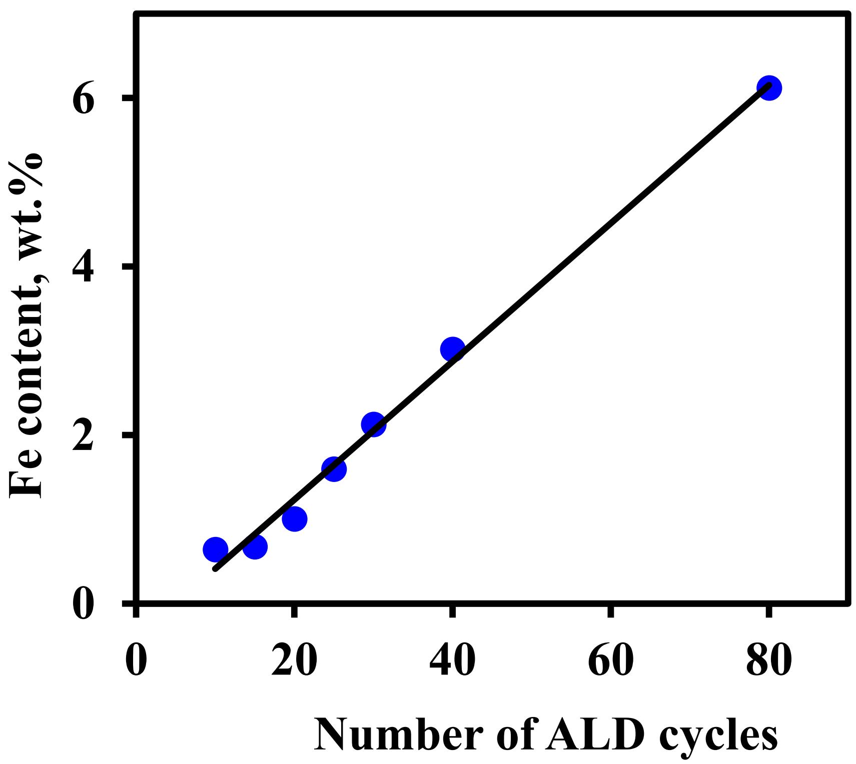

Figure S4. Iron contents on $LiMn_{1.5}Ni_{0.5}O_4$ particles versus the number of ALD coating cycles.

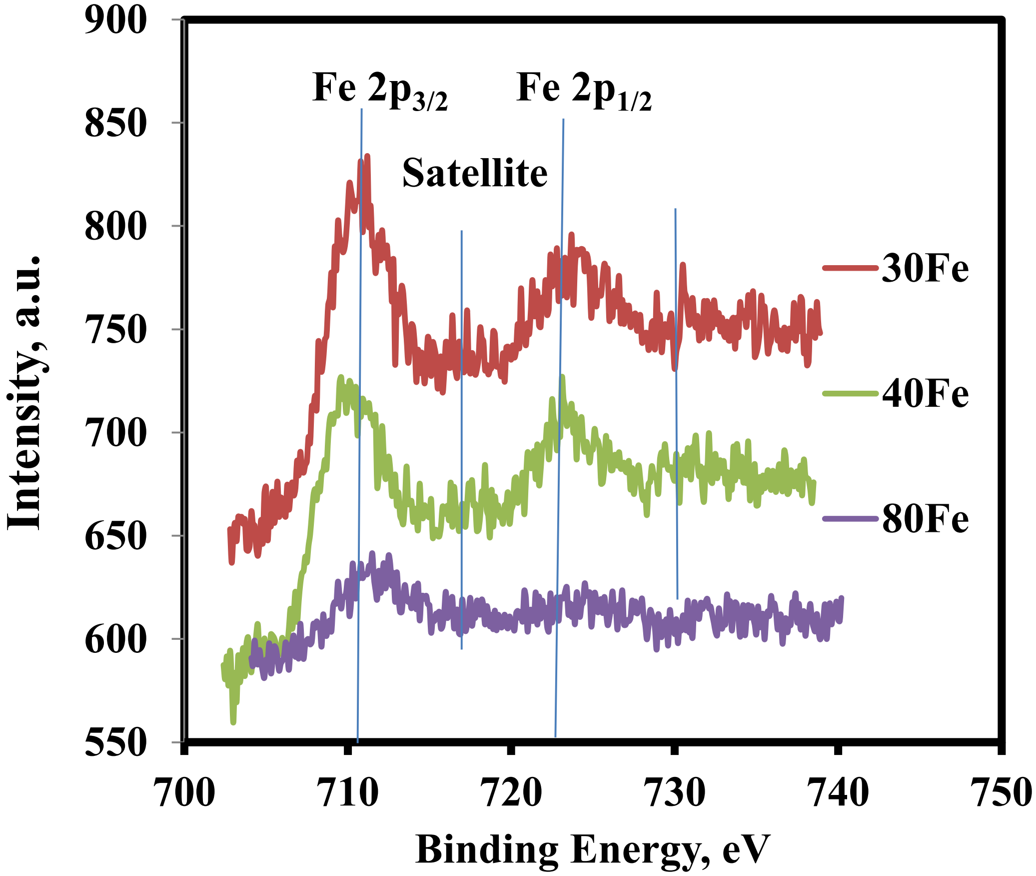

Figure S5. Fe 2p XPS spectra of 30, 40, and 80 cycles of iron oxide ALD coated $LiMn_{1.5}Ni_{0.5}O_4$ samples.

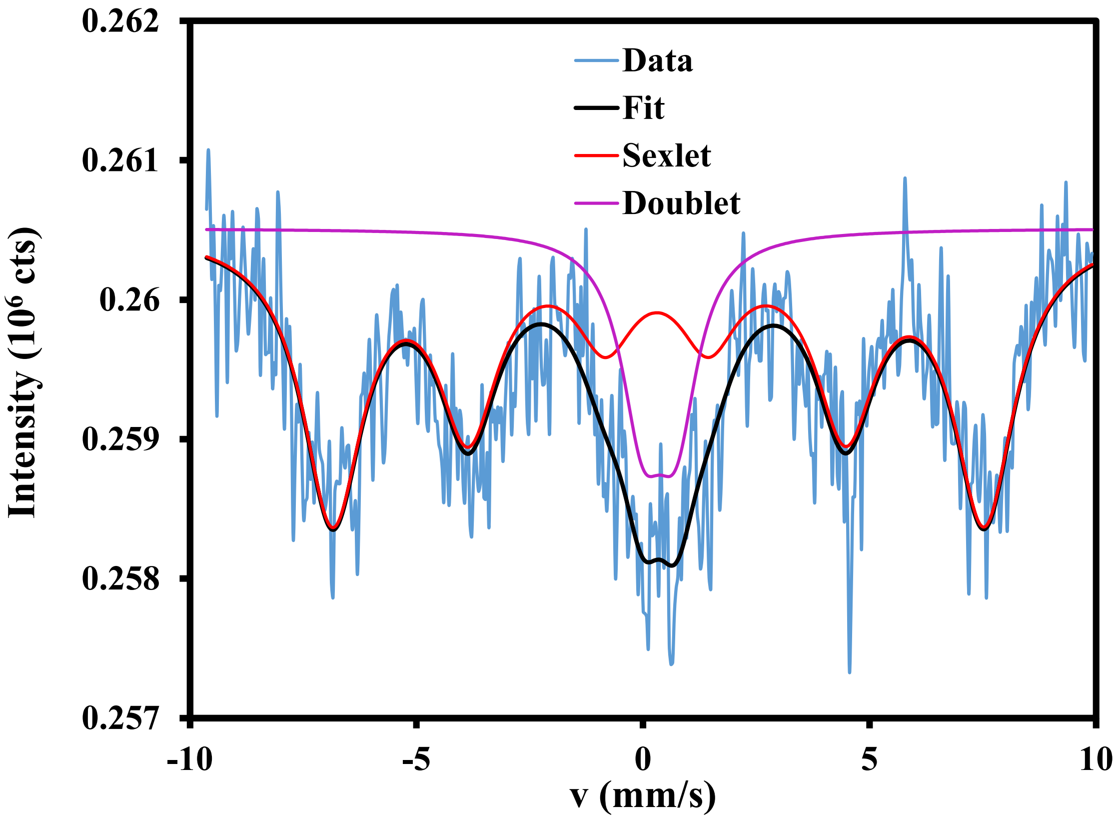

Figure S6. Mössbauer spectrum of the 160 cycles of iron oxide ALD coated $LiMn_{1.5}Ni_{0.5}O_4$ samples showing a sextet and a doublet site at the center.

SECTION

2. CONCLUSIONS AND FUTURE DIRECTIONS

2.1. CONCLUSIONS

A novel approach was developed to prepare porous titanium oxide films with subnanometer scale thickness controlled by MLD coating process followed by calcination. Ultra-thin titanicone films were deposited on sub-micron silica particles using MLD in a fluidized bed reactor at 100 °C. In order to remove the organic components of the MLD films and eventually creating porous films, the coated particles were then heated in air at 400 °C or exposed to water vapors for different time limits. The study was very helpful to understand the mechanism of controlling the porosity of the titania films.

Using the knowledge of creating the porous films after MLD process, a size-selective catalyst with an ultra-thin porous shell was prepared. The porous structure allows smaller reactants to access the encapsulated active sites, and inhibits or prevents the reactants with larger molecular size from accessing the metal catalytic sites. In this study, various thicknesses of porous alumina films were coated on Pt/SiO_2 particles. The thickness of the porous oxide films was well controlled at a nanometer scale by applying the MLD technique. Liquid-phase hydrogenation reaction of *n*-hexene versus *cis*-cyclooctene was carried out to test the size-selective effect of the prepared catalysts. This catalyst showed great selectivity in the hydrogenation of olefins. Importantly, the mass diffusion limitation was not significant due to the ultra-thin films. The success of making these materials by MLD opens up a new method for preparing size-selective catalysts.

ALD technique has been used for different types of nanostructures for LIBs application. The performance of electrode materials can be improved by depositing ultra-thin film coatings on the electrode powders. Although, ALD has been used previously by other groups for this purpose, their results showed either no significant improvement in capacity or the fabricated LIBs were not tested for enough charge-discharge cycles to verify the performance for long cycle life. There was a trade-off between the facile transport with a thin layer and long protection with a thick layer. In this study, the solution found was to coat ultra-thin conductive cerium oxide (CeO_2) coating with an optimum thickness on the cathode particle (LMO) surface, which provided a longer cycle life (~1,000 charge-discharge cycles) at a significantly improved capacity compared to the uncoated particles (96% and 95% capacity retention after 1,000 cycles with 1C rate at room temperature and 55 °C, respectively, and at least 24% improved initial capacity).

A study was conducted to understand the mechanism of performance enhancement of these CeO_2 coated cathode particles. It was understood from the previous study that the cerium oxide coated samples had much better conductivity than the uncoated sample. So, it became important to understand the ionic conductivity contributions for the CeO_2 coated cathode particles to explain the improved performance of the lithium-ion batteries. The experiments were conducted to measure the electronic and ionic conductivity of different thicknesses of CeO_2 coated LMO and LMNO particles by coating the two sides of the compressed pellets of the material with ion-blocking paste. Various thicknesses of Al_2O_3 and ZrO_2 coated LMO particles were also tested for comparison. The results showed that the ionic conductivity of the CeO_2-ALD film was at least two order of magnitudes higher than that of the uncoated substrates. The ionic conductivity of optimal thickness of CeO_2

coated sample was an order of magnitude higher than the insulating materials (Al_2O_3 and ZrO_2). This proved that the CeO_2-ALD film did in fact influence the Li-ion transport and thus perform much better than the uncoated material.

Another type of thin film coating materials was used to explore its electrochemical performance for the LIB application. Ultra-thin films of iron oxide-ALD were deposited on LMNO particles. A novel synergetic effect of Fe doping and ultra-thin iron oxide coating was found to be another key to address the trade-off between the long cycle life and the protection of the particles. XRD and XPS results of the iron oxide-ALD coated samples showed that the elemental Fe had penetrated the LMNO surface. Also, TEM showed that there was a conformal iron oxide coating on the particle surface after certain number of ALD coating cycles. The resultant nanostructure showed significant capacity improvement at 1C rate at room temperature and 55 °C, compared to the uncoated LMNO (UC). Notably, 30 cycles of FeO_x-ALD coated LMNO (30Fe) with an optimal film thickness of ~0.6 nm showed the best performance with 25% higher initial capacity than the UC, and 93% capacity retention even after 1,000 charge-discharge cycles at 1C rate at room temperature. At 55 °C, for the 30Fe sample the initial capacity was improved further by 26% than the UC, and the capacity retention even after 1,000 charge-discharge cycles at 1C rate was ~91%. This work reported the first time the synergic effect of doping and thin film coating on LMNO particles. ALD coating of iron oxide provided much better improvement in performance of LMNO than what could potentially be due to only doping effect. ALD has the potential to prepare these ultrathin electrochemically active films with an optimal thickness and synergetic effect of conductive coating and element doping, providing the industry to design novel electrodes that are durable as well as functional at high temperature and fast cycling rates.

2.2. FUTURE DIRECTIONS

For the size-selective catalysts, although, the supported Pt nanoparticles, encapsulated with a porous alumina shell, showed selectivity for catalytic hydrogenation of *n*-hexene versus *cis*-cyclooctene due to the size discrimination of the ultra-thin porous layer, the conversion was low. The decline was mainly caused by the loss of Pt metal surface. In order to improve the reactive Pt surface area, nanogaps could be introduced between the Pt nanoparticles and the porous shell, which provides the size-selective sieves and more active sites to achieve higher conversion. Porous titania films should also be explored due to its better stability in water, for the size-selective applications. In addition, ALD can "homogenize" supported heterogeneous catalysts by creating nanoparticles with extremely narrow distributions in size and composition, which is essential for understanding the fundamental nature of the catalytic active site. This type of control over the distribution of active sites is critical for elucidating reaction mechanisms that form the foundation for the rational design of improved catalysts.

For LIB cathode particles, a series of tests and characterizations should be conducted to investigate and establish the understanding for the working mechanism of the CeO_2 and iron oxide ALD coating on the performance of the cathode particles. These conductive coatings of CeO_2 should be applied to anodes, to test the effect of the coating. It is also important to understand the doping effect of iron during the iron oxide ALD process. The first step could be to investigate the doping amount with respect to the distance from surface to the center of the substrate. This could be carried out by a depth profile analysis using a secondary ion mass spectroscopy (SIMS) technique and Mossbauer spectroscopy. It is important to know the amount of Fe inside the structure of the substrate and depth of Fe doping and the point at which it starts forming the oxide film on the surface. Further in depth analysis of this unique phenomena could provide major breakthrough for not only to the field of energy storage but also to the ALD coating process.

APPENDIX

Rajankumar Patel's List of Publications during PhD Studies

I. First author papers:

1. Z. Shang[#], R.L. Patel[#], B.W. Evanko, and X. Liang*, Encapsulation of supported metal nanoparticles with an ultra-thin porous shell for size-selective reactions, ***Chemical Communications***, 49 (86), 10067-10069, 2013 ([#]Both authors contributed equally to this work; Featured as inside cover).
2. R.L. Patel, H. Xie, J. Park, H. Y. Asl, A. Choudhury, and X. Liang*, Significant capacity and cycle-life improvement of lithium-ion batteries through ultrathin conductive film stabilized cathode particles, ***Advanced Materials Interfaces***, 2 (8) 1500046, 2015 (Featured as inside cover)
3. R.L. Patel, Y.-B. Jiang, and X. Liang*, Highly porous titania films coated on sub-micron particles with tunable thickness by molecular layer deposition in a fluidized bed reactor, ***Ceramics International***, 41 (2), 2240-2246, 2014.
4. S.A. Palaparty[#], R.L. Patel[#], and X. Liang*, Enhanced cycle life and capacity retention of iron oxide ultrathin film coated SnO_2 nanoparticles at high current densities, ***RSC Advances***, 6, 24340-24348, 2016 ([#]Both authors contributed equally to this work).
5. R.L. Patel, Y.-B. Jiang, A. Choudhury, and X. Liang*, Employing synergetic effect of doping and thin film coating to boost the performance of lithium-ion battery cathode particles, revision *submitted to **Scientific Reports***.
6. R.L. Patel, H. Y. Asl, A. Choudhury, and X. Liang*, Ionic and electronic conductivities of thin atomic layer deposited film coated lithium ion battery cathode particles, *submitted to **RSC Advances***.
7. R.L. Patel, X. Liang*, Mitigating voltage fade in cathode materials by conductive thin film conformal coating, *manuscript in preparation*.

II. Co-author papers:

1. Y. Gong, R.L. Patel, X. Liang, D. Palacio, X. Song, J.B. Goodenough, and K. Huang*, Atomic layer deposition functionalized composite SOFC cathode $La_{0.6}Sr_{0.4}Fe_{0.8}Co_{0.2}O_{3-\delta}Gd_{0.2}Ce_{0.8}O_{1.9}$: Enhanced long-term stability, ***Chemistry of Materials***, 25 (21), 4224-4231, 2013.
2. Y. Gong, D. Palacio, X. Song*, R.L. Patel, X. Liang*, X. Zhao, J.B. Goodenough, and K. Huang*, Stabilizing nanostructured solid oxide fuel cell cathode with atomic layer deposition, ***Nano Letters***, 13 (9), 4340-4345, 2013.
3. X. Liang*, R.L. Patel, Porous titania microspheres with uniform wall thickness and high photoactivity, ***Ceramics International***, 40 (2), 3097-3103, 2014.
4. A. Pariyar, J. Stansbery, R.L. Patel, X. Liang, and A. Choudhury, The ubiquitous paddle-wheel building block in two-dimensional coordination polymer with square grid structure, ***Journal of Coordination Chemistry***, in press, 2016.

5. A. Pariyar, S. Gopalakrishnan, J. Stansbery, R.L. Patel, X. Liang, and A. Choudhury, 1-D Coordination Polymer Route to Catalytically Active Co@C Nanoparticles, ***RSC Advances***, in press, 2016.
6. X. Wang, A.R. Donovan, R.L. Patel, H. Shi, and X. Liang*, Nanoporous microparticles functionalized by atomic layer deposition for water treatment, *submitted to* ***Chemosphere***.

VITA

Mr. Rajankumar Patel was born in Gujarat, India. He earned a bachelor's degree in Chemical Engineering from Sardar Patel University, India in 2006. Before the graduation, he did internships at Amul Ltd. and Meghamani Organics Ltd., India. He worked as a Chemical Engineer at Gujarat Alkalies and Chemicals Ltd., India, during the first half of the year 2007. He came to USA and joined San Jose State University, California to get a master's degree in Chemical Engineering in 2007. After the graduation, he interned for a year as a MEMS Engineer at Silicon Microstructures, Inc., California. He then entered Missouri University of Science and Technology in January, 2012 and obtained his Doctor of Philosophy in Chemical Engineering from the Department of Chemical and Biochemical Engineering in May, 2016. During his Ph.D., he published a total of 13 research articles in peer-reviewed journals, and three conference papers. He won 2nd prize for his ALD-LIB work in Student Poster Session in Solid-state Science and Technology at the 227th ECS meeting, Chicago. He also won 1st prize in Graduate Research Showcase and a travel grant award from Council of Graduate Students at Missouri University of Science and Technology in 2015.